



On recovering distributed IP information from inductive source time domain electromagnetic data

Journal:	<i>Geophysical Journal International</i>
Manuscript ID	GJI-S-15-0747.R1
Manuscript Type:	Research Paper
Date Submitted by the Author:	17-Feb-2016
Complete List of Authors:	KANG, SEOGI; University of British Columbia, Earth, Ocean and Atmospheric Sceince Oldenburg, Doug; University of British Columbia, Earth, Ocean and Atmospheric Sceince
Keywords:	Electrical properties < GEOMAGNETISM and ELECTROMAGNETISM, Geomagnetic induction < GEOMAGNETISM and ELECTROMAGNETISM, Controlled source electromagnetics (CSEM) < GEOMAGNETISM and ELECTROMAGNETISM, Numerical approximations and analysis < GEOPHYSICAL METHODS, Inverse theory < GEOPHYSICAL METHODS

SCHOLARONE™
Manuscripts

1
2
3 submitted to *Geophys. J. Int.*
4
5
6
7
8

9 On recovering distributed IP information from inductive 10 11 source time domain electromagnetic data 12 13

14
15
16
17 Seogi Kang and Douglas W. Oldenburg
18
19

20 *Department of Earth, Ocean and Atmospheric Sciences, University of British Columbia, B.C. V6T 1Z4, Canada*
21
22
23
24
25

26 SUMMARY 27

28 We develop a procedure to invert time domain induced polarization (IP) data for inductive
29 sources. Our approach is based upon the inversion methodology in conventional electrical
30 IP (EIP), which uses a sensitivity function that is independent of time. However, signif-
31 icant modifications are required for inductive source IP (ISIP) because electric fields in
32 the ground do not achieve a steady state. The time-history for these fields needs to be
33 evaluated and then used to define approximate IP currents. The resultant data, either a
34 magnetic field or its derivative, are evaluated through the Biot-Savart law. This forms the
35 desired linear relationship between data and pseudo-chargeability. Our inversion pro-
36 cedure has three steps: 1) Invert TEM data and recover a 3D distribution of conductivity.
37 2) Decouple IP responses embedded in the observations by forward modelling the TEM
38 data due to a background conductivity and subtracting these from the observations. 3)
39 Use the linearized sensitivity function to invert data at each time channel and recover
40 pseudo-chargeability. Post-interpretation of the recovered pseudo-chargeabilities at mul-
41 tiple times allows recovery of intrinsic Cole-Cole parameters such as time constant and
42 chargeability. The procedure is applicable to all inductive source survey geometries but
43 we focus upon airborne time domain EM (ATEM) data with a coincident-loop configura-
44 tion because of the distinctive negative IP signal that is observed over a chargeable body.
45 Several assumptions are adopted to generate our linearized modelling but we systemati-
46
47
48
49
50
51
52
53
54
55
56
57
58
59
60

1
2 2 *Seogi Kang and Douglas W. Oldenburg*
3
4
5
6
7
8
9
10
11
12
13
14
15
16
17
18
19
20
21
22
23
24
25
26
27
28
29
30
31
32
33
34
35
36
37
38
39
40
41
42
43
44
45
46
47
48
49
50
51
52
53
54
55
56
57
58
59
60

 cally test the capability and accuracy of the linearization for ISIP responses arising from different conductivity structures. On test examples we show: (a) our decoupling procedure enhances the ability to extract information about existence and location of chargeable targets directly from the data maps; (b) the horizontal location of a target body can be well recovered through inversion; (c) the overall geometry of a target body might be recovered but for ATEM data a depth weighting is required in the inversion; (d) we can recover estimates of intrinsic τ and η that may be useful for distinguishing between two chargeable targets.

1 1 INTRODUCTION

2 The electrical conductivity of earth materials can be frequency dependent with the effective conductivity decreasing with decreasing frequency due to the buildup of electric charges that occur under the application of an electric field. Effectively, the rock is electrically polarized. Applications of induced polarization (IP) surveys to find chargeable material have been particularly successful in mineral exploration for disseminated sulphide or porphyry deposits (Pelton et al. 1978; Fink et al. 1990) and also in geotechnical and environmental problems (Li & Oldenburg 2000; Kemna et al. 2012).

3 Polarization charges can accumulate whenever there is an electric field in a medium. In controlled source surveys, the transmitter can be a galvanic source (a generator attached to two grounded electrodes), or an inductive source (arising from currents flowing in a wire loop). Most research and application has focused upon using grounded electrodes and measuring electric fields; this is called an EIP survey (Seigel 1959). Magnetic fields arising from polarization currents using grounded electrodes as the transmitter (MIP survey) have also been successfully used, particularly in mineral exploration when there is a conductive overburden (Seigel 1974). In recent years attention has also turned towards the use of inductive sources. Inductive source IP (ISIP), can have transmitters in the air or on the ground and the waveforms can be in the frequency or time domain. Recently (Marchant et al. 2012) showed how, by collecting data at two frequencies, it was possible to measure data that depended purely on IP signals and that these data can be inverted to recover a 3D distribution of chargeability. For time domain systems the observations of negative transients in coincident-loop systems provide an distinctive verification of the existence of chargeable material (Weidelt 1982). These negative transients have been frequently observed (Smith & Klein 1996; Kang & Oldenburg 2015). The effects of chargeable objects using time domain systems with inductive sources have been investigated (Smith et al. 1988; Flis et al. 1989; ElKaliouby & Eldiwany 2004; Marchant et al. 2014) and approximate

1
2
3 *On recovering distributed IP information from inductive source time domain electromagnetic data* 3
45 1 interpretation tools (Kratzer & Macnae 2012; Hodges & Chen 2014) are being developed. The ability
6 2 to fully invert these data in 3D is still lacking.
78 3 Extracting information about the complex conductivity from observed data can be done in a variety
9 4 of ways. An inverse problem can be set up to find a function $\sigma(x, y, z, \omega)$ or a parameterization of the
10 5 complex conductivity, usually with a Cole-Cole type model, (Fiandaca et al. 2012; Marchant et al.
11 6 2013; Xu & Zhdanov 2015). Traditionally, however, with EIP and time domain waveforms, one first
12 7 estimates the background conductivity from the asymptotic on-time data and then inverts off-time data
13 8 to recover information about “chargeability” (Oldenburg & Li 1994). This is carried out by solving an
14 9 inverse problem using a linear function where the sensitivities depend upon geometry of the survey
15 10 and the background conductivity. The recovered values are really pseudo-chargeability, and they have
16 11 the same units as the data (eg. msec, mV/V). The same procedure can be used in the frequency domain
17 12 experiments but the data might have units of mrad and pfe (percent frequency effect). Inversions of IP
18 13 data to recover 2D or 3D distributions of pseudo-chargeability are now commonly carried out (Kemna
19 14 et al. 2012). These inversions delineate locations of high pseudo-chargeability and the geometry of the
20 15 bodies. MIP data can be inverted with the same methodology (Chen & Oldenburg 2003). We note that
21 16 pseudo-chargeability is different from intrinsic chargeability, η , where $\eta = \frac{\sigma_\infty - \sigma_0}{\sigma_\infty}$ and σ_∞ and σ_0 are
22 17 respectively the conductivity at the infinite frequency and the zero frequency.
3334 18 The physical mechanisms by which polarization charges and currents are established in the ground
35 19 are independent of the type of transmitter and waveform; the important quantity is the time history of
36 20 the electric field within the earth. The challenge posed by the use of inductive sources is that steady
37 21 state electric fields are not established inside the earth as they are for EIP or MIP surveys. At any
38 22 location in the earth the electric field will increase to a maximum value and then decrease as the
39 23 electromagnetic (EM) wave diffuses through. The EM fields at any position and time depend upon the
40 24 convolution of the electric field with the time-dependent conductivity of the rock. Unravelling these
41 25 complexities, and providing a framework for extracting information about IP characteristics of rocks,
42 26 are issues we address in our paper.
4849 27 Our procedure involves three principal steps: 1) estimating the 3D background conductivity and
50 28 carrying out an EM-decoupling to produce IP data (d^{IP}), and 2) developing a linearized formulation
51 29 using the Biot-Savart law and an effective pseudo-chargeability that encapsulates time dependencies
52 30 of the EM fields at any location in the earth, 3) inverting d^{IP} using the linear functional to recover
53 31 pseudo-chargeability at each time channel, and subsequently processing these multi-channel data to
54 32 obtain information about Cole-Cole parameters for each point in the subsurface. Each of these steps
55 33 requires special attention for inductive source data and approximations are required. Our paper pro-
56 34 ceeds as follows. We first outline our decomposition process for obtaining d^{IP} data, define a pseudo-

1
2
3 4 *Seogi Kang and Douglas W. Oldenburg*
5

6 chargeability, and show how our problem can be linearized. The data and pseudo-chargeability are
7 linearly related through the Biot-Savart law and hence a depth weighting, required for other potential
8 field inversions, is necessary to obtain geologically meaningful solutions. The inversion can be carried
9 out at multiple times and a pseudo-chargeability as a function of time can be generated. These results
10 can be used to recover intrinsic decays of the chargeable rock units and thus potentially differentiate
11 between rock types in the same manner as carried out by Yuval & Oldenburg (1997) using EIP data. In
12 our numerical experiments, we investigate the above steps and procedures, test our assumptions, and
13 evaluate the circumstances under which our technique might provide meaningful results. Although we
14 focus upon airborne TEM data, the analysis we present here is valid for surveys on the earth's surface
15 using inductive sources and also for grounded sources although many of the complications we deal
16 with are not relevant.
17
18
19
20
21
22
23
24
25
26
27
28

12 2 COMPLEX CONDUCTIVITY

29
30 A complex conductivity model presents a mathematical form of the IP phenomenon, and there are a
31 number of models used in the literature (Dias 2000; Tarasov & Titov 2013). Each model has some
32 reflection of an IP phenomenon, and each of these models is an attempt to capture the complicated
33 nature of complex conductivity with a few parameters that may, or may not, have a physical meaning.
34 For our research we needed to choose one. We follow Smith et al. (1988) and Marchant et al. (2014)
35 who used a Cole-Cole model (Cole & Cole 1941) modified by Pelton et al. (1978):
36
37

$$40 \quad 41 \quad \sigma(s) = \sigma_\infty - \sigma_\infty \left(\frac{\eta}{1 + (1 - \eta)(s\tau)^c} \right) = \sigma_\infty + \Delta\sigma(s), \quad (1)$$

42
43 where s is the Laplace transform variable, σ_∞ is the conductivity at infinite frequency, η is the intrinsic
44 chargeability, τ is the time constant and c is the frequency dependency.
45

46
47 Real and imaginary parts of complex conductivity in the frequency domain are shown in Fig. 1(a)
48 for Cole-Cole parameters: $\sigma_\infty = 10^{-2}$ S/m, $\eta = 0.5$, $\tau = 0.01$ s, and $c=1$. By applying the inverse
49 Laplace transform, we have
50

$$52 \quad 53 \quad \sigma(t) = \mathcal{L}^{-1}[\sigma(s)] = \sigma_\infty \delta(t) + \Delta\sigma(t), \quad (2)$$

54
55 where $\delta(t)$ is Dirac delta function, and $\mathcal{L}^{-1}[\cdot]$ is inverse Laplace transform operator. Note that we
56 only deal with a causal function, which is defined when $t \geq 0$.
57

58 The intrinsic chargeability η is
59

$$60 \quad \eta = -\frac{1}{\sigma_\infty} \lim_{t \rightarrow \infty} \mathcal{L}^{-1}\left[\frac{\Delta\sigma(s)}{s}\right] \quad (3)$$

On recovering distributed IP information from inductive source time domain electromagnetic data 5

Accordingly, it is convenient to define an impulse pseudo-chargeability, $\tilde{\eta}^I(t)$ as

$$\tilde{\eta}^I(t) = -\frac{\Delta\sigma(t)}{\sigma_\infty}. \quad (4)$$

Effectively this writes $\Delta\sigma(t)$ as

$$\Delta\sigma(t) = -\sigma_\infty\tilde{\eta}^I(t), \quad (5)$$

Note that the intrinsic chargeability, η , is not time-dependent but the impulse pseudo-chargeability, $\tilde{\eta}^I(t)$, which is related to IP parameters: η , τ , and c , is time-dependent. The Cole-Cole response in time domain is shown in Fig. 1(b). The arrow at $t=0$ s indicates $\sigma_\infty\delta(t)$, which is a delta function, and after $t=0$ s, $\sigma(t) = \Delta\sigma(t)$. Since Ohm's law in time states that $\vec{j} = \sigma \otimes \vec{e}$ where \otimes indicates convolution, the negative sign of $\Delta\sigma(t)$ shows that the polarization current in the chargeable body will have a reversed direction compared to the primary current when an electric field is applied. We will revisit this later in Section 4.

3 DECOMPOSITION OF OBSERVED RESPONSES

IP effects in the observed data are coupled with EM effects. We need to decompose the observations to isolate data associated only with the IP phenomena. Maxwell's equations in the time domain, with a quasi-static approximation, are written as:

$$\vec{\nabla} \times \vec{e} = -\frac{\partial \vec{b}}{\partial t}, \quad (6)$$

$$\vec{\nabla} \times \frac{1}{\mu} \vec{b} - \vec{j} = \vec{j}_s, \quad (7)$$

where \vec{e} is the electric field (V/m), \vec{b} is the magnetic flux density (Wb/m^2), \vec{j}_s is the current source (A/m^2) and μ is the magnetic permeability (H/m). Here \vec{j} is the conduction current (A/m^2). In the frequency domain, this conduction current, \vec{J} , is related to conductivity via Ohms law: $\vec{J}(s) = \sigma(s)\vec{E}(s)$ where \vec{E} is the electric field. Converting this relationship to time domain using the inverse Laplace transform yields:

$$\vec{j}(t) = \sigma \otimes \vec{e} = \int_0^t \sigma(u) \vec{e}(t-u) du. \quad (8)$$

Thus the current density depends upon the previous history of the electric field. As in Smith et al. (1988), we represent total fields as $\vec{e} = \vec{e}^F + \vec{e}^{IP}$, $\vec{b} = \vec{b}^F + \vec{b}^{IP}$ and $\vec{j} = \vec{j}^F + \vec{j}^{IP}$, where superscript F indicates fundamental and IP is induced polarization. Here fundamental fields indicate EM fields when the chargeability is zero. Thus $\sigma(s) = \sigma_\infty$ (eq. 1) and there are no IP effects.

Equations (6) and (7) are written as

$$\vec{\nabla} \times (\vec{e}^F + \vec{e}^{IP}) = -\frac{\partial}{\partial t}(\vec{b}^F + \vec{b}^{IP}), \quad (9)$$

1
2
3 6 Seogi Kang and Douglas W. Oldenburg
4
5

6
$$\vec{\nabla} \times \frac{1}{\mu}(\vec{b}^F + \vec{b}^{IP}) - (\vec{j}^F + \vec{j}^{IP}) = \vec{j}_s. \quad (10)$$

7
8

1 The fundamental equations can be written as
2
3

4
$$\vec{\nabla} \times \vec{e}^F = -\frac{\partial \vec{b}^F}{\partial t}, \quad (11)$$

5
6

7
$$\vec{\nabla} \times \frac{1}{\mu} \vec{b}^F - \vec{j}^F = \vec{j}_s. \quad (12)$$

8
9

10 where
11
12

13
$$\vec{j}^F = \sigma_\infty \vec{e}^F. \quad (13)$$

14
15

16 Subtraction of the fundamental fields yields the expressions for the IP fields
17
18

19
$$\vec{\nabla} \times \vec{e}^{IP} = -\frac{\partial \vec{b}^{IP}}{\partial t}, \quad (14)$$

20
21

22
$$\vec{\nabla} \times \frac{1}{\mu} \vec{b}^{IP} = \vec{j}^{IP}. \quad (15)$$

23
24

25 Let $F[\cdot]$ denote the operator associated with Maxwells equations, and let d denote the observations
26 that include both EM and IP effects. Keeping the same notation, we obtain $d = d^F + d^{IP}$, where d^F
27 and d^{IP} are fundamental and IP responses, respectively. Based on this, we define the IP datum as
28
29
30
31

32
$$d^{IP} = d - d^F = F[\sigma(t)] - F[\sigma_\infty]. \quad (16)$$

33
34

35 Here $F[\sigma_\infty]$ corresponds to the fundamental response (d^F). This subtraction acts as an EM-decoupling
36 process which removes the EM effects from the measured responses. This is the same procedure that
37 formed the basis of work by Routh & Oldenburg (2001).
38
39

40
41 **4 PSEUDO-CHARGEABILITY**
42
43

44 Writing
45

46
$$\vec{j}^{IP} = \vec{j}(t) - \vec{j}^F \quad (17)$$

47
48

49 and using eqs (2) and (8) we obtain
50
51

52
$$\vec{j}^{IP} = \sigma_\infty \vec{e}^{IP} + \vec{j}^{pol}, \quad (18)$$

53
54

55 where the polarization current (\vec{j}^{pol}) is
56
57

58
$$\vec{j}^{pol}(t) = \Delta\sigma(t) \otimes \vec{e}(t). \quad (19)$$

59
60

61 If the electric field has different characteristics for the inductive and galvanic sources this will
62 generate different features in the polarization current. We consider two cases: a) a galvanic source
63 without EM induction and b) an inductive source with EM induction. The first case corresponds to EIP
64
65
66
67
68
69
70
71
72
73
74
75
76
77
78
79
80
81
82
83
84
85
86
87
88
89
90
91
92
93
94
95
96
97
98
99
100
101
102

On recovering distributed IP information from inductive source time domain electromagnetic data 7

(Seigel 1959), and the second is associated with ISIP. Fig. 2 shows the amplitude of the fundamental electric field, \vec{e}^F , in the earth for those two cases. For the galvanic source without EM induction effects ($\frac{\partial \vec{b}}{\partial t} = 0$), the electric field is instantaneously on or off in response to the transmitter. (Fig. 2 a). However, for the inductive source, the electric field in the off-time is not zero, but increases to a peak and then decays as shown in Fig. 2 (b). The polarization current for the two sources will be significantly affected by these different electric fields. To capture this difference in a linearized kernel for the IP response, we define pseudo-chargeability ($\tilde{\eta}(t)$) as

$$\tilde{\eta}(t) = -\frac{\vec{j}^{pol}(t)}{\vec{j}^{ref}}, \quad (20)$$

where the reference current (\vec{j}^{ref}) is defined as

$$\vec{j}^{ref} = \sigma_\infty \vec{e}^{ref}. \quad (21)$$

Here \vec{e}^{ref} is the reference electric field, and we will explain our choice of \vec{e}^{ref} below. The pseudo-chargeability defined in eq. (20) is the ratio of the polarization current to the reference current. This is a small quantity and it plays an essential role in our linearization. To evaluate the pseudo-chargeability, we need to identify a reference current or reference electric field, \vec{e}^{ref} , which is independent of time. For EIP, we choose the value of the electric field achieved when there is no IP present, that is the value shown in Fig. 2(a). For the inductive source we choose the peak electric field as shown in Fig. 2(b)

Each pixel in the earth has its own reference electric field and time thus both \vec{e}^{ref} and t^{ref} have a 3D distribution. For both EIP and ISIP cases, we mathematically present our choice of the reference electric field as

$$\vec{e}^{ref} = \vec{e}^F(t) \otimes \delta(t - t^{ref}). \quad (22)$$

The reference time for the EIP case can be any time in the on-time.

By rearranging eq. (20), we obtain

$$\vec{j}^{pol} = -\vec{j}^{ref} \tilde{\eta}(t). \quad (23)$$

This states that the polarization current has an opposite direction to the reference current, and is proportional to the pseudo-chargeability, $\tilde{\eta}(t)$. This reversed direction of the current in a chargeable medium results from the negative values of the time-dependent conductivity when $t > 0$ sec as shown in Fig. 1(b). This conceptual model about the polarization current shown in eq. (23) is consistent with Seigel (1959)'s result. We note, that for any pixel, even if \vec{e}^{ref} attains the same value for an ISIP survey as for an EIP survey, the pseudo-chargeability resulting from an ISIP survey will be less than that from an EIP survey. We can infer from this that linearization techniques, which have worked so well in EIP problems, should be successful in ISIP problems.

1
2
3 8 Seogi Kang and Douglas W. Oldenburg
4
5

6 **5 LINEARIZATION**
7

8 Following from the methodologies in EIP, our goal is to express the IP response, d^{IP} , as a linear
9 function of the pseudo-chargeability, $\tilde{\eta}(t)$. That is we wish to write $d^{IP}(t) = J\tilde{\eta}(t)$, where J is a
10 linear operator which is independent of time. In doing this we first consider a general EM system
11 which is applicable to galvanic or inductive sources. For any volume pixel in the earth the amplitude
12 and direction of the electric field can vary dramatically in time and thus the IP charging process can
13 be complicated. However, if substantial polarization currents are developed we assume there was a
14 sufficiently large electric field in a predominant direction to generate them. Although the direction of
15 the electric field is constant the amplitude varies with time.
16
17

18 Let $\vec{e}(t)$ be approximated as
19
20

$$\vec{e}(t) \approx \vec{e}^{ref} \hat{w}(t), \quad (24)$$

21 where $\hat{w}(t)$ is defined as:
22
23

$$\hat{w}(t) = P_0[w^{ref}(t)]. \quad (25)$$

24 Here a projection $P_0[\cdot]$ of an arbitrary function, $f(t)$, is
25
26

$$P_0[f(t)] = \begin{cases} f(t) & f(t) \geq 0 \\ 0 & \text{if } f(t) < 0, \end{cases} \quad (26)$$

27 and
28

$$w^{ref}(t) = \frac{\vec{e}^F(t) \cdot \vec{e}^{ref}}{\vec{e}^{ref} \cdot \vec{e}^{ref}}. \quad (27)$$

29 $w^{ref}(t)$ is a dimensionless function that prescribes the time history of the electric field at each location
30 along the direction of the chosen reference electric field, \vec{e}^{ref} . Negative values of $w^{ref}(t)$ are set to
31 zero in accordance with our conceptual model that polarization currents have an opposite direction to
32 the reference current (eq. 23). We redefine the pseudo-chargeability as
33
34

$$\tilde{\eta}(t) = \tilde{\eta}^I(t) \otimes \hat{w}(t). \quad (28)$$

35
36 49 The polarization current, \vec{j}^{pol} can be approximated with eq. (4) as
50
51

$$\vec{j}^{pol}(t) \approx -\tilde{\eta}^I(t) \otimes \hat{w}(t) \vec{j}^{ref}. \quad (29)$$

52
53 54 Substituting into eq. (18) yields
55
56

$$\vec{j}^{IP}(t) \approx \sigma_\infty \vec{e}^{IP}(t) - \tilde{\eta}^I(t) \otimes \hat{w}(t) \vec{j}^{ref} \quad (30)$$

57
58 60 and this yields
59
60

$$\vec{j}^{IP}(t) \approx \sigma_\infty \vec{e}^{IP}(t) - \vec{j}^{ref} \tilde{\eta}(t). \quad (31)$$

On recovering distributed IP information from inductive source time domain electromagnetic data 9

The second term, $-\vec{j}^{ref}\tilde{\eta}(t)$, corresponds to polarization currents. The first term, $\sigma_\infty\vec{e}^{IP}(t)$, is usually omitted (Smith et al. 1988). This was because Smith et al. (1988) were mostly interested in chargeable targets that were significantly conductive compared to the background. However, if the conductivity of the chargeable target is similar to that of the background the first term could be important.

We include it here and will explore the conditions in which it is important. Because the reference current is static, any time-dependence in the polarization currents is encapsulated in the pseudo-chargeability. The buildup and decrease of polarization currents is a slow process and we assume therefore that this process does not produce induction effects ($\frac{\partial\vec{b}^{IP}}{\partial t} \approx 0$) and hence we can write

$$\vec{e}^{IP} \approx \vec{e}_{approx}^{IP} = -\vec{\nabla}\phi^{IP}, \quad (32)$$

where ϕ^{IP} is the electrical potential for IP. By taking the divergence of eq. (31), substituting \vec{e}^{IP} with eq. (32), and carrying out some linear algebra, we obtain

$$\phi^{IP}(t) \approx -[\nabla \cdot \sigma_\infty \vec{\nabla}]^{-1} \nabla \cdot \vec{j}^{ref}\tilde{\eta}(t). \quad (33)$$

By applying the gradient we obtain

$$\vec{e}_{approx}^{IP} = \vec{\nabla}[\nabla \cdot \sigma_\infty \vec{\nabla}]^{-1} \nabla \cdot \vec{j}^{ref}\tilde{\eta}(t). \quad (34)$$

Thus, the electric field due to the IP effect can be expressed as a function of $\tilde{\eta}(t)$ in time. This form is also applicable to the EIP case.

For an inductive source, the data are either \vec{b} or its time derivative and hence we also need to compute \vec{b}^{IP} or its time derivative. For this, we first compute \vec{j}^{IP} then use the Biot-Savart law. By substituting eq. (34) into eq. (31), the approximated IP current density, \vec{j}_{approx}^{IP} can be expressed as

$$\vec{j}^{IP}(t) \approx \vec{j}_{approx}^{IP} = \bar{S}\vec{j}^{ref}\tilde{\eta}(t), \quad (35)$$

where

$$\bar{S} = \sigma_\infty \vec{\nabla}[\nabla \cdot \sigma_\infty \vec{\nabla}]^{-1} \nabla \cdot -\bar{I} \quad (36)$$

and \bar{I} is an identity tensor. Applying the Biot-Savart law we have:

$$\vec{b}_{approx}^{IP}(\vec{r}; t) = \frac{\mu_0}{4\pi} \int_{\Omega} \frac{\bar{S}\vec{j}^{ref}(\vec{r}_s) \times \hat{r}}{|\vec{r} - \vec{r}_s|^2} \tilde{\eta}(t) d\vec{r}_s, \quad (37)$$

where \vec{r}_s indicates a vector for a source location, and $\hat{r} = \frac{\vec{r} - \vec{r}_s}{|\vec{r} - \vec{r}_s|}$. If $\sigma_\infty\vec{e}^{IP}$ is omitted in \vec{j}^{IP} then the tensor, \bar{S} becomes $-\bar{I}$. In this situation, the IP current is same as the polarization current, and it always has an opposite direction to the reference current. This reversed current, along with Biot-Savart law, provides a physical understanding about the negative transients in ATEM data when the earth is chargeable.

1
2
3 10 Seogi Kang and Douglas W. Oldenburg
4
5

6 Observed data are often the time derivative of \vec{b} , hence by taking time derivative to the eq. (37),
7 we obtain
8

9
$$-\frac{\partial \vec{b}_{approx}^{IP}}{\partial t}(\vec{r}; t) = \frac{\mu_0}{4\pi} \int_{\Omega} \frac{\vec{S} \vec{j}^{ref}(\vec{r}_s) \times \hat{r}}{|\vec{r} - \vec{r}_s|^2} \left(-\frac{\partial \tilde{\eta}(t)}{\partial t} \right) d\vec{r}_s. \quad (38)$$

10
11

12 Here we have chosen to keep the minus signs in eq. (38) so that $-\frac{\partial \tilde{\eta}(t)}{\partial t}$ is positive when $\tilde{\eta}(t)$ is
13 decaying in time. Accordingly, the IP datum is given by $-\frac{\partial \vec{b}^{IP}}{\partial t}$.
14

15 The IP fields shown in eqs (34), (37) and (38) are linear functionals of $\tilde{\eta}$ and the equations for a
16 single time channel can be discretized in space as
17

18
$$\mathbf{d}^{IP} = \mathbf{J} \tilde{\eta}, \quad (39)$$

19
20

21 where \mathbf{J} is the corresponding sensitivity matrix. In particular when the observed datum is the time
22 derivative of \vec{b} , the linear relationship can be written as
23

24
$$\mathbf{d}^{IP} = \mathbf{J} \left(-\frac{\partial \tilde{\eta}}{\partial t} \right). \quad (40)$$

25
26

27 A detailed description for the discretization of the linearized kernel is shown in Appendices C1 and
28 C2. The representation in eq. (39) is valid for galvanic and inductive sources but the two assumptions:
29
30 a) $\vec{e} \approx \vec{e}^{ref} \hat{w}(t)$ and b) $\vec{e}^{IP} \approx -\vec{\nabla} \phi^{IP}$ need to be tested numerically for the case of inductive sources.
31
32

33
34
35 12 **6 IP INVERSION METHODOLOGY**
36

37 For the inversion of ISIP data, we focus on an ATEM survey with a coincident-loop geometry. From
38 the previous section, we first defined the IP datum (eq. 16) then linearized it as a function of the
39 pseudo-chargeability (eq. 39). The linearization was developed for a single transmitter. An ATEM
40 survey however includes many transmitters and each will excite a volumetric pixel differently. We
41 address this important issue in Appendix A1. It requires combining the pseudo-chargeabilities that
42 arise from individual transmitters into a transmitter-independent effective pseudo-chargeability. This
43 requires computing, and combining, the individual time histories of the electric fields due to each
44 transmitter into an effective time history. The result is that a d^{IP} datum for any transmitter takes the
45 form:
46

47
$$\begin{bmatrix} \mathbf{d}_1^{IP}(t) \\ \mathbf{d}_2^{IP}(t) \\ \vdots \\ \mathbf{d}_{nTx}^{IP}(t) \end{bmatrix} = \begin{bmatrix} \mathbf{J}_1 \\ \mathbf{J}_2 \\ \vdots \\ \mathbf{J}_{nTx} \end{bmatrix} \begin{bmatrix} \tilde{\eta}(t) \end{bmatrix}, \quad (41)$$

48
49
50
51
52
53
54
55
56
57
58

59 where $\mathbf{d}_k^{IP}(t)$ and \mathbf{J}_k indicates the IP datum and sensitivity matrix at k -th transmitter. Here $\tilde{\eta}(t)$
60 stands for an effective pseudo-chargeability, which represents pseudo-chargeability from all transmit-

On recovering distributed IP information from inductive source time domain electromagnetic data 11

ters. Hence, for a given effective pseudo-chargeability we can compute IP responses at all transmitters. Eq. 41 shows that IP data for an ATEM survey are linearly related to effective pseudo-chargeability. Information about chargeability can be obtained by solving a linear inverse problem. This is a common problem in applied geophysics so we provide only an essential summary.

6.1 3D IP inversion with a linearized kernel

The linear inverse problem to recover chargeability is straightforward and is described in Oldenburg & Li (1994). We rewrite eq. (39) as

$$\mathbf{d}^{pred} = \mathbf{J}\mathbf{m}, \quad (42)$$

where \mathbf{J} is the sensitivity matrix of linear problem, which corresponds to \mathbf{J} shown in eq. (39). Here, \mathbf{d}^{pred} represents IP responses at a single time channel, \mathbf{m} denotes model parameters, which can be either $\tilde{\eta}$ or $-\frac{\partial \tilde{\eta}}{\partial t}$. The important positivity constraint results because the intrinsic chargeability η is restricted to the range [0,1].

The solution to the inverse problem is the model \mathbf{m} that solves the optimization problem

$$\text{minimize } \phi = \phi_d(\mathbf{m}) + \beta\phi_m(\mathbf{m}) \quad (43)$$

$$\text{s.t. } 0 \leq \mathbf{m},$$

where ϕ_d is a measure of data misfit, ϕ_m is a user-defined model objective function and β is regularization or trade-off parameter.

We use the sum of the squares to measure data misfit

$$\phi_d = \|\mathbf{W}_d(\mathbf{A}\mathbf{m} - \mathbf{d}^{obs})\|_2^2 = \sum_{j=1}^N \left(\frac{d_j^{pred} - d_j^{obs}}{\epsilon_j} \right)^2, \quad (44)$$

where N is the number of the observed data and \mathbf{W}_d is a diagonal data weighting matrix which contains the reciprocal of the estimated uncertainty of each datum (ϵ_j) on the main diagonal, \mathbf{d}^{obs} is a vector containing the observed data, \mathbf{d}^{pred} is a vector containing calculated data from a linear eq. given in eq. (42). The model objective function, ϕ_m , is a measure of the amount structure in the model and upon minimization this will generate a smooth model which is close to a reference model, \mathbf{m}_{ref} .

We define ϕ_m as

$$\phi_m = \sum_{i=s,x,y,z} \alpha_i \|\mathbf{W}_i \mathbf{W}(\mathbf{m} - \mathbf{m}_{ref})\|_2^2, \quad (45)$$

where \mathbf{W} is a model weighting matrix, which will be defined below, \mathbf{W}_s is a diagonal matrix containing volumetric information of prisms, and \mathbf{W}_x , \mathbf{W}_y and \mathbf{W}_z are discrete approximations of the

1
2
3 12 *Seogi Kang and Douglas W. Oldenburg*
4
5

6 first derivative operator in x , y and z directions, respectively. The α 's are weighting parameters that
7 balance the relative importance of producing small or smooth models (Tikhonov & Arsenin 1977).
8
9

10 Because in our ATEM data we have only a single datum for each transmitter, we do not have
11 intrinsic depth resolution. This is the same circumstance encountered when inverting magnetic data.
12 (Li & Oldenburg 1996). Correspondingly we apply a depth weighting through the model weighting
13 matrix (\mathbf{W}):
14
15

$$\mathbf{W} = \text{diag}(\mathbf{z} - \mathbf{z}_0)^{1.5}, \quad (46)$$

16 where \mathbf{z} and \mathbf{z}_0 are discretized depth locations and reference depth in the 3D domain.
17
18

19 Although we use the linear form of d^{IP} data (eq. 39), the inverse problem is nonlinear because
20 of imposed positivity on \mathbf{m} . We solve this constrained optimization problem using a projected Gauss-
21 Newton (GN) method (Kelley 1999). For further details of implementing this constrained optimization
22 see Marchant et al. (2012). The trade-off parameter, β , is determined using a cooling technique where
23 β is progressively reduced from some high value. The inversion is stopped when the tolerance is
24 reached (cf. Nocedal & Wright (1999); Oldenburg & Li (2005); Kang & Oldenburg (2015)).
25
26

27 For the implementation of our IP inversion algorithm, we use an open source python package
28 for simulation and gradient-based parameter estimation in geophysics called SIMPEG (Cockett et al.
29 2015).
30
31
32
33
34

40 41 42 43 44 45 46 47 48 49 50 51 52 53 54 55 56 57 58 59 60 6.2 IP inversion workflow

61 The 3D IP inversion methodology provides us with a capability to invert IP data at each time channel.
62 However, before we invert those IP data, we need to compute an estimate of σ_∞ which is needed for
63 EM-decoupling as well as generating the sensitivity matrix.
64
65

66 Considering the multiple tasks required to restore IP information from TEM data we use the
67 following workflow: (1) invert early-time TEM data that appear not to be contaminated with IP effects.
68 This yields a 3D conductivity model, σ_{est} which should be reasonably close to σ_∞ . (2) Forward model
69 σ_{est} to obtain the fundamental response d^F and subtract it from the observations to obtain d^{IP} data.
70 (3) Invert d^{IP} data to recover a pseudo-chargeability model at individual time channels using the
71 relationship in eq. (39). (4) Further, process the inversion outputs at multiple time-channels to estimate
72 the Cole-Cole, or equivalent IP parameters. For detailed descriptions of this step see Appendix B.
73
74

75 In the following we investigate each of the above steps via numerical simulations and test the
76 validity of our assumptions.
77
78

1
2
3 *On recovering distributed IP information from inductive source time domain electromagnetic data* 13
4
5

6 **7 NUMERICAL EXPERIMENTS**

7 For our numerical experiments we concentrate upon coincident-loop ATEM surveys. This choice is
8 made because of the observed negative transients that are direct indicators of IP phenomena (Smith &
9 Klein 1996; Kratzer & Macnae 2012; Kang & Oldenburg 2015), and the extensive use of this survey
10 by industry.

11 We begin with a simple IP model composed of a chargeable block in a halfspace as shown in
12 Figure 3. Cole-Cole parameters of the block are $\eta = 0.2$, $\tau = 0.005$ and $c = 1$. The conductivity of the
13 halfspace, (σ_1) is 10^{-3} S/m, whereas σ_2 , the conductivity at infinite frequency for the chargeable body,
14 is variable. We consider three cases: a) canonical ($\sigma_2 = \sigma_1$), b) conductive ($\sigma_2 = 10^2 \times \sigma_1$) and c)
15 resistive models ($\sigma_2 = 10^{-2} \times \sigma_1$). The 3D earth is discretized with $50 \times 50 \times 50$ m core cells and the
16 number of cells in the domain is $41 \times 41 \times 40$. The size of the chargeable body is $250 \times 250 \times 200$ m and
17 the top boundary is located 50 m below the surface. The EMTDIP code (Marchant et al. 2014) is used
18 to compute forward ATEM responses that include IP effects. The survey consisting of 11 soundings
19 along each of 11 lines is shown in Fig. 3(a). Data are from a coincident-loop system and the flight
20 height is 30 m above the surface; the radius of the loop is 10 m. A step-off transmitter waveform is
21 used and the range of the observed time channels is 0.01-60 ms. The observed responses can be the
22 vertical component of \vec{b} or $\frac{\partial \vec{b}}{\partial t}$.

23 In this section, we first decompose the observed responses and the total currents into fundamental
24 and IP portions to aid in the basic understanding of IP effects in ATEM data. Second, we validate the
25 linearized functional by computing the approximate IP current and IP responses, and compare these
26 with the true values. Third, we invert the IP data and recover 3D distributions of pseudo-chargeability
27 at multiple times. Lastly, we use the recovered pseudo-chargeabilities to examine the potential to
28 extract intrinsic Cole-Cole parameters.

29 **7.1 IP responses**

30 Using the EMTDIP code and carrying out two simulations, we compute the IP data via subtraction in
31 eq. (16). Fig. 4 shows the observed, fundamental, and IP responses at a sounding location above the
32 center of the chargeable body for (a) canonical, (b) conductive and (c) resistive models. Both b_z and
33 $-\frac{\partial b_z}{\partial t}$ data are shown. The IP effects are most noticeable for the conductive body and we turn attention
34 to this example first. The IP response starts to significantly affect the observations near 0.6 ms and the
35 observed responses show a sign reversal near 1 ms. Beyond that time the signal is dominated by the IP.
36 The dashed line in Fig. 4(b) shows that after turning off the transmitter current, the IP current increases
37 (as inferred by the magnitude of the b_z field) until about 1 ms and then decreases. We interpret this
38 in terms of charging and discharging phases and a vertical dashed line in the figure defines the two

14 *Seogi Kang and Douglas W. Oldenburg*

1 phases. In the charging phase at early times the EM effects dominate and IP signals are not expected
2 to be observed. In the discharging phase, which occurs at later time, the IP effects may eventually
3 dominate the EM effects. The maximum of the b_z^{IP} corresponds to the zero crossing for $-\frac{\partial b_z^{IP}}{\partial t}$ but
4 the times at which the IP signal becomes dominant are delayed compared to b_z^{IP} . By comparing the
5 observations with the fundamental fields we see that the IP signal could be recognized in the b_z data
6 near 0.7 ms and near 2.0 ms in the $-\frac{\partial b_z}{\partial t}$ data.

7 The plots for the canonical and resistive bodies show that the time that separates charging and dis-
8 charging occurs earlier than for the conductive body. This is a reflection that the fundamental currents
9 reside for a longer time in a conductor. For the canonical body, a significant difference between the
10 measured responses and the fundamental fields occur about 0.9 ms for b_z and about 2 ms for $-\frac{\partial b_z}{\partial t}$.
11 The amplitudes of the IP responses are significantly smaller than those for the conductor. Lastly, there
12 is little IP signal for the resistive body; the IP signal is much smaller than the fundamental response
13 throughout the given time range. This is a consequence of the small fundamental currents in the resis-
14 tor.

15 The decay curves from a sounding location provide insight about the IP response but more is
16 gleaned by looking at data from all sounding locations in the ATEM survey. We focus on b_z^{IP} for the
17 conductive block at selected time channels. Fig. 5 shows interpolated maps of the observed, funda-
18 mental and IP responses at (a) 0.86 ms and (b) 6.7 ms which are respectively included in the charging
19 and discharging times. For the conductive block, 0.86 ms is close to the peak time when transition
20 from charging to discharging occurs, but it is still included in the charging time. At this time, the ob-
21 servations are dominated by the fundamental response and no negative values, which are the signature
22 of the IP effect, are observed. Subtracting the fundamental however, yields a residual d^{IP} data map
23 that has a strong negative. This example shows that our EM-decoupling procedure can work satisfac-
24 torily. At 6.7 ms, obtaining good IP data are easier because the observed data already show negative
25 values. There is still a weak fundamental field and the subtraction process improves the d^{IP} response.
26 The d^{IP} data at 0.86 ms and 6.7 ms shown in Fig. 5 are of sufficient quality to be inverted.

27 **7.2 Polarization currents**

28 To evaluate the polarization current shown in eq. (19) for the linear functional, we assumed $\vec{e}(t) \approx$
29 $\vec{e}^{ref} w^e(t)$ and defined our reference current as $\vec{j}^{ref} = \sigma_\infty \vec{e}^{ref}$. That yielded our approximation of
30 the polarization current to be $\vec{j}^{pol}(t) \approx -\vec{j}^{ref} \tilde{\eta}(t)$. This approximation requires that the polarization
31 current has a direction antiparallel to the reference current, and the direction is the same for all times.
32 With this approximation the time dependence for the polarization currents only occurs through the
33 scalar $\tilde{\eta}(t)$. We investigate the approximation by evaluating both reference and polarization currents

On recovering distributed IP information from inductive source time domain electromagnetic data 15

numerically. From eq. (22), a reference current can be considered as the maximum fundamental current that occurred throughout the time history. To evaluate polarization currents we rearrange eq. (18) as

$$\vec{j}^{pol} = \vec{j}^{IP} - \sigma_\infty \vec{e}^{IP}.$$

Here we limit our attention to canonical and conductive blocks. Figs 6(a) and (b) show reference currents for the canonical and conductive blocks, respectively. A transmitter is located at (-200 m, 0 m, 30 m) and marked as a white solid circle in the figure, where (\cdot, \cdot, \cdot) refers to a point at (easting, northing, depth). Reference currents for the canonical block are circular, centered on the transmitter location, and decay with distance. For the conductive block, additional vortex currents are induced. We compare these reference currents with the polarization currents. Fig. 7 shows the plan and section view maps of the polarization currents at 0.86 ms. Comparisons of Figs 6 and 7 clearly show that polarization currents for both canonical and conductive blocks are oppositely aligned with respect to their reference current. This was the hypothesized outcome. Fig. 8 shows that the direction of polarization currents at 6.7 ms is similar to those at 0.86 ms. Thus both for the canonical and conductive blocks, the direction of polarization currents after 0.86 ms is constant in time.

Of particular interest is the difference in character of the polarization currents for the canonical and conductive bodies. For the canonical body the currents look like anomalous galvanic currents that would be expected from an EIP survey. The resultant magnetic fields will be similar to the magnetic fields obtained from an electric dipole. For the conductive case however, the currents are circular and they reflect the vortex nature of the induced currents. The resultant magnetic fields are those associated with a magnetic dipole. The polarization currents inside a body are therefore complicated by the fact that they are a mixture of galvanic and inductive processes. Our choice of reference currents effectively incorporates this complexity.

7.3 IP currents

The IP currents, as provided in eq. (18), are given as

$$\vec{j}^{IP} = \sigma_\infty \vec{e}^{IP} + \vec{j}^{pol}. \quad (47)$$

In most analyses, e.g. Smith et al. (1988), the term $\sigma_\infty \vec{e}^{IP}$ is neglected. We have included this term but with an approximation that $\vec{e}^{IP} \approx -\nabla\phi$ (eq. 32). Here we investigate these approximations, and under what circumstances they hold.

Using the forward modelling we can evaluate \vec{e}^{IP} . This field can be broken into galvanic and inductive parts using the Helmholtz decomposition (Bladel 1959): $\vec{e} = -\vec{\nabla}\phi - \vec{a}$ so that $\vec{j}^{IP} = \vec{j}^{pol} - \sigma_\infty \vec{\nabla}\phi^{IP} - \sigma_\infty \vec{a}^{IP}$. In our work we included the effects from the scalar potential but neglected any contribution from the vector potential. We look at the contributions of each of these terms for the

16 *Seogi Kang and Douglas W. Oldenburg*

1 three cases of canonical, conductive and resistive bodies. Fig. 9 respectively shows plan view maps of
2 \vec{j}^{pol} , $-\sigma_\infty \vec{\nabla} \phi^{IP}$, and $-\sigma_\infty \vec{a}^{IP}$ for (a) canonical, (b) conductive, and (c) resistive models at 0.86 ms.

3 Inside the body, the polarization currents have the greatest strength and the strength of these cur-
4 rents is largest in the conductive body and smallest in the resistive body. In all cases, the polarization
5 currents are the largest contribution to \vec{j}^{IP} . The second column in Fig. 9 is related to the scalar poten-
6 tial for the electric field or effectively to the galvanic currents. These exist both inside and outside the
7 chargeable body. Again, these are largest for the conductive body. We note that inside the body, these
8 currents have a direction that is opposite to the polarization currents. The third column is associated
9 with the vector potential for \vec{e}^{IP} and is associated with vortex currents. The effects of these currents
10 have not been included in our linearized approximations. These currents are quite small for the canon-
11 ical and resistive models but their amplitude starts to be comparable to the galvanic portion for the
12 conductive model.

13 We evaluate \vec{j}^{IP} and its components at two locations in the body for conductive model. These are
14 denoted by white stars in the figures. For both locations, the polarization currents have the greatest
15 strength and the vortex currents are smaller than the galvanic currents. The IP current is smaller than
16 the polarization current mostly because the galvanic IP currents are in the opposite direction compared
17 to the polarization currents. The results are tabulated in Table 1.

18 The above figures provide insight about the three contributions to \vec{j}^{IP} but of ultimate interest is the
19 effect of these currents on the measured data. We therefore apply the Biot-Savart law to each current. It
20 suffices to work with the conductive case. Fig. 10 shows IP responses computed from the polarization
21 current (stars), galvanic (rectangles) and inductive portions (circles) of the IP current. Here solid and
22 empty markers show negative and positive signs, respectively. The polarization current has the major
23 contribution to the IP response although it is larger than the true value. This overshoot is primarily
24 negated by the galvanic portion of IP responses and further reduced because of the vortex currents.
25 We notice that the contribution of the galvanic currents is generally larger than those due to the vortex
26 currents except near 0.4 ms. At 6.7 ms, the amplitude of the IP response due to the polarization current
27 is about 130 percent of the true one, while galvanic portion is 30 percent. These results show that the
28 assumption by Smith et al. (1988) is reasonable, but incorporation of the galvanic portion to the IP
29 datum is significant at later times. The inductive portion of the IP responses is small compared to the
30 galvanic portion except for the time before 0.2 ms, and hence ignoring this is generally justified.

31 **7.4 Validations of linearization**

32 Forward modelling using eq. (39) requires that we have adequately estimated the IP currents and we
33 can evaluate their response using the Biot-Savart law. To validate this we first compute approximate

1
2
3 *On recovering distributed IP information from inductive source time domain electromagnetic data* 17
4
56 IP currents using eq. (35), and first compare them with the true IP currents. It suffices to work with
7 the conductive model which is the most challenging. Fig. 11 compares the true and approximate IP
8 currents at 0.86 ms. The approximate IP currents match well, both in direction and amplitude, with
9 the true IP currents both inside and outside the body. As shown in Fig. 12 the agreement improves
10 as time increases (see the directions of the true and approximate IP currents at (0,0,-350) on the right
11 panels of Figs 11 and 12).
12
1314 We next test the validity of the computation of IP responses by using our formulation of the Biot-
15 Savart law. To do this we compute the “true” IP responses by subtracting the fundamental response
16 from the observations. We next compute the IP responses by evaluating the Biot-Savart law with the
17 true IP currents shown in Fig. 12(a). As shown in Fig. 13 the agreement between these responses
18 is very good after 0.01 ms. This validates the use of the Biot-Savart law (eq. 37). Lastly, we want
19 to compare responses, evaluated through the Biot Savart law, but use our approximated IP currents
20 (Fig. 12b). The results are shown in Fig. 13. The responses obtained from using our approximate
21 currents have lower amplitude and differ by 33 percent at the extreme. The difference decreases with
22 increasing time. Overall the two curves are in reasonable agreement, thus validating our linearized
23 forward modeling (eq. 39).
24
2526 The same analysis of comparing true and approximate d^{IP} data was carried out for the canonical
27 and resistive models. As shown in Fig. 13, the true and approximate d^{IP} for both cases show good
28 agreements. We note however, that despite the fact that our linear functional reasonably explains d^{IP}
29 data for the resistive case, the IP signals are very small compared to EM signals and we likely cannot
30 identify them in practice.
31
3240
41
42
43
44 **7.5 3D IP inversions**
4546 Using our linearized sensitivity, we now proceed with 3D IP inversion, which recovers a pseudo-
47 chargeability given by eq. (39). We limit our attention to the conductive case. For the computation of
48 the sensitivity we use the true conductivity (σ_∞) and then invert data at successive time channels and
49 recover 3D pseudo-chargeability at multiple times. Our 3D inversion is based upon (Oldenburg & Li
50 1994; Li & Oldenburg 2000), and it requires some choices for inversion parameters.
51
5253 For data uncertainties, we use one percent of the maximum amplitude of the observed data ($0.01\max(|\mathbf{d}^{obs}|)$).
54
55 Coefficients for smallness and smoothness are set to $\alpha_s = 10^{-5}$ and $\alpha_x = \alpha_y = \alpha_z = 1$, respec-
56 tively. The reference model is zero, which means the pseudo-chargeability of every cell is zero, and
57 we applied a depth weighting. The need for a depth weighting arises because the sensitivity function
58 J is primarily controlled by a $1/r^3$ decay associated with the Biot-Savart kernels. Thus an ATEM data
59
60

18 *Seogi Kang and Douglas W. Oldenburg*

1 set is not unlike a magnetic data set where it is well established that a depth weighting is required to
2 image objects at depth. The following example illustrates this.

3 We first generate IP responses at a single time using the linear functional and specifying that
4 the pseudo-chargeability is unity inside the body and zero outside, as shown in Fig. 14(a). Fig. 14(b)
5 shows the recovered pseudo-chargeability without depth weighting. The recovered anomalous pseudo-
6 chargeability is concentrated near the surface and the magnitude of the pseudo-chargeability is under-
7 estimated; it is ~ 0.2 rather than unity. By using the depth weighting shown in eq. (46), the IP body is
8 imaged closer to its true depth (Fig. 14b). Also, the magnitude of the recovered pseudo-chargeability
9 (~ 0.6) is closer to the true value than the result without depth weighting. Based on this analysis, we
10 use the same depth weighting for our following examples.

11 *7.5.1 Incorrect conductivity*

12 The background conductivity σ_∞ plays a central role in our analysis. It is used in the EM-decoupling
13 process and it is also needed to compute the linearized sensitivities for inversion. Since we need to
14 estimate σ_∞ , usually through the inversion of TEM data, it will never be correct. Here we explore
15 some effects of an incorrect conductivity but the consequences are problem dependent.

16 We return to our conductive block in a halfspace and evaluate the d^{IP} data when the background
17 is the true value ($\sigma_1 = 10^{-3}$ S/m) as well as a factor of two too large (2×10^{-3} S/m) and a factor of
18 two too small (5×10^{-4} S/m). The data along a survey line are plotted in Fig. 15.

19 We invert these three IP responses, and provide sections of the recovered pseudo-chargeability at
20 0 m-northing. Fig. 16(a), (b) and (c) correspondingly show the recovered pseudo-chargeability when
21 the conductivity is: the true value, too high, or too low. With the correct conductivity the geometry
22 of the IP body is reasonably recovered. When the conductivity is too high, the d^{IP} have a negative
23 bias that results in larger pseudo-chargeabilities and positive-valued artifacts near the IP body (Fig.
24 16b). When the conductivity is too small, the IP data have a positive bias and this produces negative-
25 valued artifacts near the IP body (Fig. 16c). White dotted contours shown in Fig. 16(c) shows zero-
26 crossing lines, which delineate those negative-valued artifacts. However, based on the definition of the
27 pseudo-chargeability shown in eq. (A.5), the sign of the pseudo-chargeability should be positive. By
28 incorporating positivity as a constraint in the inversion, and re-inverting the IP data that have a positive
29 bias, we obtain the result in Fig. 16(d). This is a much better result than Fig. 16(c), and it shows that
30 the positive constraints prevent fitting positive residual fields. We shall use this positivity constraint
31 for our following 3D IP inversion examples.

32 The background conductivity is also needed when computing the sensitivity function, since we
33 need the reference electric field, which is dependent on conductivity. An incorrect conductivity will

4
3 *On recovering distributed IP information from inductive source time domain electromagnetic data* 19
51 then affect the sensitivity function. In order to test this, we compute the sensitivity matrix using a
2 halfspace conductivity model ($\sigma_\infty = \sigma_1$). Fig. 17 compares the recovered pseudo-chargeability from
3 the 3D IP inversion of the IP datum at 0.86 ms with the true and incorrect sensitivity function using
4 halfspace conductivity. There is not a large difference between the two inversions which suggests
5 that an approximate conductivity may still provide sensitivities that are adequate for inversion. This
6 parallels results from EIP where even an approximate conductivity can still yield good results when
7 inverting the data. Thus there is robustness in our sensitivity function with respect to an incorrect
8 conductivity.
919
20 7.5.2 *Extracting intrinsic IP parameters*
2122
23 By applying our inversion to each time channel of d^{IP} data separately, we can recover 3D distri-
24 butions of pseudo-chargeability at multiple times. The pseudo-chargeability at each time carries dif-
25 ferent information about the state of polarization and we can use these to recover information about
26 intrinsic IP parameters. Diverse time-dependent conductivity models such as the Cole-Cole model and
27 stretched-exponential can be used for this interpretation. We use the Cole-Cole model with $c = 1$. We
28 parametrize pseudo-chargeability at a single pixel in terms of chargeability and time constant as de-
29 scribed in Appendix B, and solve a small inverse problem. In previous works about this task for the
30 EIP problem (Yuval & Oldenburg 1997; Hördt et al. 2006), the convolution shown in eq. B.1 was not
31 explicitly mentioned because $\hat{w}(t)$ is a step-off or -on function and it does not change for different
32 cells and transmitters. This allowed an explicit equation for a step-off or -on response of the pseudo-
33 chargeability to be derived. However, in our work, convolution plays a fundamental role and needs to
34 be explicitly addressed when extracting intrinsic IP parameters. Also, the details regarding how we
35 defined the effective pseudo-chargeability (eq. A.8) needs to be included. Except for this additional
36 complexity related to the convolution, our approach parallels that of Yuval & Oldenburg (1997); Hördt
37 et al. (2006).
3839
40 As an example, we use the conductive and chargeable block presented in the previous section
41 and invert 14 time channels of data ranging from 1-10 ms. The EM data are forward modelled using
42 EMTDIP code and the true σ_∞ model is used to evaluate the IP datum and compute the sensitivity
43 function. The recovered pseudo-chargeability from one of the 14 inversions is shown in Fig. 17a. In
44 that pseudo-chargeability model, we select cells that have a pseudo-chargeability value greater than
45 0.001, and then carry out the nonlinear inversion to estimate the time constant, τ , and chargeability,
46 η , for each cell separately. The forward modelling for this inversion is shown in eq. (A.8), which
47 requires $w^e(t)$ (eq. A.9). The $w^e(t)$ for a pixel in the block is shown in Fig. A2.
4849
50 Fig. 18(a) and (b) correspondingly show the estimated time constants and chargeability as section
51

1
2
3 20 *Seogi Kang and Douglas W. Oldenburg*
4
5
6
7
8
9
10
11
12
13
14
15
16
17
18
19

maps. The estimated time constants show good agreement with the true value $\tau = 0.005$. There is less agreement about chargeability for which the true value is $\eta = 0.2$. Recovered values range from about 0.04-0.2 so most values are underestimated. In Fig. 19, we also provide time decays of the observed and predicted pseudo-chargeabilities at a single pixel marked as a black empty rectangle in Fig. 18. The estimated time constant, τ_{est} , and chargeability, η_{est} , for this pixel are 0.0046 and 0.09, respectively. These results imply there is greater stability on recovering the time constant than on recovering chargeability with our approach. Again, similar experiments were carried out for the canonical and resistive bodies and the conclusions were also that the time constant was adequately recovered with better fidelity than was the chargeability.

20
21
22
23
24
25
26
27

10 8 ESTIMATING THE BACKGROUND CONDUCTIVITY

28
29
30
31
32
33
34
35
36
37
38
39
40
41
42
43
44
45
46
47
48
49
50
51
52
53
54
55
56
57
58
59
60

In this paper we have generally assumed that a good estimate of σ_∞ was available. If it is, then we have shown that we can obtain IP data by subtracting the fundamental responses from the observations. This process is sometimes referred to as EM-decoupling and its solution has been a long-standing goal in exploration geophysics. For the ATEM survey, one potential approach to finding σ_∞ is to invert the early-time data in which the EM response is much larger than the IP response (for example inverting time channels 2 to 10 ms in the left panel of Fig. 4b). The success of this method is dependent upon three factors: (a) that the data are uncontaminated by IP effects (i.e. there is no IP-coupling); (b) that the data acquisition is sufficiently dense in space and in time so that needed information about σ_∞ is obtained; (c) an inversion algorithm exists that can generate a 3D conductivity model. Even so, the recovered conductivity will not be equal to the true conductivity. In Section 7.5.1, we showed how the estimated IP data are affected when a background halfspace is altered by a factor of two. This was a simple example but it illustrated the general effects of an incorrect conductivity and ameliorating effects of the positivity constraint in the IP inversion (eq. 43). The problem will become more challenging when there is substantial spatial variation between the true and approximate conductivity. It is conceivable that if the ATEM data show no negative values and if the conductivity approximation is sufficiently poor then our EM-decoupling procedure will fail to produce quality IP data. This will have to be addressed for each survey. What we did demonstrate here was that even an approximate σ_∞ is sufficient to generate the sensitivities, and hence if quality IP data can be isolated from observations, then our techniques can unravel the data to generate information about the polarization structure.

1
2
3 *On recovering distributed IP information from inductive source time domain electromagnetic data* 21
4
5

6 **9 CONCLUSIONS**
7

8 In this paper, we have introduced a procedure for recovering IP information from TEM data with
9 inductive sources. Three main steps are required: 1) subtraction of the fundamental responses from
10 the observations to generate IP data, 2) linearization of the IP responses as a function of the pseudo-
11 chargeability, and 3) restoration of 3D pseudo-chargeability at multiple times, and further interpreta-
12 tion of the pseudo-chargeability to extract intrinsic IP parameters like Cole-Cole model. We used the
13 ATEM survey to test our IP inversion procedure.
14
15

16 The first step requires a good estimate for the background conductivity σ_∞ . This is important for
17 two reasons. σ_∞ is used to generate the fundamental fields that are subtracted from the observations
18 to produce the IP data. This conductivity is also needed to compute the sensitivities for our linear
19 relationship between the IP data and pseudo-chargeability. To construct σ_∞ we invert early time data
20 that is felt to be uncontaminated with significant IP responses. For the mid-time data, subtraction of
21 the fundamental responses from the observations revealed negative data even though the observations
22 were positive. At very late times this subtraction process was not necessary since the EM fields had
23 sufficiently decayed. We note that maps of the d^{IP} data can, in themselves, be a useful processing
24 tool for detecting anomalies. To carry out that analysis we assumed that σ_∞ was known. For practical
25 applications, where we propose inverting early TEM data to recover σ_∞ , the effects on an incorrect
26 σ_∞ on the d^{IP} data will need to be investigated.
27
28

29 The second item, linearization of the IP responses with respect to a pseudo-chargeability, required
30 that a number of assumptions be made. Our pseudo-chargeability is defined as the ratio of the polar-
31 ization current to a reference current. Unlike the EIP case, the electric fields for an inductive source
32 do not achieve steady-state and hence neither do the polarization currents. To address this important
33 difference we evaluate the fundamental fields at each location in the earth and generate a reference
34 electric field that has the direction and magnitude of the field at the time when the fundamental field
35 reaches its maximum value. The pseudo-chargeability at a point in the earth thus depends upon the
36 chargeability, the reference electric field, and the time history of the fundamental electric field. The sit-
37 uation becomes more complicated when data from many transmitters are to be inverted simultaneously
38 because the time history of the electric field at a point in the earth is different for each transmitter. We
39 handle this by defining an effective pseudo-chargeability and an associated reference electric field that
40 accommodates, in a least squares fashion, the effects of all transmitters acting on a single cell.
41
42

43 To have confidence in when, and under what circumstances, our approximations are sufficiently
44 valid, we proceed with a number of rigorous tests. First we introduce 3 test models which are respec-
45 tively a chargeable block in a halfspace. The block can be conductive, canonical, or resistive with
46 respect to the background. Our evaluations show that: (a) our choice of reference electric field and
47
48

1
2
3 22 Seogi Kang and Douglas W. Oldenburg
4
5

6 its time history produces a good estimate of the polarization currents; (b) the IP currents are domi-
7 nated by the polarization currents, which is an assumption that is often made. However, the galvanic
8 and vortex currents arising from the scalar and vector potentials in the Helmholtz decomposition of
9 \bar{e}^{IP} can be significant in some circumstances. The galvanic currents are the second most important
10 contribution to the IP currents and, in the body, they have a direction that opposes the direction of
11 the polarization currents. In our work we have included the galvanic currents and neglected the vor-
12 tex currents which are almost always smaller than the galvanic currents; (c) the IP responses can be
13 accurately evaluated using the Biot-Savart law provides accurate results; (d) with our approximate IP
14 currents, the predicted responses are in reasonably good agreement with true values although they are
15 underestimated for the highly conductive example. These results lead us to infer that our linearized
16 formulation $d^{IP}(t) = J\tilde{\eta}(t)$ is a viable representation for the forward modelling at late times when
17 the IP effects are substantial compared to the EM effects. (e) For the multi-transmitter case we derived
18 an effective pseudo-chargeability which is a linear combination of the pseudo-chargeability of each
19 transmitter. These were forward modelled with the linearized formulation and compared to the true
20 responses. The values were underestimated for the conductive model but were almost identical for the
21 canonical and resistive models.
22
23

24 The third component is the 3D inversion of the IP data using the linearized formulation to recover
25 an effective pseudo-chargeability for each cell. ATEM data have only one receiver for each transmitter
26 and a data map at a single time channel is essentially a potential field. The data do not have intrinsic
27 resolving power and hence, as in magnetics or gravity inversions, we attempt to counteract this by in-
28 troducing a depth weighting. When this is done, our 3D IP inversion recovers a reasonable geometric
29 shape and location of the chargeable body but the amplitude is underestimated. For the inversion it
30 is assumed that a good estimate of σ_∞ is available. An incorrect σ_∞ has two effects in the inversion.
31 Firstly it can generate errors in the d^{IP} data because the fundamental field, which is subtracted from
32 the observations, is incorrect. To obtain insight we looked at the effects when σ_{est} was too low or two
33 high. This respectively yielded positive or negative residual fields in the IP response. A positivity con-
34 straint on the pseudo-chargeability (similar to that used in EIP surveys) greatly ameliorated the effects
35 of the positive residuals. The other avenue by which an incorrect σ_∞ can affect the inversion is through
36 the sensitivity matrix J . We showed that, even with an approximate conductivity, we recovered impor-
37 tant information about the chargeable body such as geometric shape and location. An inversion of the
38 data at a particular time channel provides information about the effective pseudo-chargeability for each
39 pixel. Inversions carried out at multiple time channels therefore generates a pseudo-chargeability as a
40 function of time for each pixel. The pseudo-chargeability for pixels that had significant chargeability
41 were subsequently fit to a Cole-Cole model to estimate τ and η by assuming $c = 1$. The estimated τ
42
43
44
45
46
47
48
49
50
51
52
53
54
55
56
57
58
59
60

4 *On recovering distributed IP information from inductive source time domain electromagnetic data* 235 1 was close to the true value whereas η was underestimated and less robust. This suggests that there is
6 2 a possibility to extract intrinsic IP parameters from the recovered pseudo-chargeability from ATEM
7 3 surveys.8 4 Our IP inversion procedure provides a framework for recovering IP information from inductive
9 5 source EM surveys and in particular from ATEM surveys that are commonly flown. Our examples
10 6 show: (a) that the horizontal location of a target body can be well recovered; (b) the overall geometry
11 7 might be recovered but much of that inference requires a depth weighting to be included; (c) we can
12 8 recover estimates of intrinsic τ and η that may be useful for distinguishing between two chargeable
13 9 targets. Our procedure depends on having a good estimate for the background conductivity and this
14 10 aspect this should be carefully investigated in future practical applications. Other areas for follow-
15 11 up research include quantifying depth of resolution for airborne IP surveys, and general strategies
16 12 for extracting intrinsic IP parameters from our effective pseudo-chargeabilities. Lastly, our numerical
17 13 examples only treated the ATEM survey, but the procedure is applicable to other types of inductive
18 14 source TEM survey such as a large-loop TEM with many receivers. There will be details that need to
19 15 be addressed for those applications but the work presented here provides the fundamental background
20 16 for those future studies whose goal is to extract some information about polarization from an inductive
21 17 time domain system.33 18 **ACKNOWLEDGMENTS**34 19 We wish to thank David Marchant for providing EMTDIP code, and other UBC-GIF members for
35 20 their constructive comments. We would like to thank Rowan Cockett and Lindsey Heagy for their
36 21 contributions to SIMPEG (<http://www.simpeg.xyz>).43 22 **REFERENCES**

- 44 23 Bladel, J., 1959. On helmholtz's theorem in finite regions,
- Antennas and Propagation, IRE Transactions on*
- ,
-
- 45 24
- 7**
- (5), 119–119.
-
- 46 25 Chen, J. & Oldenburg, D., 2003. 3-D inversion of magnetic induced polarization data,
- ASEG Extended Ab-*
-
- 47 26
- stracts*
- ,
- 1**
- (1), 1–11.
-
- 48 27 Cockett, R., Kang, S., Heagy, L. J., Pidlisecky, A., & Oldenburg, D. W., 2015. SimPEG: An open source
-
- 49 28 framework for simulation and gradient based parameter estimation in geophysical applications (submitted),
-
- 50 29
- Computers and geoscience*
- .
-
- 51 30 Cole, K. S. & Cole, R. H., 1941. Dispersion and absorption in dielectrics i. alternating current characteristics,
-
- 52 31
- The Journal of Chemical Physics*
- ,
- 9**
- (4).

1
2
3 24 Seogi Kang and Douglas W. Oldenburg
4
5
6
7
8
9
10
11
12
13
14
15
16
17
18
19
20
21
22
23
24
25
26
27
28
29
30
31
32
33
34
35
36
37
38
39
40
41
42
43
44
45
46
47
48
49
50
51
52
53
54
55
56
57
58
59
60

- Dias, C. A., 2000. Developments in a model to describe lowfrequency electrical polarization of rocks, *GEO-PHYSICS*, **65**(2), 437–451.
- EIKalioubi, H. & Eldiwany, E., 2004. Transient electromagnetic responses of 3D polarizable body, *Geophysics*, **69**(2), 426–430.
- Fiandaca, G., Auken, E., Christiansen, A. V., & Gazoty, A., 2012. Time-domain-induced polarization: Full-decay forward modeling and 1D laterally constrained inversion of Cole-Cole parameters, *Geophysics*, **77**(3), E213.
- Fink, J., McAlister, E., Sternberg, B., Wieduwilt, W., & Ward, S., 1990. *Induced Polarization Applications and Case Histories*, Society of Exploration Geophysicists.
- Flis, M. F., Newman, G. A., & Hohmann, G. W., 1989. Inducedpolarization effects in timedomain electromagnetic measurements, *Geophysics*, **54**(4), 514–523.
- Haber, E., 2014. *Computational Methods in Geophysical Electromagnetics*, Society for Industrial and Applied Mathematics, Philadelphia, PA.
- Hodges, G. & Chen, T., 2014. IP effect in airborne TDEM data: Model studies and field examples, *SEG Technical Program Expanded Abstracts*, **158**, 828–832.
- Hördt, A., Hanstein, T., Hönig, M., & Neubauer, F. M., 2006. Efficient spectral IP-modelling in the time domain, *Journal of Applied Geophysics*, **59**(2), 152–161.
- Kang, S. & Oldenburg, D., 2015. Recovering IP information in airborne-time domain electromagnetic data, *ASEG Extended Abstracts*, **1**(1), 1–4.
- Kelley, C. T., 1999. *Iterative Methods for Optimization*, Society for Industrial and Applied Mathematics.
- Kemna, A., Binley, A., Cassiani, G., Niederleithinger, E., Revil, A., Slater, L., Williams, K. H., Orozco, A. F., Haegel, F. H., Hördt, A., Kruschwitz, S., Leroux, V., Titov, K., & Zimmermann, E., 2012. An overview of the spectral induced polarization method for near-surface applications, *Near Surface Geophysics*, **10**(6), 453–468.
- Kohlrausch, R., 1854. Theorie des elektrischen Rückstandes in der Leidener Flasche, *Annalen der Physik*, **167**(2), 179–214.
- Kratzer, T. & Macnae, J., 2012. Induced polarization in airborne EM, *Geophysics*, **77**(5), E317–E327.
- Li, Y. & Oldenburg, D., 1996. 3-D inversion of magnetic data, *Geophysics*, **61**(2), 394–408.
- Li, Y. & Oldenburg, D. W., 2000. 3-D inversion of induced polarization data, *Geophysics*, **65**(6), 1931–1945.
- Marchant, D., Haber, E., & Oldenburg, D. W., 2012. Inductive source induced polarization, *Geophysical Journal International*, **192**(2), 602–612.
- Marchant, D., Haber, E., & Oldenburg, D., 2013. Recovery of 3D IP distribution from airborne time-domain EM, *ASEG Extended Abstracts*, **144**, 1–4.
- Marchant, D., Haber, E., & Oldenburg, D., 2014. Three-dimensional modeling of IP effects in time-domain electromagnetic data, *Geophysics*, **79**(6), E303–E314.
- Nocedal, J. & Wright, S. J., 1999. *Numerical Optimization*, Springer, New York, NY.
- Oldenburg, D. & Li, Y., 1994. Inversion of induced polarization data, *Geophysics*, **59**(9), 1327–1341.

1
2
3 *On recovering distributed IP information from inductive source time domain electromagnetic data* 25
4
5

- 1 Oldenburg, D. W. & Li, Y., 2005. 5. *Inversion for Applied Geophysics: A Tutorial*, chap. 5, pp. 89–150.
- 2 Pelton, W., Ward, S., Hallof, P., Sill, W., & Nelson, P., 1978. Mineral discrimination and removal of inductive
3 coupling with multifrequency IP, *Geophysics*, **43**(3), 588–609.
- 4 Routh, P. S. & Oldenburg, D. W., 2001. Electromagnetic coupling in frequency-domain induced polarization
5 data: a method for removal, *Geophysical Journal International*, **145**(1), 59–76.
- 6 Seigel, H., 1959. Matehematical formulation and type curves for induced polarization, *Geophysics*, **24**(3),
7 547–565.
- 8 Seigel, H., 1974. The magnetic induced polarization (MIP) method, *Geophysics*, **39**(3), 321–339.
- 9 Smith, R. S. & Klein, J., 1996. A special circumstance of airborne inducedpolarization measurements, *Geo-
10 physics*, **61**(1), 66–73.
- 11 Smith, R. S., Walker, P., Polzer, B., & West, G. F., 1988. The time-domain electromagnetic response of
12 polarizable bodies: an approximate convolution algorithm, *Geophysical Prospecting*, **36**(April), 772–785.
- 13 Tarasov, A. & Titov, K., 2013. On the use of the Cole-Cole equations in spectral induced: Polarization,
14 *Geophysical Journal International*, **195**(1), 352–356.
- 15 Tikhonov, A. & Arsenin, V., 1977. *Solutions of Ill-Posed Problems*, W.H. Winston and Sons.
- 16 Weidelt, P., 1982. Response characteristics of coincident loop transient electromagnetic systems, **47**(Septem-
17 ber), 1325–1330.
- 18 Xu, Z. & Zhdanov, M., 2015. Three-Dimensional Cole-Cole Model Inversion of Induced Polarization Data
19 Based on Regularized Conjugate Gradient Method, *Geoscience and Remote Sensing Letters, IEEE*, **12**(6),
20 1180–1184.
- 21 Yee, K., 1966. Numerical solution of initial boundary value problems involving maxwell's equations in
22 isotropic media, *Antennas and Propagation, IEEE Transactions on*, **14**(3), 302–307.
- 23 Yuval & Oldenburg, D., 1997. Computation of Cole-Cole parameters from IP data, *Geophysics*, **62**(2), 436–
24 448.
- 41
42
43
44
45
46
47
48
49
50
51
52
53
54
55
56
57
58
59
60

1
2
3 26 *Seogi Kang and Douglas W. Oldenburg*
4
5
6
7
8
9
10
11
12
13
14
15
16
17
18
19
20
21
22
23
24
25
26
27
28
29
30
31
32
33
34
35
36
37
38
39
40
41
42
43
44
45
46
47
48
49
50
51
52
53
54
55
56
57
58
59
60

Table 1. Amplitudes of decomposed IP currents at two marked points (white stars) shown in Fig. 9(b). Units in A/m^2

Division	$ \vec{j}^{IP} $	$ \vec{j}^{pol} $	$ \sigma_\infty \vec{\nabla} \phi^{IP} $	$ \sigma_\infty \vec{d}^{IP} $
Left	1.5×10^{-10}	2.5×10^{-10}	7.6×10^{-11}	1.9×10^{-12}
Right	5.4×10^{-11}	1.2×10^{-10}	3.5×10^{-11}	3.3×10^{-11}

On recovering distributed IP information from inductive source time domain electromagnetic data 27

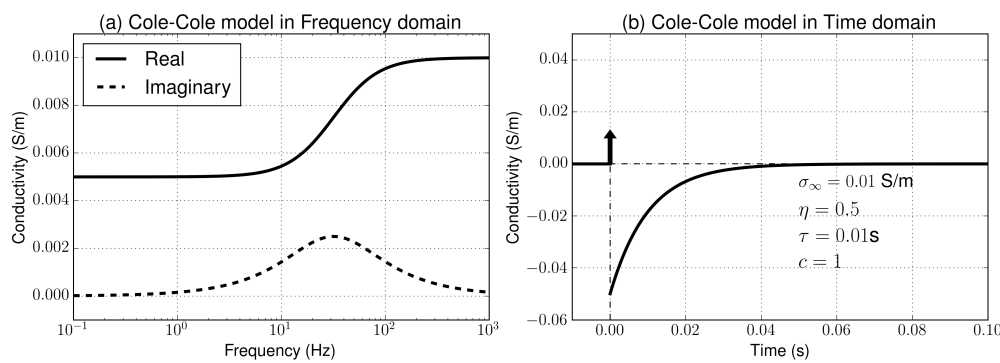


Figure 1. Cole-Cole response in frequency domain (a) and time (b) domain. The Cole-Cole parameters are $\sigma_\infty = 10^{-2} \text{ S/m}$, $\eta = 0.5$, $\tau = 0.01$, and $c=1$. The arrow shown in Fig. 1(b) indicates a delta function ($\sigma_\infty \delta(t)$).

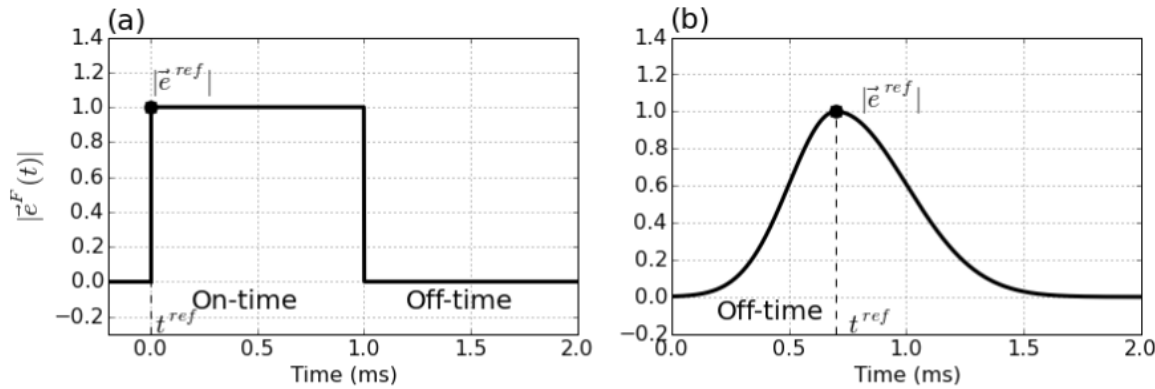
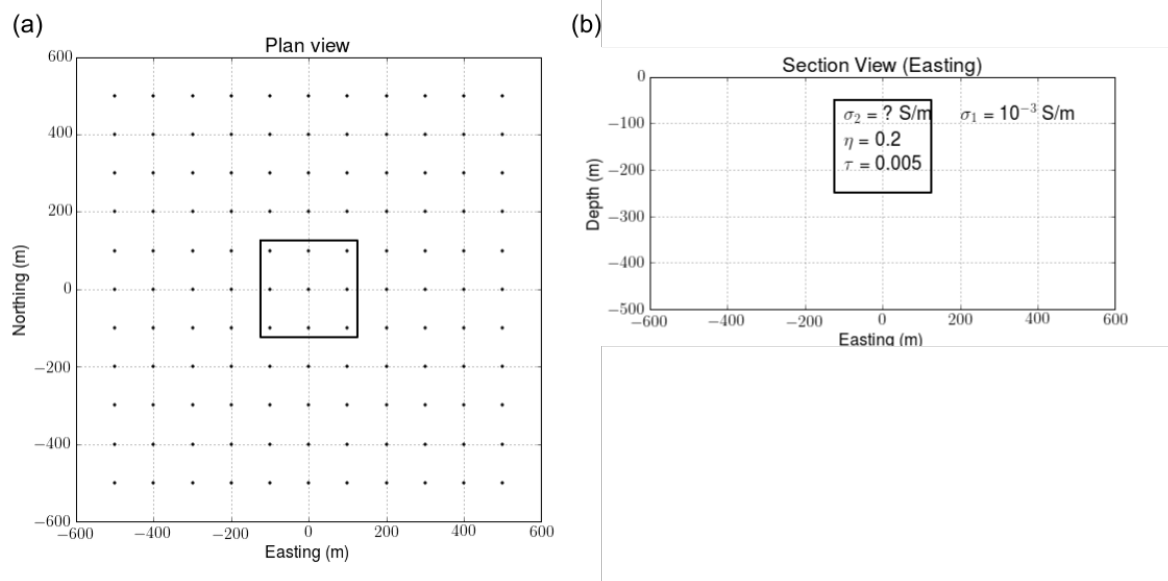


Figure 2. Conceptual diagram for the amplitude of the fundamental electric fields. (a) EIP and (b) ISIP cases.

1
2
3 28 Seogi Kang and Douglas W. Oldenburg
4
5
6
7
8
9
10
11
12
13
14
15
16
17
18
19
20
21
22
23
24
25



26 **Figure 3.** Plan (a) and section b) views of the IP model. The solid line in (a) delineates the boundary of the IP
27 body. Solid circles in (a) denote the sounding locations. In (b) the conductivity σ_2 is variable so that canonical,
28 conductive and resistive blocks can be examined
29
30
31
32
33
34
35
36
37
38
39
40
41
42
43
44
45
46
47
48
49
50
51
52
53
54
55
56
57
58
59
60

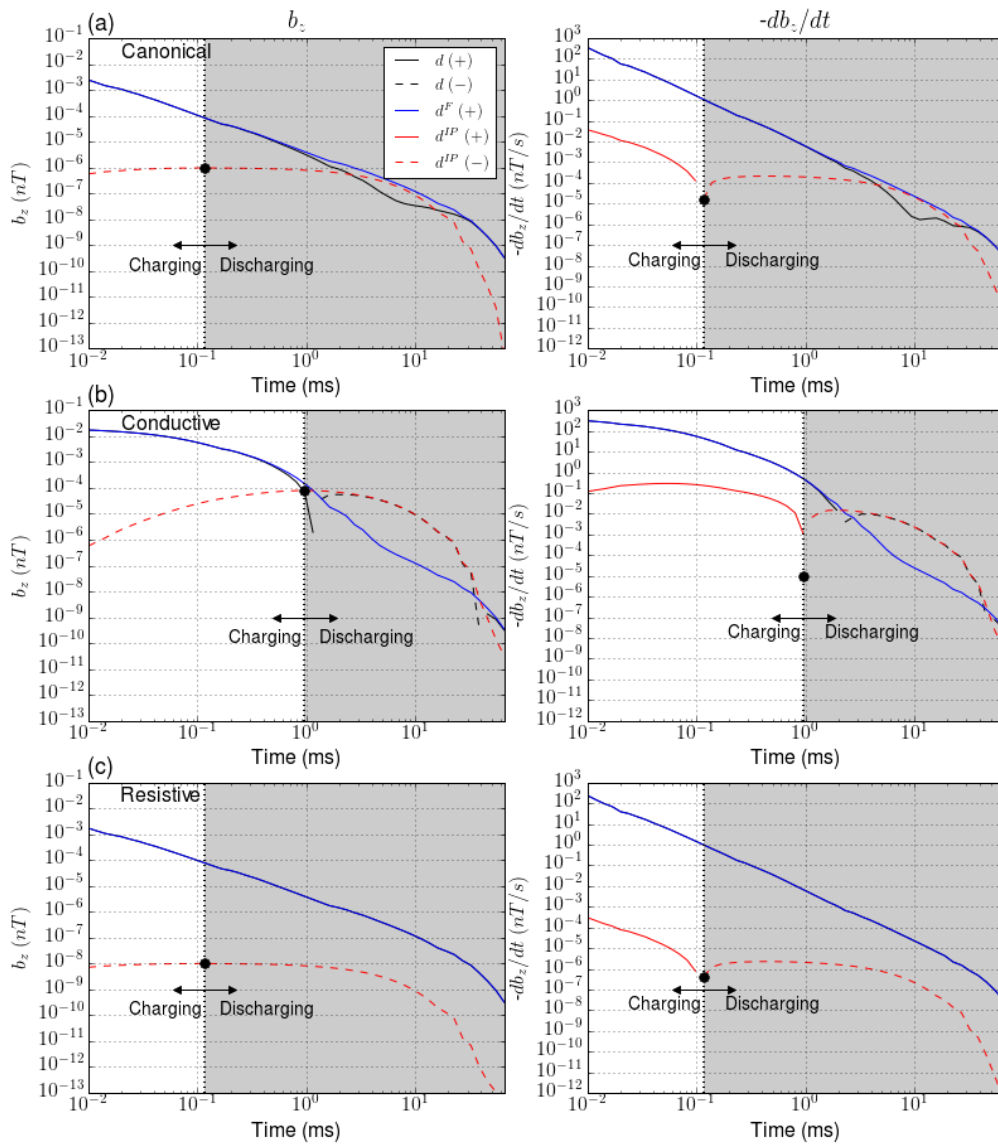


Figure 4. Time decaying curves of the observations (d ; black line), fundamental (d^F ; blue line) and IP (d^{IP} ; red line) responses. All three cases: (a) canonical, (b) conductive and (c) resistive are presented. Right and left panels show b_z and $-\frac{\partial b_z}{\partial t}$. The vertical black dotted line indicates the time at which the polarization field reaches its maximum value. The flight height of the collocated transmitting and receiving loop is 30 m above the surface.

30 Seogi Kang and Douglas W. Oldenburg

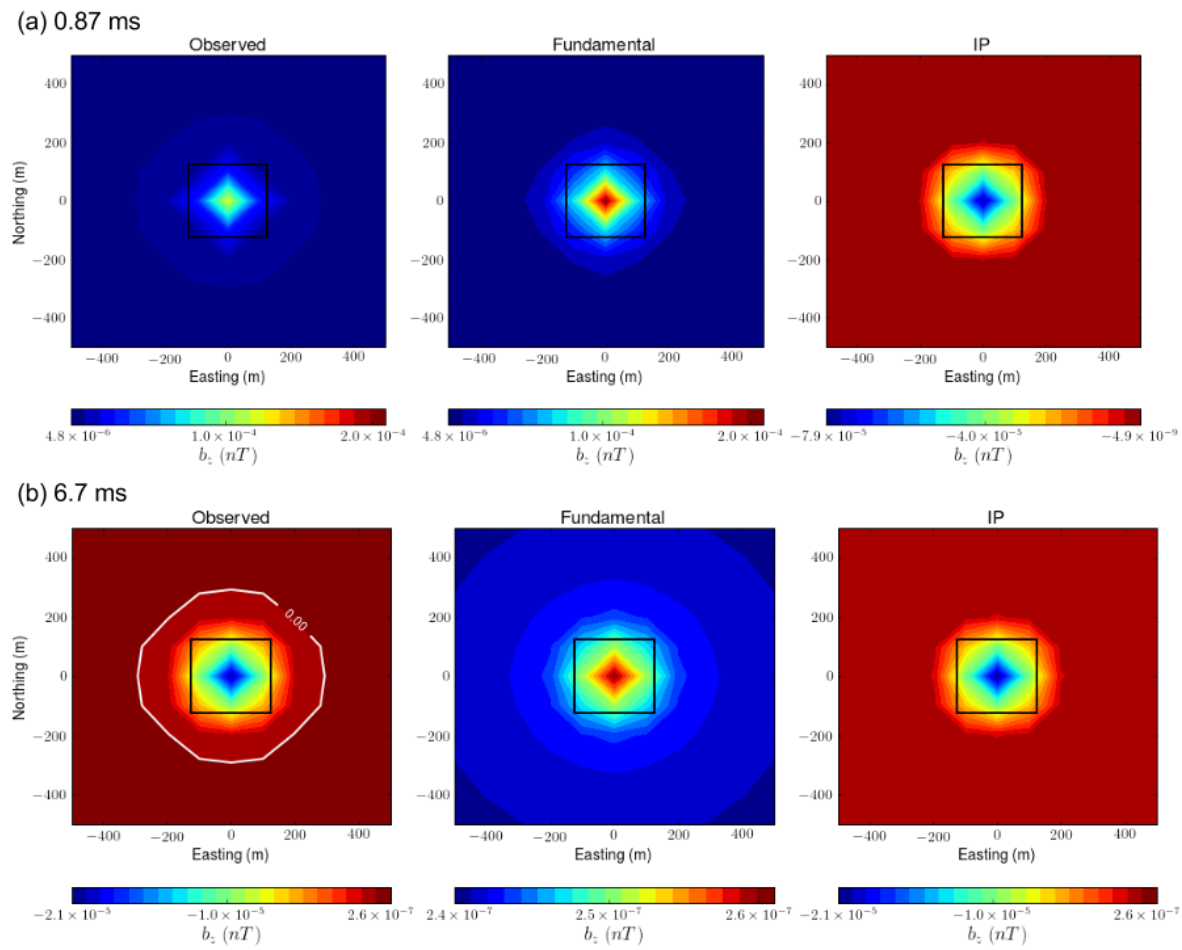


Figure 5. Interpolated maps of observed (left panel), fundamental (middle panel) and IP (right panel) responses. Two time channels at (a) 0.86 ms and (b) 6.7 ms are presented. White line contours a zero-crossing in the observed response.

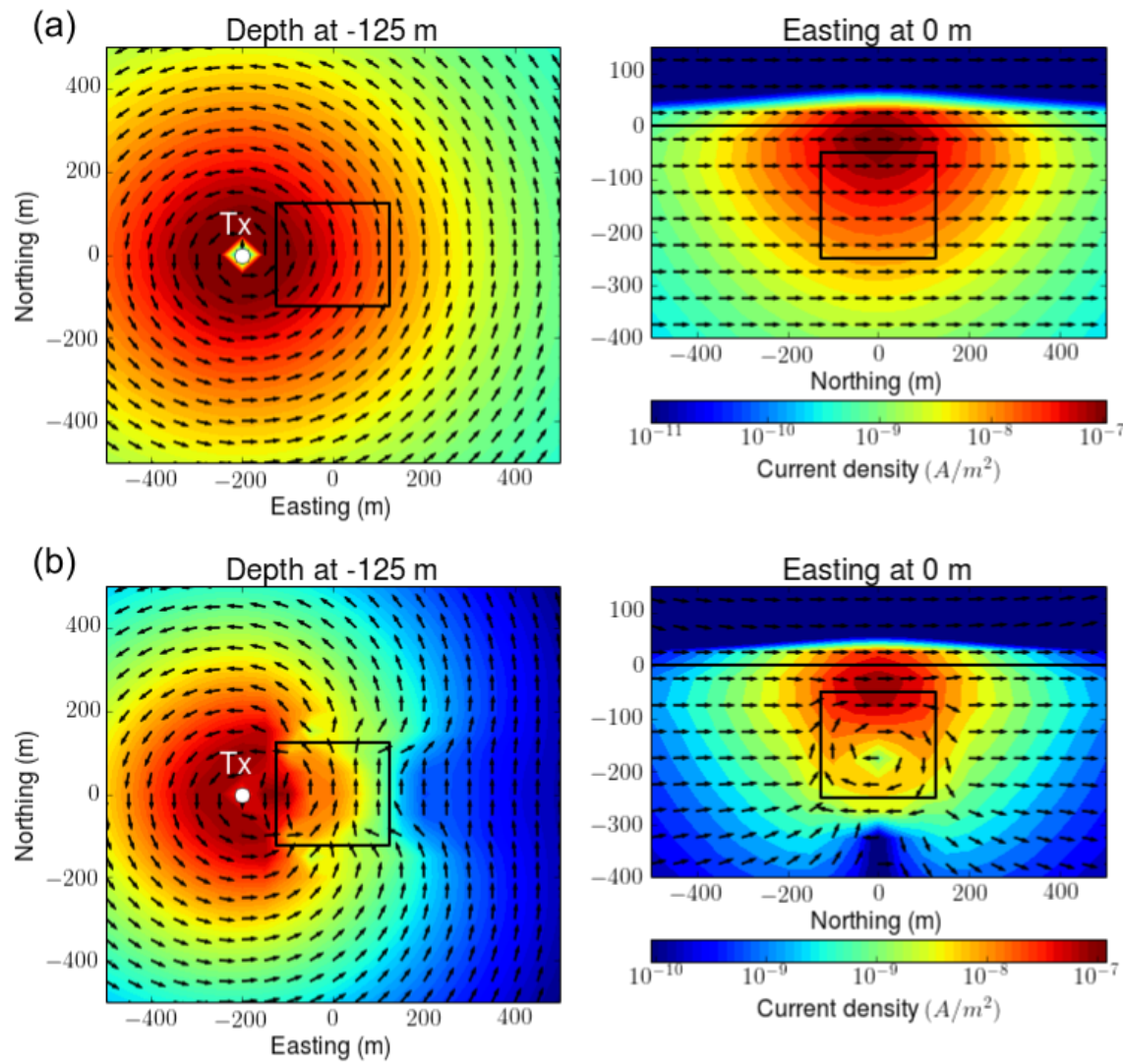


Figure 6. Maps of reference currents: (a) canonical and (b) conductive models. Left and right panels show plan and section views at -125 m-depth and 0 m-easting, respectively. A transmitter is located at (-200 m, 0 m, 30 m). Black arrows and colored background respectively indicate the direction and amplitude of the current. The black solid line outlines the boundary of chargeable body.

1
2
3
4 32 Seogi Kang and Douglas W. Oldenburg
5
6
7
8
9
10
11
12
13
14
15
16
17
18
19
20
21
22
23
24
25
26
27
28
29
30
31
32
33
34
35
36
37
38
39
40
41
42
43
44
45
46
47
48
49
50
51
52
53
54
55
56
57
58
59
60

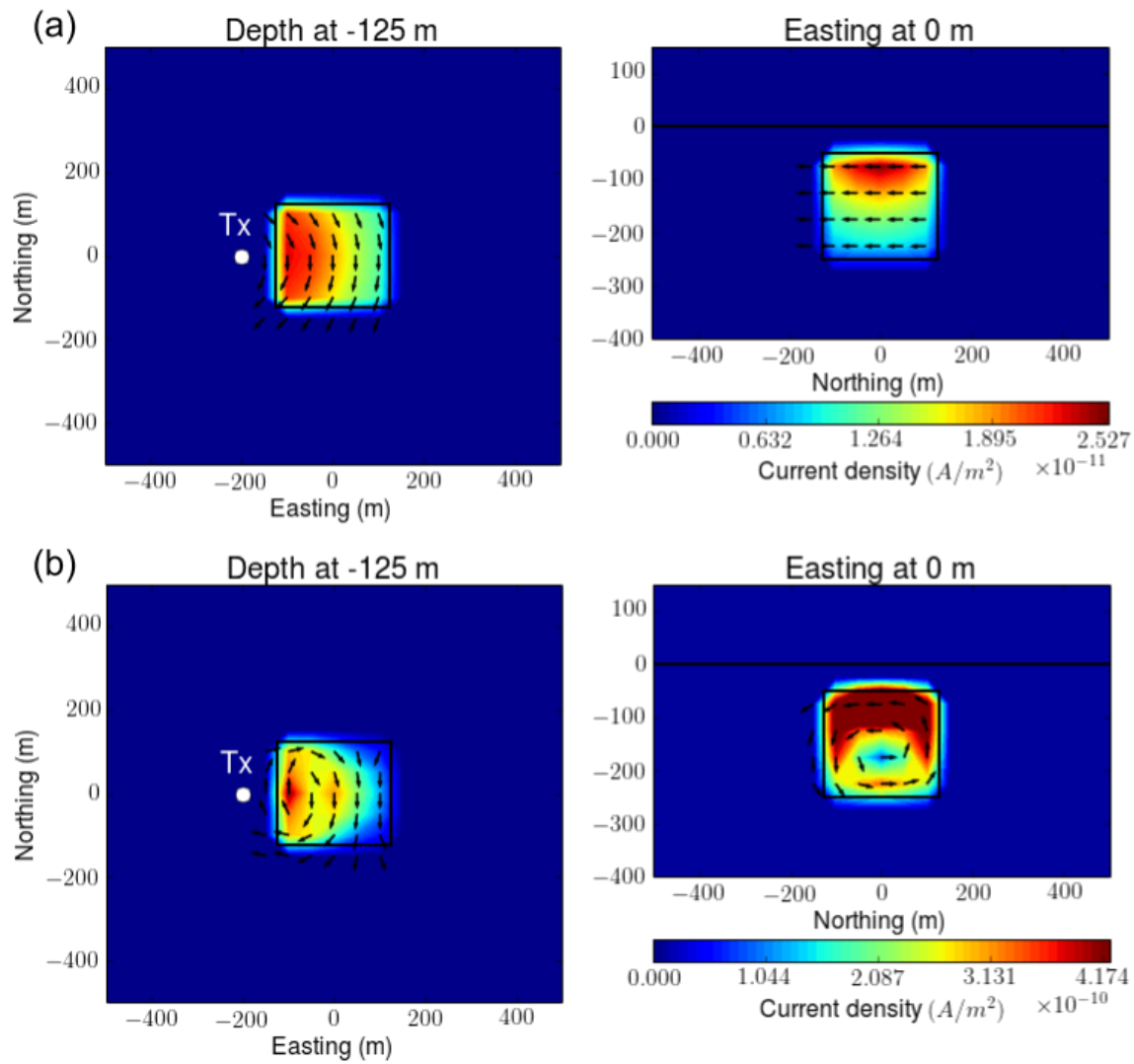


Figure 7. Maps of polarization currents: (a) canonical and (b) conductive models at 0.86 ms. Left and right panels show plan and section views at -125 m-depth and 0 m-easting, respectively. A transmitter is located at (-200 m, 0 m, 30 m). Black arrows and shaded values respectively indicate the direction and amplitude of the current. Black solid outlines boundary of the surface or the chargeable body.

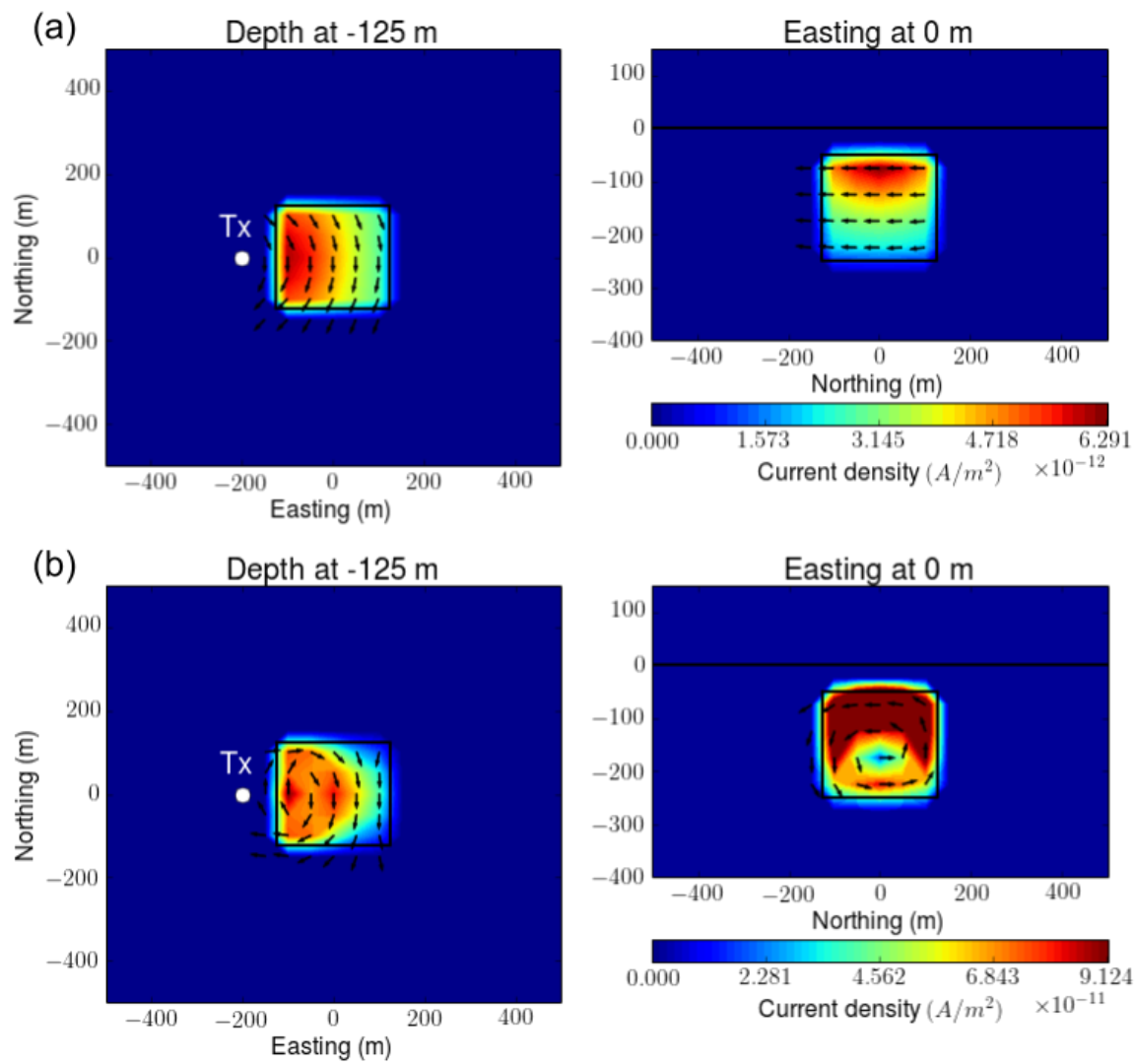


Figure 8. Maps of polarization currents: (a) canonical and (b) conductive models at 6.7 ms. Left and right panels show plan and section views at -125 m-depth and 0 m-easting, respectively. A transmitter is located at (-200 m, 0 m, 30 m). Black arrows and shaded values indicate the direction and amplitude of the current, respectively. Black solid outlines boundary of the surface or the chargeable body.

34 Seogi Kang and Douglas W. Oldenburg

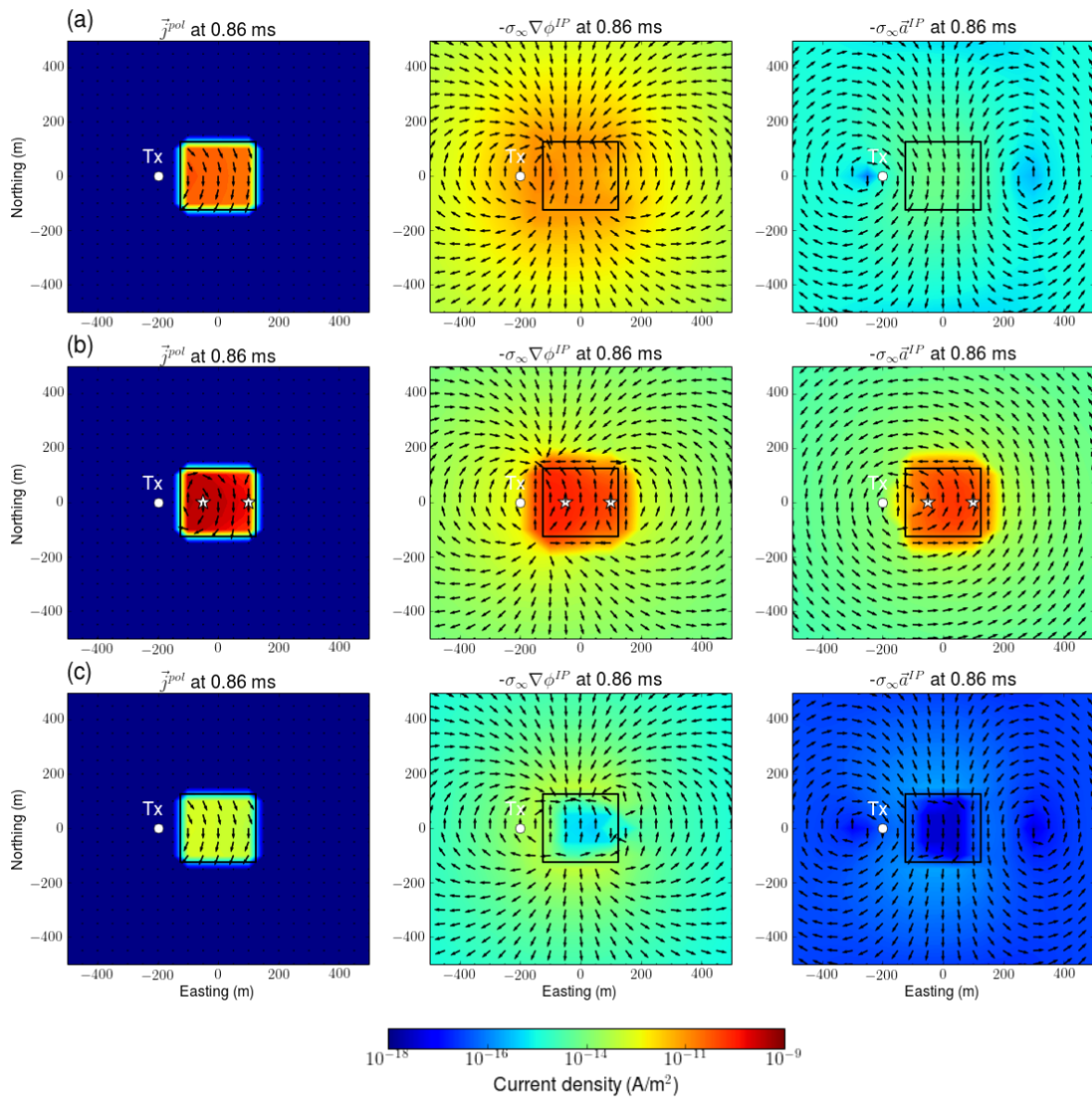


Figure 9. Decomposition of the IP currents as \vec{j}^{pol} (left panel), $-\sigma_\infty \nabla \phi^{IP}$ (middle panel), and $-\sigma_\infty \vec{a}^{IP}$ (right panel) at 0.86 ms. Plan view maps of the currents at -125 m-depth are shown: (a) canonical, (b) conductive, and (c) resistive cases.

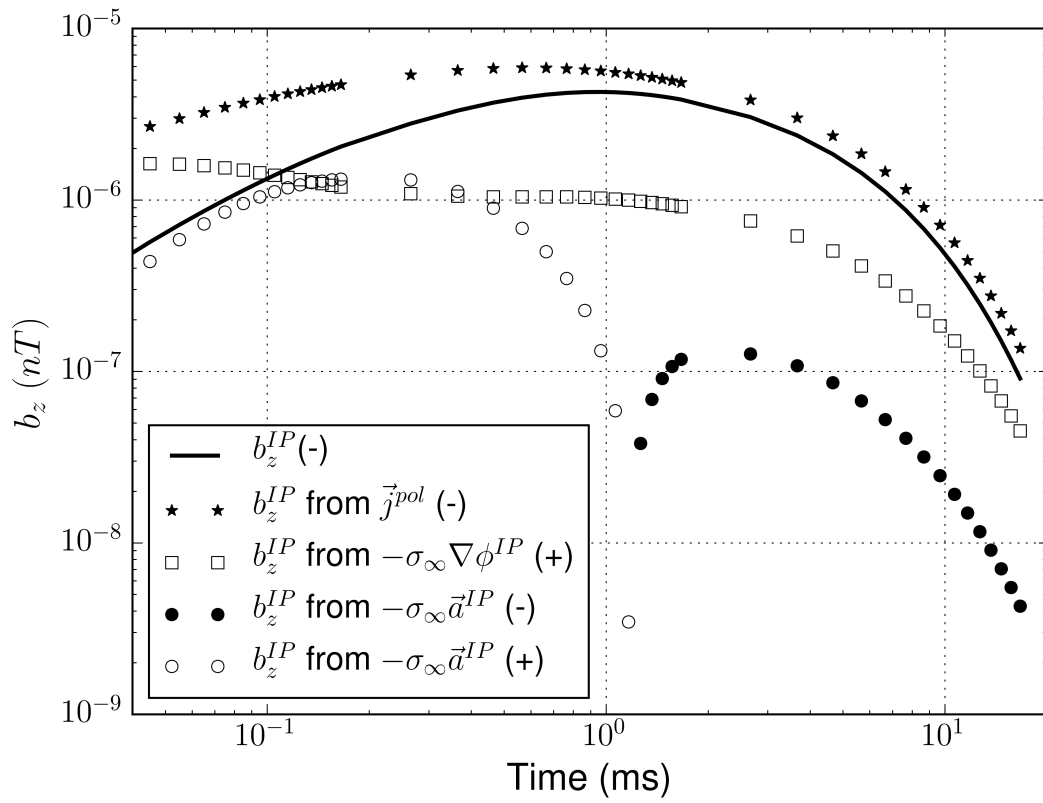


Figure 10. Comparisons of contributions of \vec{j}^{pol} , $-\sigma_\infty \vec{\nabla} \phi^{IP}$, and $-\sigma_\infty \vec{a}^{IP}$ to the observed IP responses. Solid line indicates true b_z^{IP} responses. Stars, rectangles, and circles correspondingly indicate each IP response generated by applying Biot-Savart law to \vec{j}^{pol} , $-\sigma_\infty \vec{\nabla} \phi^{IP}$, and $-\sigma_\infty \vec{a}^{IP}$. Empty and solid markers represent positive and negative values, respectively.

1
2
3
4 36 Seogi Kang and Douglas W. Oldenburg
5
6
7
8
9
10
11
12
13
14
15
16
17
18
19
20
21
22
23
24
25
26
27
28
29
30
31
32
33
34
35
36
37
38
39
40
41
42
43
44
45
46
47
48
49
50
51
52
53
54
55
56
57
58
59
60

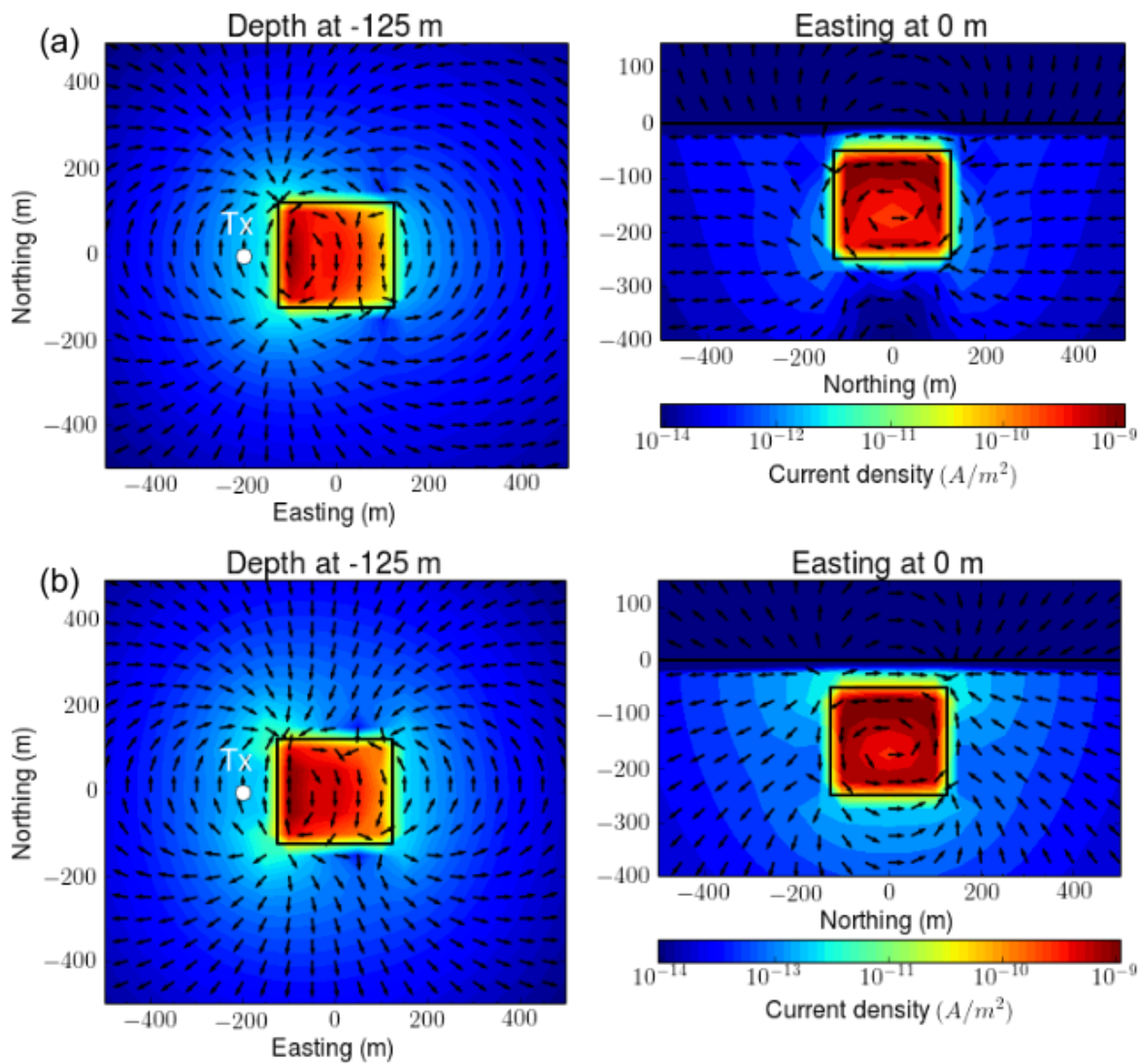


Figure 11. Interpolated maps of (a) true and (b) approximate IP currents at 0.86 ms. Left and right columns respectively show plan and section view maps at -125 m-depth and 0 m-easting.

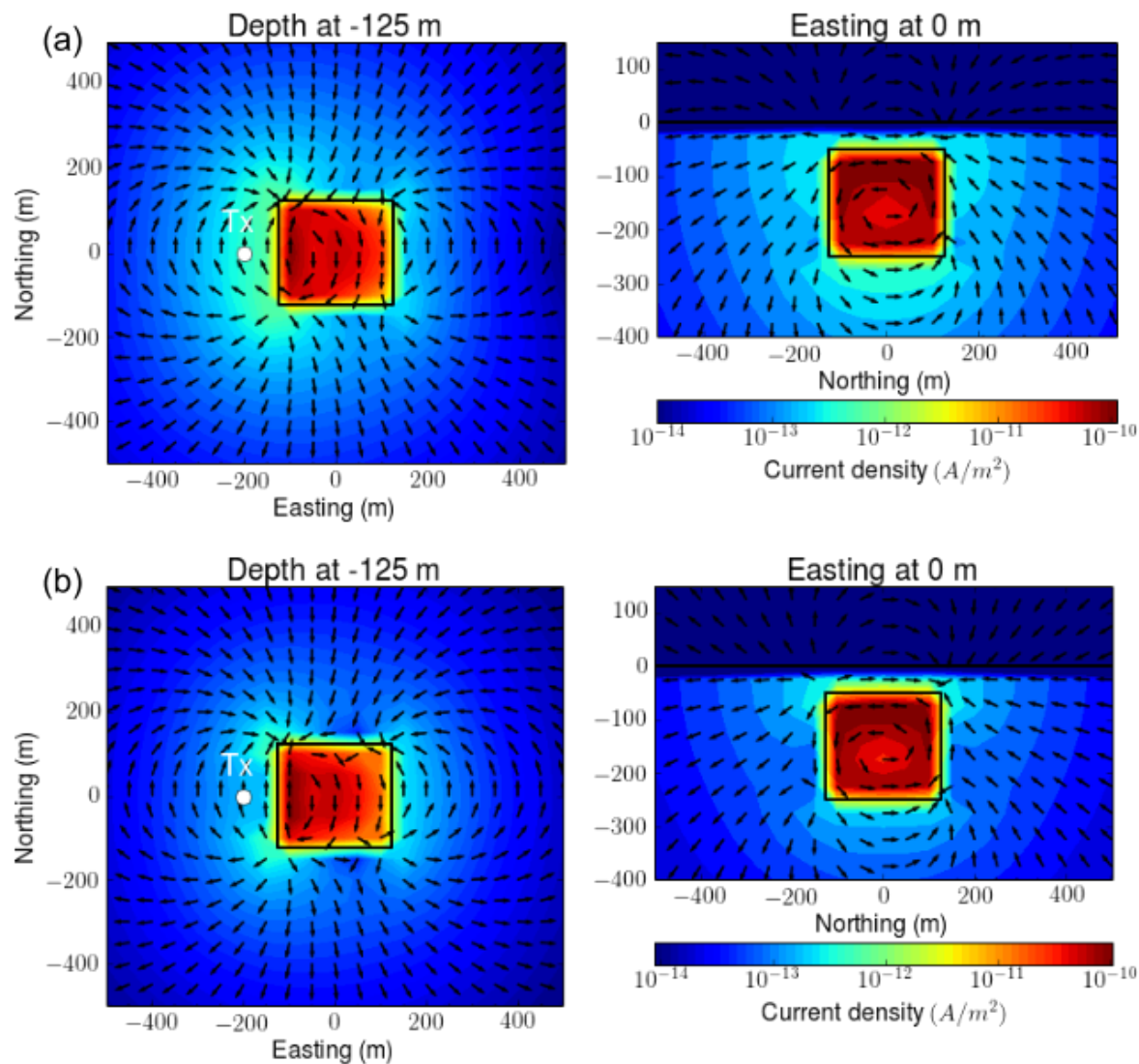
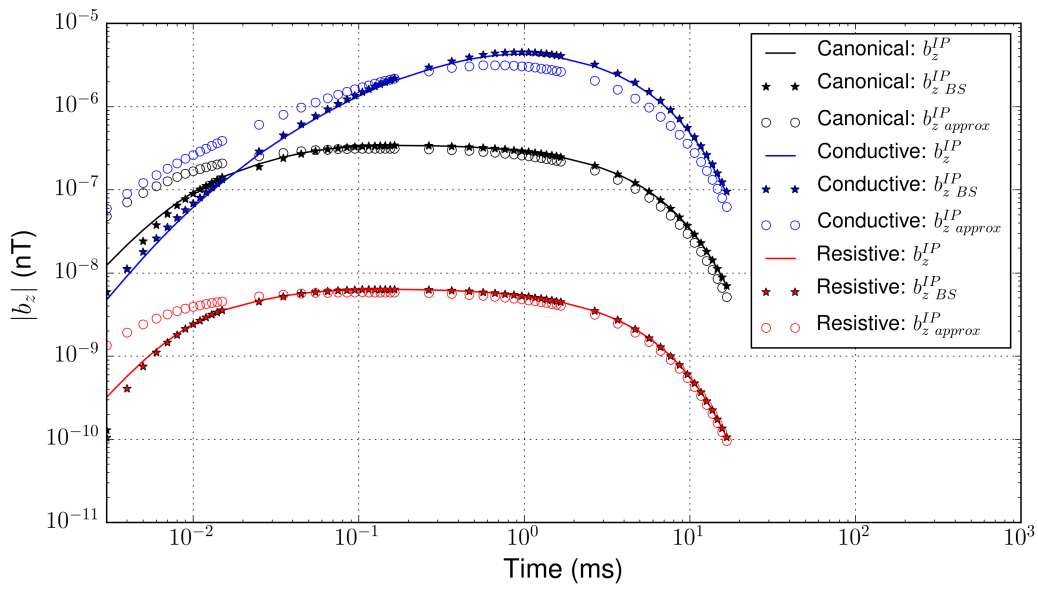


Figure 12. Interpolated maps of (a) true and (b) approximate IP currents at 6.7 ms. Left and right columns respectively show plan and section view maps at -125 m-depth and 0 m-easting.

1
2
3 38 Seogi Kang and Douglas W. Oldenburg
4
5
6



28 **Figure 13.** Comparison of true and approximate IP responses (b_z^{IP}). Black, blue, and red colors respectively
29 indicate canonical, conductive, and resistive cases. Solid lines indicate true b_z^{IP} computed by subtracting the
30 fundamental response from the observation. The stars are the application of Biot-Savart to true IP current and
31 generate $b_z^{IP}_{BS}$. Empty circles show our approximate $b_z^{IP}_{approx}$ response.
32
33
34
35
36
37
38
39
40
41
42
43
44
45
46
47
48
49
50
51
52
53
54
55
56
57
58
59
60

On recovering distributed IP information from inductive source time domain electromagnetic data 39

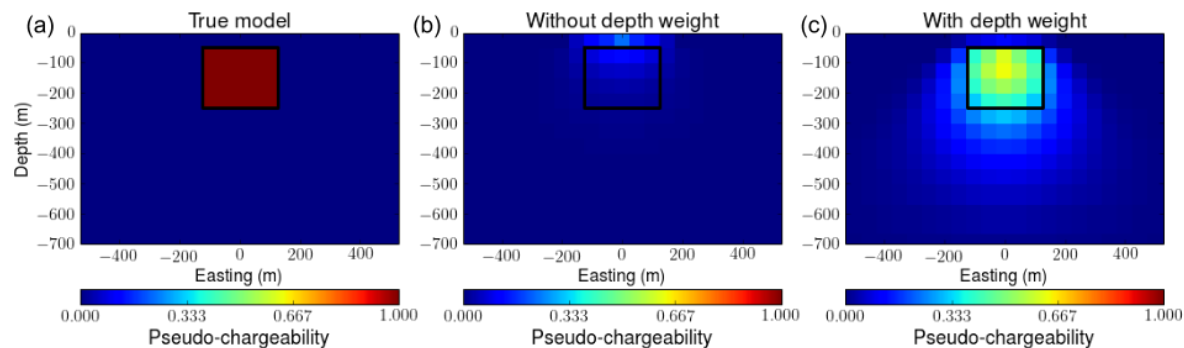


Figure 14. Effect of depth weighting in 3D IP inversion. (a) True pseudo-chargeability model on vertical section at 0 m-northing. Recovered pseudo-chargeability models (b) without depth weighting and (c) with depth weighting.

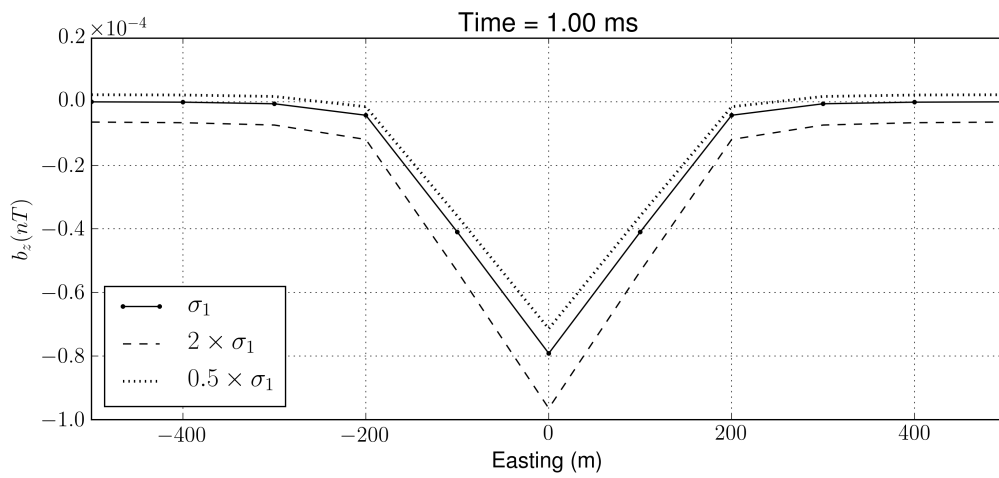


Figure 15. IP responses on a profile line at 0 m-northing. IP responses are computed from perturbed σ_∞ models. Halfspace conductivity (σ_1) is perturbed two times higher or less resulting in overestimated (dotted line) and underestimated (dashed line) IP responses. Solid line shows the true IP response.

40 Seogi Kang and Douglas W. Oldenburg

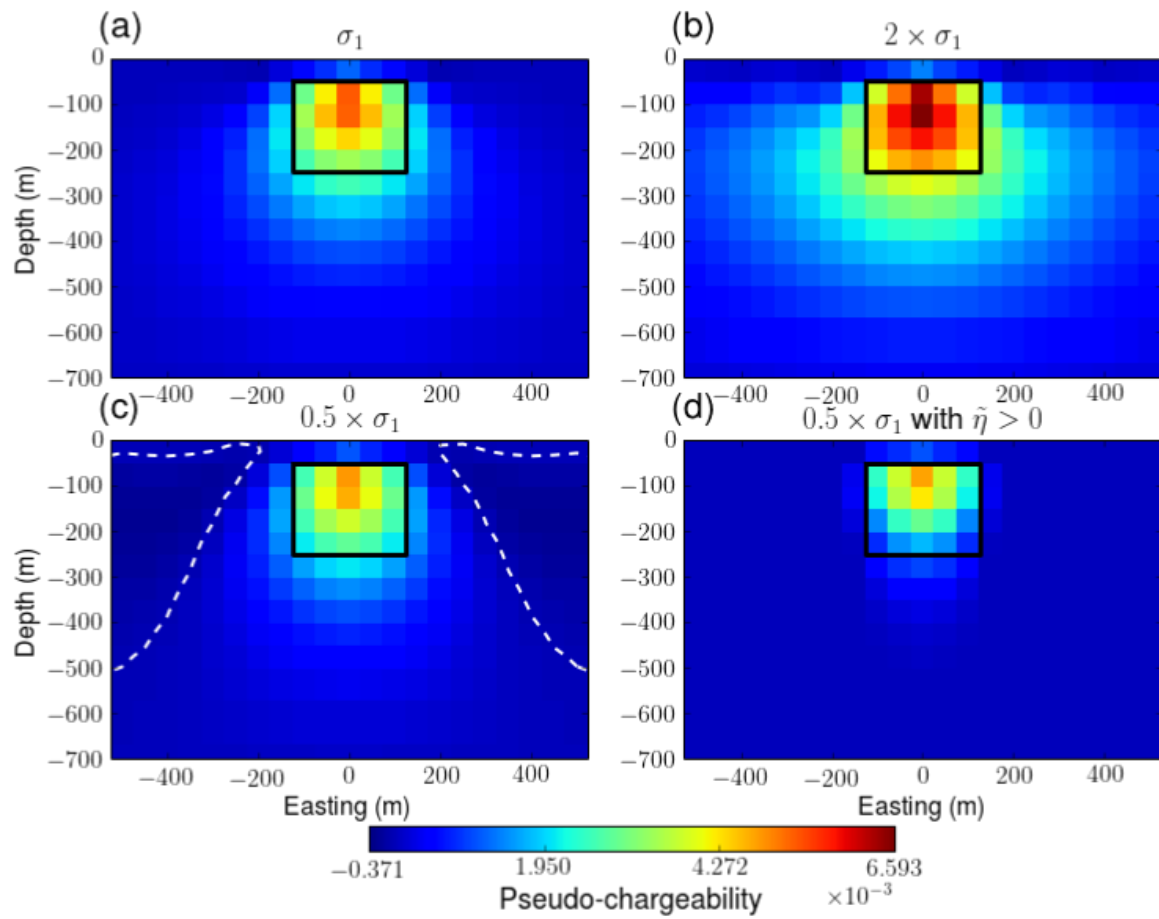


Figure 16. Recovered pseudo-chargeability sections from 3D IP inversions at 0 m-northing. (a) d^{IP} with true σ_1 . (b) d^{IP} with $2 \times \sigma_1$. (c) d^{IP} with $0.5 \times \sigma_1$. (d) d^{IP} with $0.5 \times \sigma_1$ and the positivity constraint on the pseudo-chargeability. White dashed lines contour zero-crossing lines.

1
2
3
4 *On recovering distributed IP information from inductive source time domain electromagnetic data* 41
5
6
7
8
9
10
11
12
13
14
15
16
17
18
19
20
21
22
23
24
25
26
27
28
29
30
31
32
33
34
35
36
37
38
39
40
41
42
43
44
45
46
47
48
49
50
51
52
53
54
55
56
57
58
59
60

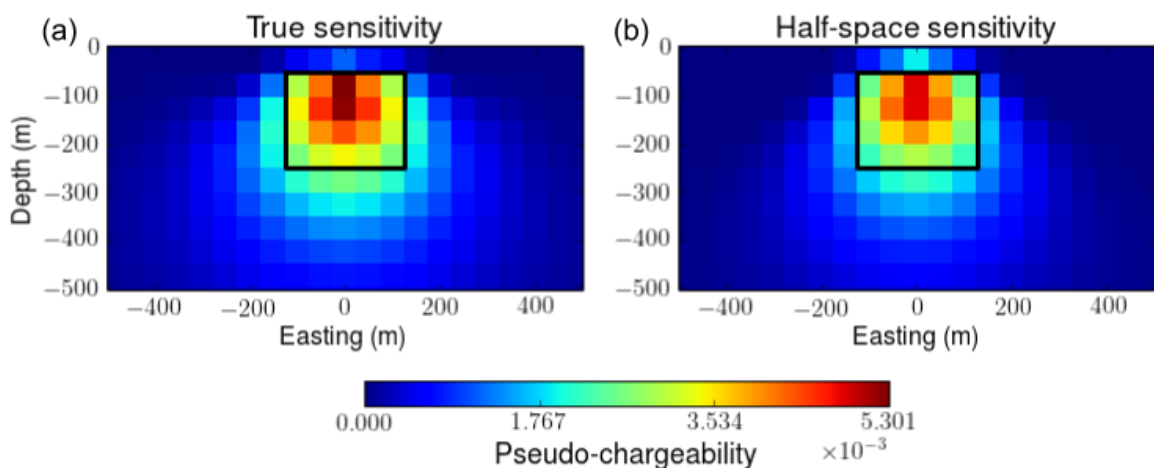


Figure 17. Recovered pseudo-chargeability sections from the 3D IP inversions at 0 m-northing. (a) True and (b) incorrect σ_∞ is used to compute sensitivity function. For the incorrect sensitivity we used a halfspace conductivity σ_1 .

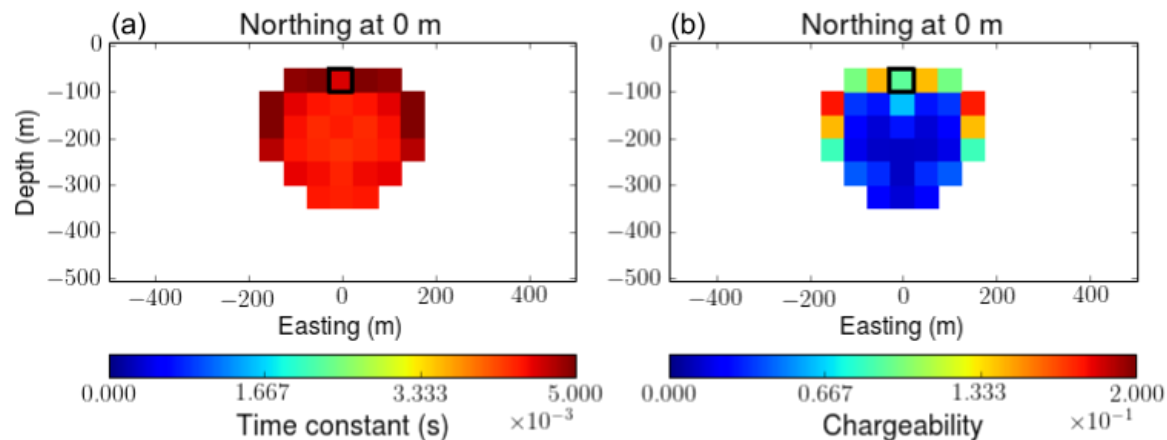


Figure 18. Section views of recovered: (a) time constant and (b) chargeability. Any region where the pseudo-chargeability shown in Fig. 17a is smaller than 0.001 is ignored in this analysis, and blanked.

42 Seogi Kang and Douglas W. Oldenburg

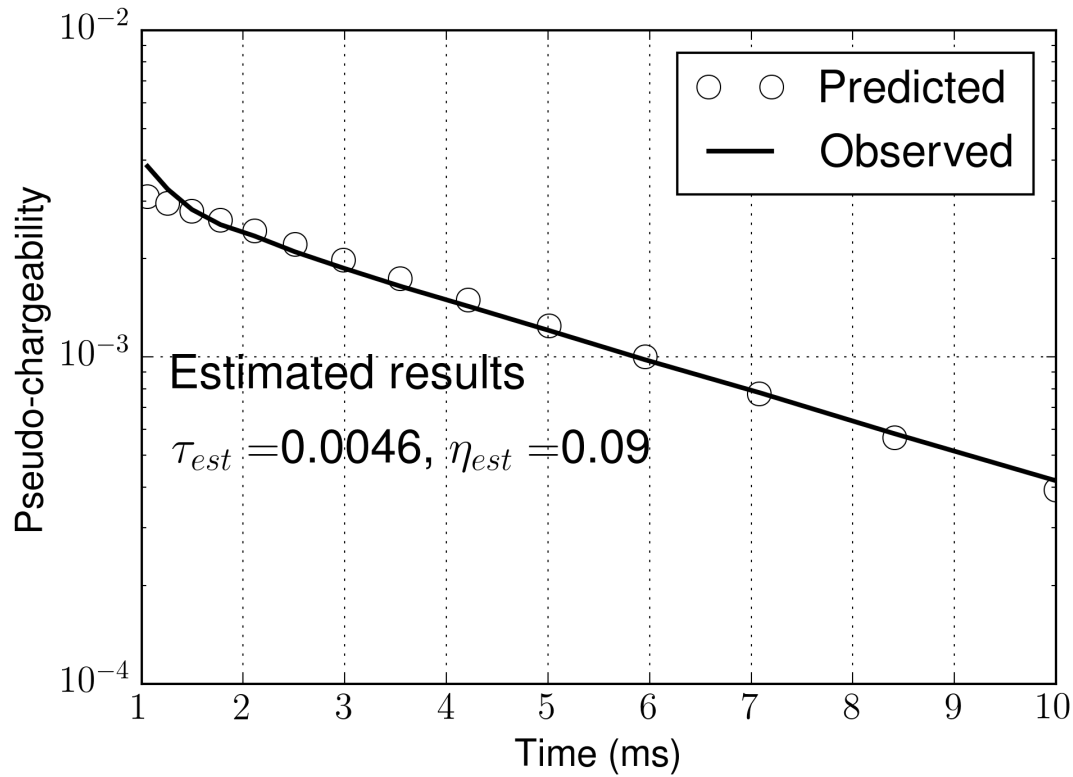


Figure 19. Comparisons of the observed and predicted pseudo-chargeability at a single pixel in a chargeable body. The empty circles and solid line respectively indicate predicted and observed pseudo-chargeability. The estimated time constant and chargeability are respectively expressed as τ_{est} and η_{est} . The true values for τ and η are respectively 0.005 and 0.2.

1
2
3 *On recovering distributed IP information from inductive source time domain electromagnetic data* 43
4
5

6 **APPENDIX A: EFFECTIVE PSEUDO-CHARGEABILITY**
7
8

9 **A1 Handling multiple transmitters in ATEM surveys**
10

11 The work for inductive sources in the main section of the paper has been developed for a single
12 transmitter and 3D information about chargeability can be obtained if there are multiple receivers. For
13 ATEM data however, we have only a single receiver location for each transmitter but we have multiple
14 transmitter locations. Our goal is to alter the problem to work with an effective pseudo-chargeability.
15
16

17 In our linearized eq. (39), each transmitter has its own sensitivity and pseudo-chargeability. For our
18 airborne case the sensitivity for the k -th transmitter is the k -th row of \mathbf{J} and the pseudo-chargeability
19 is $\tilde{\eta}^k$. The corresponding IP datum is
20

$$22 \quad d_k^{IP}(t) = \sum_{i=1}^{nC} J_{k,i} \tilde{\eta}_i^k(t), \quad k = 1, \dots, nTx, \quad (A.1)$$

23 where nTx is the number of transmitters, nC is the number of cells in the domain, and $J_{k,i}$ indicates
24 an element of the Jacobian matrix for the k -th transmitter and the i -th cell. We want to replace $\tilde{\eta}_i^k$ with
25 a single effective pseudo-chargeability $\tilde{\eta}_i$ and therefore write the IP datum as
26
27

$$28 \quad d_k^{IP}(t) = \sum_{i=1}^{nC} J_{k,i} \tilde{\eta}_i(t), \quad k = 1, \dots, nTx, \quad (A.2)$$

29 The waveforms are different for each transmitter and hence this representation cannot be exact. To
30 examine the implications of this it suffices to look at the contribution of any volumetric pixel. Each
31 pixel contributes to all of the IP data but in differing amounts. The total contribution of the i -th pixel
32 to the nTx data set at a single time is
33
34

$$35 \quad q_i = \sum_{k=1}^{nTx} J_{k,i} \tilde{\eta}_i^k(t), \quad i = 1, \dots, nC. \quad (A.3)$$

36 Our goal is to find an effective chargeability that produces the same net effect on the measured data.
37
38 We search for a transmitter-independent $\tilde{\eta}_i$ such that
39

$$40 \quad q_i^{est} = \sum_{k=1}^{nTx} J_{k,i} \tilde{\eta}_i(t), \quad i = 1, \dots, nC. \quad (A.4)$$

41 Minimizing the least squares difference between eqs (A.3) and (A.4) yields
42
43

$$44 \quad \tilde{\eta}_i(t) = \frac{\sum_{k=1}^{nTx} J_{k,i}^2 \tilde{\eta}_i^k(t)}{\sum_{k=1}^{nTx} J_{k,i}^2} = \sum_{k=1}^{nTx} a_i^k \tilde{\eta}_i^k(t), \quad i = 1, \dots, nC. \quad (A.5)$$

45 where the normalized weight (p_i^k) is
46
47

$$48 \quad p_i^k = \frac{J_{k,i}^2}{\sum_{k=1}^{nTx} J_{k,i}^2}, \quad i = 1, \dots, nC. \quad (A.6)$$

1
2
3 44 Seogi Kang and Douglas W. Oldenburg
4
5

6 With the above understanding about how $\tilde{\eta}_i$ relates to the $\tilde{\eta}_i^k$ from each transmitter we can proceed
7
8 as follows. Firstly, from eq. (28) we have
9
10

$$\tilde{\eta}_i^k(t) = \tilde{\eta}^I \otimes \hat{w}_i^k(t) \quad (\text{A.7})$$

11
12 3 Substituting eqs (A.7) into (A.5) allows us to write
13
14

$$\tilde{\eta}_i(t) = \tilde{\eta}^I(t) \otimes w_i^e(t), \quad (\text{A.8})$$

15
16 4 where we define the effective time history of the electric field, $w_i^e(t)$ as
17
18

$$w_i^e(t) = \sum_{k=1}^{nTx} a_i^k \hat{w}_i^k(t), \quad i = 1, \dots, nC. \quad (\text{A.9})$$

19
20 5 The above equations shows that the pseudo-chargeability for any pixel recovered from the inversion
21
22 is equal to the convolution of the impulse pseudo-chargeability, $\tilde{\eta}^I(t)$, with an effective time history
23
24 of the electric field $w^e(t)$. Although it is somewhat involved, the $w^e(t)$ associated with each pixel can
25
26 be evaluated by knowing the electric fields associated with the fundamental EM problem. Ultimately
27
28 this allows us to estimate the parameters associated with the impulse pseudo-chargeability in the same
29
30 manner as outlined for the case with a single transmitter. Our ability to evaluate the $w^e(t)$ and test the
31
32 validity of eq. (A.2) is treated in Section A2.
33
34

35 12 A2 Effective pseudo-chargeability for ATEM data

36
37 In Appendix A1 we showed how to define an effective chargeability when we have multi-transmitters.
38
39 For each pixel we have equation:

$$\tilde{\eta}_i(t) = \tilde{\eta}_i^I(t) \otimes w_i^e(t), \quad (\text{A.10})$$

40
41 13 where $\tilde{\eta}_i^I(t)$ is the impulse pseudo-chargeability associated with an individual pixel. The effective
42
43 time history of the electric field, $w_i^e(t)$ is a linear combination of the fundamental electric fields due
44
45 to the individual transmitters. We can calculate $w_i^e(t)$ and carry out the convolution to evaluate the
46
47 effective pseudo-chargeability. The IP data can then be forward modelled using eq. (39). This allows
48
49 us to validate eq. (A.2), which demonstrated linear form of d^{IP} data at all transmitter locations, by
50
51 comparing results with the true IP data obtained via forward modelling. It is only necessary to apply
52
53 this to the conductive model.

54
55 20 The evaluation of the effective pseudo-chargeability is carried out on a cell by cell basis. For each
56
57 cell we first evaluate $w^e(t)$ (eq. A.9). This requires calculating normalized weights shown in eq. (A.6).
58
59 Fig. A1 shows these weights at a single pixel located at (0 m, 0 m, -75 m). These decay away from
60
61 the center pixel because of the decay of the sensitivity functions. Because those are weights used
62
63 to compute $w^e(t)$, we could expect that the computed $w^e(t)$ will be mostly affected by \hat{w}_k from a

On recovering distributed IP information from inductive source time domain electromagnetic data 45

few stations close to the center. In Fig. A2, we provide both \hat{w}_k (dashed lines) from all transmitter locations and $w^e(t)$ (solid line) averaged by them. The $w^e(t)$ is dominantly affected by the $\hat{w}(t)$ at the center transmitter location (solid circles). Considering that the transmitters are 50 m apart, the decay of the sensitivity from center transmitter location to others is substantial ($\sim 1/r^3$). This results in the greatest normalized weight at the center transmitter location, and the observed result about $w^e(t)$ is caused by this. $w^e(t)$ is convolved with $\tilde{\eta}^I(t)$ to compute the effective $\tilde{\eta}(t)$ for that cell. When this is carried out for each cell then the approximate IP responses can be computed using eq. (39). These can be compared with the true IP responses. Fig. A3 shows the comparisons at 0.86 ms. The images are nearly identical in shape but the approximate IP responses are nearly a factor of two lower than the true values. This is not entirely unexpected. A similar effect was observed for IP responses for a single transmitter shown in Fig. 13. At 0.86 ms, the approximate value was about 70 percent of the true d^{IP} . These results seem to be a worst case scenario. The discrepancy for a conductive body lessens as time increases and analyses for the canonical and resistive bodies shows that the approximate and true IP data are in very good agreement.

APPENDIX B: EXTRACTING INTRINSIC IP PARAMETERS

The output of our IP inversion is a 3D distribution of the pseudo-chargeability at multiple time channels. As its name suggests, pseudo-chargeability is not an intrinsic IP parameter like chargeability, but it is a convoluted property between $\tilde{\eta}^I(t)$ and $\hat{w}(t)$:

$$\tilde{\eta}(t) = \tilde{\eta}^I(t) \otimes \hat{w}(t), \quad (B.1)$$

with the definition of impulse pseudo-chargeability (eq. 4). We now use the $\tilde{\eta}(t)$ as the data and recover intrinsic parameters such as η, τ, c in a Cole-Cole model. Assuming a Debye model ($c=1$), we obtain

$$\tilde{\eta}^I(t) = \frac{\eta}{(1-\eta)\tau} e^{-\frac{t}{(1-\eta)\tau}}, \quad (B.2)$$

Since we have σ_∞ we can compute $\hat{w}(t)$, which is the time history of the electric field. Accordingly, we can unravel the recovered pseudo-chargeability to extract intrinsic IP parameters such as chargeability(η) and time constant (τ). We use a gradient-based optimization and thus we need the sensitivity function for the pseudo-chargeability (eq. B.1) with respect to η and τ . To simplify this procedure, we rewrite impulse pseudo-chargeability as

$$\tilde{\eta}^I(t) = a e^{-bt}, \quad (B.3)$$

where $a = \frac{\eta}{(1-\eta)\tau}$ and $b = \frac{1}{(1-\eta)\tau}$. Then we take the derivative of $\tilde{\eta}(t)$ with regard to a and b :

$$\frac{\partial \tilde{\eta}(t)}{\partial a} = e^{-bt} \otimes \hat{w}(t), \quad (B.4)$$

1
2
3 46 Seogi Kang and Douglas W. Oldenburg
4
5

6
$$\frac{\partial \tilde{\eta}(t)}{\partial b} = -ate^{-bt} \otimes \hat{w}(t). \quad (\text{B.5})$$

7
8

9 1 With these sensitivity functions, we can set up an inverse problem, and recover a and b . The charge-
10 2 ability and time constant can be obtained from a and b :
11
12

13
$$\eta = \frac{a}{b}, \quad (\text{B.6})$$

14
15

16
$$\tau = \frac{1}{(1 - a/b)b}. \quad (\text{B.7})$$

17
18

19 4 We apply this inversion separately to each cell in the recovered pseudo-chargeability in a manner
20 5 similar to (Yuval & Oldenburg 1997). For the better alternative (representation) of time-dependent
21 6 conductivity, a different parameterization such as stretched-exponential (Kohlrausch 1854) or Cole-
22 7 Cole model with variable c can be implemented.
23
24
25
26
27
28

29 APPENDIX C: DISCRETIZATIONS 30

31 9 C1 Steady-state Maxwell's equations 32

33 As shown in eq. (33), computation of our linearized kernel requires solving steady-state Maxwell's
34 equations. We discretize this system using a mimetic finite volume (FV) method with weak formulation
35 (Yee 1966; Haber 2014). For the discretization, we assume that the electric field \vec{e} is discretized
36 by a grid function e on cell edges and the magnetic flux density \vec{b} is discretized by a grid function b on
37 cell faces. The electrical potential ϕ is discretized by a grid function ϕ on the cell nodes. For a clear
38 representation of the derivation, recall Maxwell's equations in steady state are
39
40

41
$$\vec{j} = \sigma_\infty \vec{e} = -\sigma_\infty \vec{\nabla} \phi, \quad (\text{C.1})$$

42
43

44
$$-\nabla \cdot \vec{j} = \nabla \cdot \vec{j}_s, \quad (\text{C.2})$$

45
46

47
$$\vec{j}|_{\partial\Omega} \cdot \hat{n} = 0, \quad (\text{C.3})$$

48
49

50 where $\partial\Omega$ indicates boundary surface of the system and \hat{n} is the normal vector of the boundary surface.
51

52 The weak form of those equations can be written as
53
54

55
$$(\vec{j}, \vec{w}) + (\sigma_\infty \vec{\nabla} \phi, \vec{w}) = 0, \quad (\text{C.4})$$

56
57

58
$$-(\vec{j}, \vec{\nabla} \psi) = (\vec{j}_s, \vec{\nabla} \psi). \quad (\text{C.5})$$

59
60

61 10 The inner products (\vec{j}, \vec{w}) , $(\sigma_\infty \vec{\nabla} \phi, \vec{w})$, $(\vec{j}, \vec{\nabla} \psi)$ and $(\vec{j}_s, \vec{\nabla} \psi)$ are edge-based products. Here we define
62 11 the inner product as

63
$$(\vec{a}, \vec{b}) = \int_{\Omega} \vec{a} \cdot \vec{b} dv, \quad (\text{C.6})$$

64
65

On recovering distributed IP information from inductive source time domain electromagnetic data 47

where Ω is the volume of the system. By discretizing the $\vec{\nabla}$ operator and the inner product in space, we obtain

$$\mathbf{M}^e \mathbf{j} + \mathbf{M}_{\sigma_\infty}^e \mathbf{G} \phi = 0, \quad (C.7)$$

$$-\mathbf{G}^T \mathbf{M}^e \mathbf{j} = \mathbf{G}^T \mathbf{M}^e \mathbf{j}_s, \quad (\text{C.8})$$

4 where \mathbf{M}^e performs volume averaging, and $\mathbf{M}_{\sigma_\infty}^e$ is the mass matrix of conductivity (σ_∞), which
 5 discretizes the edge based inner product. For further details on the formation of this matrix see Haber
 6 (2014).

7 By substituting eq. (C.7) into (C.8), we have

$$\mathbf{A}_{\sigma_\infty} \phi = \mathbf{rhs}^{DC}, \quad (C.9)$$

8 where $\mathbf{A}_{\sigma_\infty} = \mathbf{G}^T \mathbf{M}_{\sigma_\infty}^e \mathbf{G}$ and $\mathbf{rhs}^{DC} = \mathbf{G}^T \mathbf{M}^e \mathbf{j}_s$. We use SIMPEG's tensor mesh and solver
9 classes to form and solve above linear system (Cockett et al. 2015).

10 C2 Linearized kernel for IP responses

To obtain a linear form of eq. (39), we first discretize the Biot-Savart law shown in eqs (37) and (38). In our discretization \vec{j}^{IP} and $\tilde{\eta}$ are defined at the cell centers, and those for each time channel are constant in a cell volume, whereas \vec{e}^{ref} is defined on the cell edges. We define the number of cells and edges in 3D space as nC and nE , respectively. The discretized IP current density, $\mathbf{j}_{cc}^{IP} \in \mathbb{R}_1^{3nC}$, is defined at the cell center. Since \vec{j}^{IP} has three components, we first discretize the integration operator including cross product ($\int_v \frac{\mathbf{x}\hat{r}}{r^2} dv$) as

$$\mathbf{G}_{Biot} = \begin{bmatrix} \mathbf{e}^T & \mathbf{0} & \mathbf{0} \\ \mathbf{0} & \mathbf{e}^T & \mathbf{0} \\ \mathbf{0} & \mathbf{0} & \mathbf{e}^T \end{bmatrix} \begin{bmatrix} \mathbf{0} & \mathbf{S}_z & -\mathbf{S}_y \\ -\mathbf{S}_z & \mathbf{0} & \mathbf{S}_x \\ \mathbf{S}_y & -\mathbf{S}_x & \mathbf{0} \end{bmatrix}, \quad (C.10)$$

17 where

$$\mathbf{S}_l = \mathbf{diag}(\mathbf{v} \oplus \mathbf{r}_l \oplus \frac{1}{\mathbf{r}^2}), \quad l = x, y, z$$

and the electric field, $\mathbf{e} \in \mathbb{R}_1^{nE}$ is a column vector, $\text{diag}(\cdot)$ is the diagonal matrix and \oplus is the Hadamard product. Then we discretize \vec{j}^{IP} shown in eq. (35) as

$$\mathbf{j}_{cc}^{IP}(t) \equiv \mathbf{S} \text{diag}(\mathbf{e}_{max}^F) \mathbf{A}_c^{eT} \text{diag}(\mathbf{v}) \text{diag}(\sigma_\infty) \tilde{\eta}(t), \quad (\text{C.11})$$

where \mathbf{A}^e is a discrete averaging matrix from edge to cell center and

$$S = A^e - M^{e-1} [M^e - G A^{-1} G^T - I] \text{diag}(e^F -) A^{eT} \text{diag}(v) \text{diag}(\sigma_{\text{res}}) \quad (C12)$$

1
2
3 48 *Seogi Kang and Douglas W. Oldenburg*
4
5

6 1 Here \mathbf{A}_{ccv}^e is a discrete averaging matrix from edge to cell center with consideration of three compo-
7 2 nent vector: $\in \mathbb{R}_{nE}^{3nC}$. Thus, we can have a linear equation for a single time channel as
8
9

$$\mathbf{b}^{IP} = \mathbf{G}_{Biot} \mathbf{S} \tilde{\eta},$$

10 12 Finally, by letting
13
14 3 $\mathbf{J} = \mathbf{G}_{Biot} \mathbf{S}$, (C.13)
15
16 4 we have
17
18 5 where \mathbf{J} is the Jacobian matrix of the linear equation, and since \mathbf{J} is static, we also obtain
19
20 22
21 23
22 24
23 25
24 26
25 27
26 28
27 29
28 30
29 31
30 32
31 33
32 34
33 35
34 36
35 37
36 38
37 39
38 40
39 41
40 42
41 43
42 44
43 45
44 46
45 47
46 48
47 49
48 50
49 51
50 52
51 53
52 54
53 55
54 56
55 57
56 58
57 59
58 60

$$\mathbf{b}^{IP} = \mathbf{J} \tilde{\eta}, \quad (C.14)$$

$$-\frac{\partial \mathbf{b}^{IP}}{\partial t} \Big| = \mathbf{J} \left(-\frac{\partial \tilde{\eta}}{\partial t} \Big| \right). \quad (C.15)$$

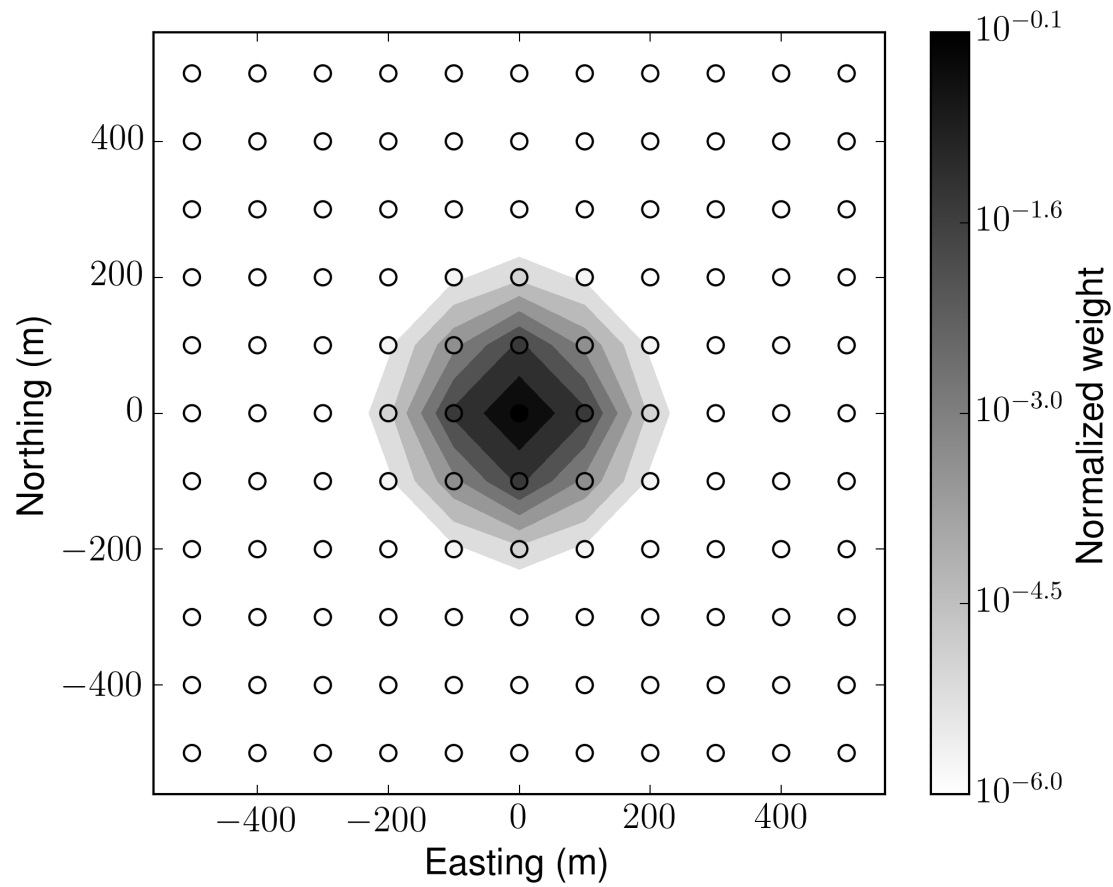


Figure A1. Normalized weights for the conductive case for all transmitter locations. A single pixel located at (0 m, 0 m, -75 m) is used.

50 Seogi Kang and Douglas W. Oldenburg

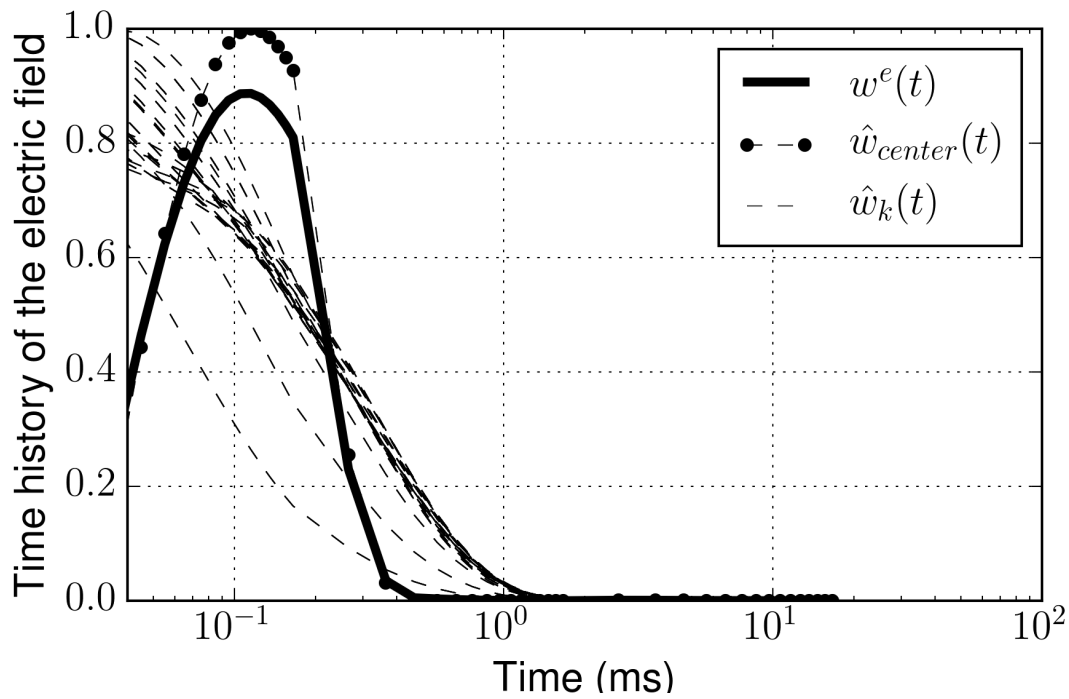


Figure A2. Time decays of $w^e(t)$ and $\hat{w}(t)$ for the conductive case. A single pixel located at (0 m, 0 m, -75 m) is used. Solid line and dashed lines correspond to $w^e(t)$ and $\hat{w}_k(t)$ for all transmitters ($k = 1, \dots, n_{Tx}$); \hat{w}_k at the center transmitter located at (0 m, 0 m, 30 m) is marked as solid circles. A number of $w^e(t)$ curves are overlaid due to the symmetric position of transmitter locations to the conductive block.

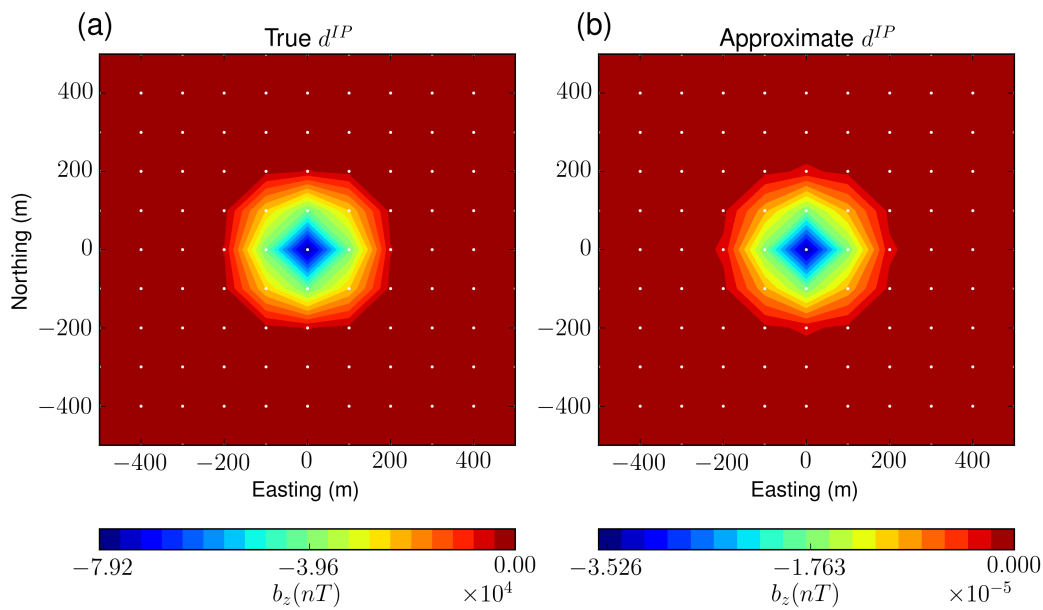


Figure A3. Comparison of true and approximate b_z^{IP} responses at 0.86 ms on plan view map.

1
2
3 submitted to *Geophys. J. Int.*
4
5
6
7
8

9 On recovering distributed IP information from inductive 10 source time domain electromagnetic data 11 12

13
14
15
16 Seogi Kang and Douglas W. Oldenburg
17
18

19 *Department of Earth, Ocean and Atmospheric Sciences, University of British Columbia, B.C. V6T 1Z4, Canada*
20
21
22
23
24
25

26 SUMMARY 27

28 We develop a procedure to invert time domain induced polarization (IP) data for inductive
29 sources. Our approach is based upon the inversion methodology in conventional electrical
30 IP (EIP), which uses a sensitivity function that is independent of time. However, signif-
31 icant modifications are required for inductive source IP (ISIP) because electric fields in
32 the ground do not achieve a steady state. The time-history for these fields needs to be
33 evaluated and then used to define approximate IP currents. The resultant data, either a
34 magnetic field or its derivative, are evaluated through the Biot-Savart law. This forms the
35 desired linear relationship between data and pseudo-chargeability. Our inversion pro-
36 cedure has three steps: 1) Invert TEM data and recover a 3D distribution of conductivity.
37 2) Decouple IP responses embedded in the observations by forward modelling the TEM
38 data due to a background conductivity and subtracting these from the observations. 3)
39 Use the linearized sensitivity function to invert data at each time channel and recover
40 pseudo-chargeability. Post-interpretation of the recovered pseudo-chargeabilities at mul-
41 tiple times allows recovery of intrinsic Cole-Cole parameters such as time constant and
42 chargeability. The procedure is applicable to all inductive source survey geometries but
43 we focus upon airborne time domain EM (ATEM) data with a coincident-loop configura-
44 tion because of the distinctive negative IP signal that is observed over a chargeable body.
45 Several assumptions are adopted to generate our linearized modelling but we systemati-
46
47
48
49
50
51
52
53
54
55
56
57
58
59
60

1
2
3 2 *Seogi Kang and Douglas W. Oldenburg*
4
5
6
7
8
9
10
11
12
13
14
15
16
17
18
19
20
21
22
23
24
25
26
27
28
29
30
31
32
33
34
35
36
37
38
39
40
41
42
43
44
45
46
47
48
49
50
51
52
53
54
55
56
57
58
59
60

2 cally test the capability and accuracy of the linearization for ISIP responses arising from
3 different conductivity structures. On test examples we show: (a) our decoupling procedure
4 enhances the ability to extract information about existence and location of chargeable tar-
5 gets directly from the data maps; (b) the horizontal location of a target body can be well
6 recovered through inversion; (c) the overall geometry of a target body might be recovered
7 but for ATEM data a depth weighting is required in the inversion; (d) we can recover es-
8 timates of intrinsic τ and η that may be useful for distinguishing between two chargeable
9 targets.

1 1 INTRODUCTION

2 The electrical conductivity of earth materials can be frequency dependent with the effective conduc-
3 tivity decreasing with decreasing frequency due to the buildup of electric charges that occur under the
4 application of an electric field. Effectively, the rock is electrically polarized. Applications of induced
5 polarization (IP) surveys to find chargeable material have been particularly successful in mineral ex-
6 ploration for disseminated sulphide or porphyry deposits (Pelton et al. 1978; Fink et al. 1990) and also
7 in geotechnical and environmental problems (Li & Oldenburg 2000; Kemna et al. 2012).

8 Polarization charges can accumulate whenever there is an electric field in a medium. In controlled
9 source surveys, the transmitter can be a galvanic source (a generator attached to two grounded elec-
10 trodes), or an inductive source (arising from currents flowing in a wire loop). Most research and appli-
11 cation has focused upon using grounded electrodes and measuring electric fields; this is called an EIP
12 survey (Seigel 1959). Magnetic fields arising from polarization currents using grounded electrodes
13 as the transmitter (MIP survey) have also been successfully used, particularly in mineral exploration
14 when there is a conductive overburden (Seigel 1974). In recent years attention has also turned towards
15 the use of inductive sources. Inductive source IP (ISIP), can have transmitters in the air or on the
16 ground and the waveforms can be in the frequency or time domain. Recently (Marchant et al. 2012)
17 showed how, by collecting data at two frequencies, it was possible to measure data that depended
18 purely on IP signals and that these data can be inverted to recover a 3D distribution of chargeability.
19 For time domain systems the observations of negative transients in coincident-loop systems provide
20 an distinctive verification of the existence of chargeable material (Weidelt 1982). These negative tran-
21 sients have been frequently observed (Smith & Klein 1996; Kang & Oldenburg 2015). The effects of
22 chargeable objects using time domain systems with inductive sources have been investigated (Smith
23 et al. 1988; Flis et al. 1989; ElKaliouby & Eldiwany 2004; Marchant et al. 2014) and approximate

1
2
3 *On recovering distributed IP information from inductive source time domain electromagnetic data* 3
45 interpretation tools (Kratzer & Macnae 2012; Hodges & Chen 2014) are being developed. The ability
6 to fully invert these data in 3D is still lacking.
78 Extracting information about the complex conductivity from observed data can be done in a variety
9 of ways. An inverse problem can be set up to find a function $\sigma(x, y, z, \omega)$ or a parameterization of the
10 complex conductivity, usually with a Cole-Cole type model, (Fiandaca et al. 2012; Marchant et al.
11 2013; Xu & Zhdanov 2015). Traditionally, however, with EIP and time domain waveforms, one first
12 estimates the background conductivity from the asymptotic on-time data and then inverts off-time data
13 to recover information about “chargeability” (Oldenburg & Li 1994). This is carried out by solving an
14 inverse problem using a linear function where the sensitivities depend upon geometry of the survey
15 and the background conductivity. The recovered values are really pseudo-chargeability, and they have
16 the same units as the data (eg. msec, mV/V). The same procedure can be used in the frequency domain
17 experiments but the data might have units of mrad and pfe (percent frequency effect). Inversions of IP
18 data to recover 2D or 3D distributions of pseudo-chargeability are now commonly carried out (Kemna
19 et al. 2012). These inversions delineate locations of high pseudo-chargeability and the geometry of the
20 bodies. MIP data can be inverted with the same methodology (Chen & Oldenburg 2003). We note that
21 pseudo-chargeability is different from intrinsic chargeability, η , where $\eta = \frac{\sigma_\infty - \sigma_0}{\sigma_\infty}$ and σ_∞ and σ_0 are
22 respectively the conductivity at the infinite frequency and the zero frequency.
2324 The physical mechanisms by which polarization charges and currents are established in the ground
25 are independent of the type of transmitter and waveform; the important quantity is the time history of
26 the electric field within the earth. The challenge posed by the use of inductive sources is that steady
27 state electric fields are not established inside the earth as they are for EIP or MIP surveys. At any
28 location in the earth the electric field will increase to a maximum value and then decrease as the
29 electromagnetic (EM) wave diffuses through. The EM fields at any position and time depend upon the
30 convolution of the electric field with the time-dependent conductivity of the rock. Unravelling these
31 complexities, and providing a framework for extracting information about IP characteristics of rocks,
32 are issues we address in our paper.
3334 Our procedure involves three principal steps: 1) estimating the 3D background conductivity and
35 carrying out an EM-decoupling to produce IP data (d^{IP}), and 2) developing a linearized formulation
36 using the Biot-Savart law and an effective pseudo-chargeability that encapsulates time dependencies
37 of the EM fields at any location in the earth, 3) inverting d^{IP} using the linear functional to recover
38 pseudo-chargeability at each time channel, and subsequently processing these multi-channel data to
39 obtain information about Cole-Cole parameters for each point in the subsurface. Each of these steps
40 requires special attention for inductive source data and approximations are required. Our paper pro-
41 ceeds as follows. We first outline our decomposition process for obtaining d^{IP} data, define a pseudo-
42

4 Seogi Kang and Douglas W. Oldenburg

1 chargeability, and show how our problem can be linearized. The data and pseudo-chargeability are
 2 linearly related through the Biot-Savart law and hence a depth weighting, required for other potential
 3 field inversions, is necessary to obtain geologically meaningful solutions. The inversion can be carried
 4 out at multiple times and a pseudo-chargeability as a function of time can be generated. These results
 5 can be used to recover intrinsic decays of the chargeable rock units and thus potentially differentiate
 6 between rock types in the same manner as carried out by Yuval & Oldenburg (1997) using EIP data. In
 7 our numerical experiments, we investigate the above steps and procedures, test our assumptions, and
 8 evaluate the circumstances under which our technique might provide meaningful results. Although we
 9 focus upon airborne TEM data, the analysis we present here is valid for surveys on the earth's surface
 10 using inductive sources and also for grounded sources although many of the complications we deal
 11 with are not relevant.

2 COMPLEX CONDUCTIVITY

13 A complex conductivity model presents a mathematical form of the IP phenomenon, and there are a
 14 number of models used in the literature (Dias 2000; Tarasov & Titov 2013). Each model has some
 15 reflection of an IP phenomenon, and each of these models is an attempt to capture the complicated
 16 nature of complex conductivity with a few parameters that may, or may not, have a physical meaning.
 17 For our research we needed to choose one. We follow Smith et al. (1988) and Marchant et al. (2014)
 18 who used a Cole-Cole model (Cole & Cole 1941) modified by Pelton et al. (1978):

$$\sigma(s) = \sigma_\infty - \sigma_\infty \left(\frac{\eta}{1 + (1 - \eta)(s\tau)^c} \right) = \sigma_\infty + \Delta\sigma(s), \quad (1)$$

19 where s is the Laplace transform variable, σ_∞ is the conductivity at infinite frequency, η is the intrinsic
 20 chargeability, τ is the time constant and c is the frequency dependency.

21 Real and imaginary parts of complex conductivity in the frequency domain are shown in Fig. 1(a)
 22 for Cole-Cole parameters: $\sigma_\infty = 10^{-2}$ S/m, $\eta = 0.5$, $\tau = 0.01$ s, and $c=1$. By applying the inverse
 23 Laplace transform, we have

$$\sigma(t) = \mathcal{L}^{-1}[\sigma(s)] = \sigma_\infty \delta(t) + \Delta\sigma(t), \quad (2)$$

24 where $\delta(t)$ is Dirac delta function, and $\mathcal{L}^{-1}[\cdot]$ is inverse Laplace transform operator. Note that we
 25 only deal with a causal function, which is defined when $t \geq 0$.

26 The intrinsic chargeability η is

$$\eta = -\frac{1}{\sigma_\infty} \lim_{t \rightarrow \infty} \mathcal{L}^{-1}\left[\frac{\Delta\sigma(s)}{s}\right] \quad (3)$$

1
2
3 *On recovering distributed IP information from inductive source time domain electromagnetic data* 5
4

5 1 Accordingly, it is convenient to define an impulse pseudo-chargeability, $\tilde{\eta}^I(t)$ as
6
7

$$8 \quad \tilde{\eta}^I(t) = -\frac{\Delta\sigma(t)}{\sigma_\infty}. \quad (4)$$

9

10 2 Effectively this writes $\Delta\sigma(t)$ as
11
12

$$13 \quad \Delta\sigma(t) = -\sigma_\infty \tilde{\eta}^I(t), \quad (5)$$

14 3 Note that the intrinsic chargeability, η , is not time-dependent but the impulse pseudo-chargeability,
15 4 $\tilde{\eta}^I(t)$, which is related to IP parameters: η , τ , and c , is time-dependent. The Cole-Cole response in
16 5 time domain is shown in Fig. 1(b). The arrow at $t=0$ s indicates $\sigma_\infty \delta(t)$, which is a delta function,
17 6 and after $t=0$ s, $\sigma(t) = \Delta\sigma(t)$. Since Ohm's law in time states that $\vec{j} = \sigma \otimes \vec{e}$ where \otimes indicates
18 7 convolution, the negative sign of $\Delta\sigma(t)$ shows that the polarization current in the chargeable body
19 8 will have a reversed direction compared to the primary current when an electric field is applied. We
20 9 will revisit this later in Section 4.
21
22
23
24
25
26
27

28 10 **3 DECOMPOSITION OF OBSERVED RESPONSES**
29

30 11 IP effects in the observed data are coupled with EM effects. We need to decompose the observations
31 12 to isolate data associated only with the IP phenomena. Maxwell's equations in the time domain, with
32 13 a quasi-static approximation, are written as:
33
34

$$35 \quad \vec{\nabla} \times \vec{e} = -\frac{\partial \vec{b}}{\partial t}, \quad (6)$$

36
37

$$38 \quad \vec{\nabla} \times \frac{1}{\mu} \vec{b} - \vec{j} = \vec{j}_s, \quad (7)$$

39
40

41 15 where \vec{e} is the electric field (V/m), \vec{b} is the magnetic flux density (Wb/m^2), \vec{j}_s is the current source
42 16 (A/m^2) and μ is the magnetic permeability (H/m). Here \vec{j} is the conduction current (A/m^2). In
43 17 the frequency domain, this conduction current, \vec{J} , is related to conductivity via Ohms law: $\vec{J}(s) =$
44 18 $\sigma(s) \vec{E}(s)$ where \vec{E} is the electric field. Converting this relationship to time domain using the inverse
45
46
47
48 Laplace transform yields:

$$49 \quad \vec{j}(t) = \sigma \otimes \vec{e} = \int_0^t \sigma(u) e(t-u) du. \quad (8)$$

50
51

52 20 Thus the current density depends upon the previous history of the electric field. As in Smith et al.
53 21 (1988), we represent total fields as $\vec{e} = \vec{e}^F + \vec{e}^{IP}$, $\vec{b} = \vec{b}^F + \vec{b}^{IP}$ and $\vec{j} = \vec{j}^F + \vec{j}^{IP}$, where superscript
54 22 F indicates fundamental and IP is induced polarization. Here fundamental fields indicate EM fields
55 23 when the chargeability is zero. Thus $\sigma(s) = \sigma_\infty$ (eq. 1) and there are no IP effects.
56
57

58 24 Equations (6) and (7) are written as
59
60

$$61 \quad \vec{\nabla} \times (\vec{e}^F + \vec{e}^{IP}) = -\frac{\partial}{\partial t} (\vec{b}^F + \vec{b}^{IP}), \quad (9)$$

1
2
3 6 *Seogi Kang and Douglas W. Oldenburg*
4
5

6
$$\vec{\nabla} \times \frac{1}{\mu}(\vec{b}^F + \vec{b}^{IP}) - (\vec{j}^F + \vec{j}^{IP}) = \vec{j}_s. \quad (10)$$

7
8

9 1 The fundamental equations can be written as
10
11

12 2
$$\vec{\nabla} \times \vec{e}^F = -\frac{\partial \vec{b}^F}{\partial t}, \quad (11)$$

13
14

15 3
$$\vec{\nabla} \times \frac{1}{\mu} \vec{b}^F - \vec{j}^F = \vec{j}_s. \quad (12)$$

16
17

18 3 where
19
20

21 4
$$\vec{j}^F = \sigma_\infty \vec{e}^F. \quad (13)$$

22
23

24 4 Subtraction of the fundamental fields yields the expressions for the IP fields
25
26

27 5
$$\vec{\nabla} \times \vec{e}^{IP} = -\frac{\partial \vec{b}^{IP}}{\partial t}, \quad (14)$$

28
29

30 5
$$\vec{\nabla} \times \frac{1}{\mu} \vec{b}^{IP} = \vec{j}^{IP}. \quad (15)$$

31
32

33 6 Let $F[\cdot]$ denote the operator associated with Maxwells equations, and let d denote the observations
34 7 that include both EM and IP effects. Keeping the same notation, we obtain $d = d^F + d^{IP}$, where d^F
35 8 and d^{IP} are fundamental and IP responses, respectively. Based on this, we define the IP datum as
36
37

38 32
$$d^{IP} = d - d^F = F[\sigma(t)] - F[\sigma_\infty]. \quad (16)$$

39
40

41 35 Here $F[\sigma_\infty]$ corresponds to the fundamental response (d^F). This subtraction acts as an EM-decoupling
42 36 process which removes the EM effects from the measured responses. This is the same procedure that
43 37 formed the basis of work by Routh & Oldenburg (2001).
44
45

46 42 **4 PSEUDO-CHARGEABILITY**
47

48 44 Writing
49

50 46
$$\vec{j}^{IP} = \vec{j}(t) - \vec{j}^F \quad (17)$$

51
52

53 48 and using eqs (2) and (8) we obtain
54

55 50
$$\vec{j}^{IP} = \sigma_\infty \vec{e}^{IP} + \vec{j}^{pol}, \quad (18)$$

56
57

58 54 where the polarization current (\vec{j}^{pol}) is
59

60 55
$$\vec{j}^{pol}(t) = \Delta\sigma(t) \otimes \vec{e}(t). \quad (19)$$

61
62

63 57 If the electric field has different characteristics for the inductive and galvanic sources this will
64 58 generate different features in the polarization current. We consider two cases: a) a galvanic source
65 59 without EM induction and b) an inductive source with EM induction. The first case corresponds to EIP
66 60

1
2
3
4 *On recovering distributed IP information from inductive source time domain electromagnetic data* 75
6 (Seigel 1959), and the second is associated with ISIP. Fig. 2 shows the amplitude of the fundamental
7 electric field, \vec{e}^F , in the earth for those two cases. For the galvanic source without EM induction
8 effects ($\frac{\partial b}{\partial t} = 0$), the electric field is instantaneously on or off in response to the transmitter. (Fig.
9 2 a). However, for the inductive source, the electric field in the off-time is not zero, but increases to
10 a peak and then decays as shown in Fig. 2 (b). The polarization current for the two sources will be
11 significantly affected by these different electric fields. To capture this difference in a linearized kernel
12 for the IP response, we define pseudo-chargeability ($\tilde{\eta}(t)$) as
13
14

15
16
17
$$\tilde{\eta}(t) = -\frac{\vec{j}^{pol}(t)}{\vec{j}^{ref}}, \quad (20)$$

18
19 where the reference current (\vec{j}^{ref}) is defined as
20
21

22
23
$$\vec{j}^{ref} = \sigma_\infty \vec{e}^{ref}. \quad (21)$$

24
25 Here \vec{e}^{ref} is the reference electric field, and we will explain our choice of \vec{e}^{ref} below. The pseudo-
26 chargeability defined in eq. (20) is the ratio of the polarization current to the reference current. This is
27 a small quantity and it plays an essential role in our linearization. To evaluate the pseudo-chargeability,
28 we need to identify a reference current or reference electric field, \vec{e}^{ref} , which is independent of time.
29 For EIP, we choose the value of the electric field achieved when there is no IP present, that is the value
30 shown in Fig. 2(a). For the inductive source we choose the peak electric field as shown in Fig. 2(b)31
32 Each pixel in the earth has its own reference electric field and time thus both \vec{e}^{ref} and t^{ref} have
33 a 3D distribution. For both EIP and ISIP cases, we mathematically present our choice of the reference
34 electric field as
35
36

37
$$\vec{e}^{ref} = \vec{e}^F(t) \otimes \delta(t - t^{ref}). \quad (22)$$

38
39 The reference time for the EIP case can be any time in the on-time.
40
4142
43 By rearranging eq. (20), we obtain
44
45

46
47
$$\vec{j}^{pol} = -\vec{j}^{ref} \tilde{\eta}(t). \quad (23)$$

48
49 This states that the polarization current has an opposite direction to the reference current, and is propor-
50 tional to the pseudo-chargeability, $\tilde{\eta}(t)$. This reversed direction of the current in a chargeable medium
51 results from the negative values of the time-dependent conductivity when $t > 0$ sec as shown in Fig.
52 1(b). This conceptual model about the polarization current shown in eq. (23) is consistent with Seigel
53 (1959)'s result. We note, that for any pixel, even if \vec{e}^{ref} attains the same value for an ISIP survey as
54 for an EIP survey, the pseudo-chargeability resulting from an ISIP survey will be less than that from
55 an EIP survey. We can infer from this that linearization techniques, which have worked so well in EIP
56 problems, should be successful in ISIP problems.
57
58
59
60

8 Seogi Kang and Douglas W. Oldenburg

5 LINEARIZATION

Following from the methodologies in EIP, our goal is to express the IP response, d^{IP} , as a linear function of the pseudo-chargeability, $\tilde{\eta}(t)$. That is we wish to write $d^{IP}(t) = J\tilde{\eta}(t)$, where J is a linear operator which is independent of time. In doing this we first consider a general EM system which is applicable to galvanic or inductive sources. For any volume pixel in the earth the amplitude and direction of the electric field can vary dramatically in time and thus the IP charging process can be complicated. However, if substantial polarization currents are developed we assume there was a sufficiently large electric field in a predominant direction to generate them. Although the direction of the electric field is constant the amplitude varies with time.

Let $\vec{e}(t)$ be approximated as

$$\vec{e}(t) \approx \vec{e}^{ref} \hat{w}(t), \quad (24)$$

where $\hat{w}(t)$ is defined as:

$$\hat{w}(t) = P_0[w^{ref}(t)]. \quad (25)$$

Here a projection $P_0[\cdot]$ of an arbitrary function, $f(t)$, is

$$P_0[f(t)] = \begin{cases} f(t) & f(t) \geq 0 \\ 0 & \text{if } f(t) < 0, \end{cases} \quad (26)$$

and

$$w^{ref}(t) = \frac{\vec{e}^F(t) \cdot \vec{e}^{ref}}{\vec{e}^{ref} \cdot \vec{e}^{ref}}. \quad (27)$$

$w^{ref}(t)$ is a dimensionless function that prescribes the time history of the electric field at each location along the direction of the chosen reference electric field, \vec{e}^{ref} . Negative values of $w^{ref}(t)$ are set to zero in accordance with our conceptual model that polarization currents have an opposite direction to the reference current (eq. 23). We redefine the pseudo-chargeability as

$$\tilde{\eta}(t) = \tilde{\eta}^I(t) \otimes \hat{w}(t). \quad (28)$$

The polarization current, \vec{j}^{pol} can be approximated with eq. (4) as

$$\vec{j}^{pol}(t) \approx -\tilde{\eta}^I(t) \otimes \hat{w}(t) \vec{j}^{ref}. \quad (29)$$

Substituting into eq. (18) yields

$$\vec{j}^{IP}(t) \approx \sigma_\infty \vec{e}^{IP}(t) - \tilde{\eta}^I(t) \otimes \hat{w}(t) \vec{j}^{ref} \quad (30)$$

and this yields

$$\vec{j}^{IP}(t) \approx \sigma_\infty \vec{e}^{IP}(t) - \vec{j}^{ref} \tilde{\eta}(t). \quad (31)$$

1
2
3
4 *On recovering distributed IP information from inductive source time domain electromagnetic data* 95
6 The second term, $-\vec{j}^{ref}\tilde{\eta}(t)$, corresponds to polarization currents. The first term, $\sigma_\infty\vec{e}^{IP}(t)$, is
7 usually omitted (Smith et al. 1988). This was because Smith et al. (1988) were mostly interested
8 in chargeable targets that were significantly conductive compared to the background. However, if
9 the conductivity of the chargeable target is similar to that of the background the first term could be
10 important.11
12 We include it here and will explore the conditions in which it is important. Because the refer-
13 ence current is static, any time-dependence in the polarization currents is encapsulated in the pseudo-
14 chargeability. The buildup and decrease of polarization currents is a slow process and we assume
15 therefore that this process does not produce induction effects ($\frac{\partial\vec{b}^{IP}}{\partial t} \approx 0$) and hence we can write
16

17
18
$$\vec{e}^{IP} \approx \vec{e}_{approx}^{IP} = -\vec{\nabla}\phi^{IP}, \quad (32)$$

19
20 where ϕ^{IP} is the electrical potential for IP. By taking the divergence of eq. (31), substituting \vec{e}^{IP} with
21 eq. (32), and carrying out some linear algebra, we obtain

22
23
$$\phi^{IP}(t) \approx -[\nabla \cdot \sigma_\infty \vec{\nabla}]^{-1} \nabla \cdot \vec{j}^{ref}\tilde{\eta}(t). \quad (33)$$

24
25 By applying the gradient we obtain

26
27
$$\vec{e}_{approx}^{IP} = \vec{\nabla}[\nabla \cdot \sigma_\infty \vec{\nabla}]^{-1} \nabla \cdot \vec{j}^{ref}\tilde{\eta}(t). \quad (34)$$

28
29 Thus, the electric field due to the IP effect can be expressed as a function of $\tilde{\eta}(t)$ in time. This form is
30 also applicable to the EIP case.31
32 For an inductive source, the data are either \vec{b} or its time derivative and hence we also need to
33 compute \vec{b}^{IP} or its time derivative. For this, we first compute \vec{j}^{IP} then use the Biot-Savart law. By
34 substituting eq. (34) into eq. (31), the approximated IP current density, \vec{j}_{approx}^{IP} can be expressed as
35

36
37
$$\vec{j}^{IP}(t) \approx \vec{j}_{approx}^{IP} = \bar{S}\vec{j}^{ref}\tilde{\eta}(t), \quad (35)$$

38
39 where

40
41
$$\bar{S} = \sigma_\infty \vec{\nabla}[\nabla \cdot \sigma_\infty \vec{\nabla}]^{-1} \nabla \cdot -\bar{I} \quad (36)$$

42
43 and \bar{I} is an identity tensor. Applying the Biot-Savart law we have:

44
45
$$\vec{b}_{approx}^{IP}(\vec{r}; t) = \frac{\mu_0}{4\pi} \int_{\Omega} \frac{\bar{S}\vec{j}^{ref}(\vec{r}_s) \times \hat{r}}{|\vec{r} - \vec{r}_s|^2} \tilde{\eta}(t) d\vec{r}_s, \quad (37)$$

46
47 where \vec{r}_s indicates a vector for a source location, and $\hat{r} = \frac{\vec{r} - \vec{r}_s}{|\vec{r} - \vec{r}_s|}$. If $\sigma_\infty\vec{e}^{IP}$ is omitted in \vec{j}^{IP} then
48 the tensor, \bar{S} becomes $-\bar{I}$. In this situation, the IP current is same as the polarization current, and it
49 always has an opposite direction to the reference current. This reversed current, along with Biot-Savart
50 law, provides a physical understanding about the negative transients in ATEM data when the earth is
51 chargeable.

10 Seogi Kang and Douglas W. Oldenburg

1 Observed data are often the time derivative of \vec{b} , hence by taking time derivative to the eq. (37),

2 we obtain

$$-\frac{\partial \vec{b}_{approx}^{IP}}{\partial t}(\vec{r}; t) = \frac{\mu_0}{4\pi} \int_{\Omega} \frac{\vec{S} \vec{j}^{ref}(\vec{r}_s) \times \hat{r}}{|\vec{r} - \vec{r}_s|^2} \left(-\frac{\partial \tilde{\eta}(t)}{\partial t} \right) d\vec{r}_s. \quad (38)$$

3 Here we have chosen to keep the minus signs in eq. (38) so that $-\frac{\partial \tilde{\eta}(t)}{\partial t}$ is positive when $\tilde{\eta}(t)$ is
4 decaying in time. Accordingly, the IP datum is given by $-\frac{\partial \vec{b}^{IP}}{\partial t}$.

5 The IP fields shown in eqs (34), (37) and (38) are linear functionals of $\tilde{\eta}$ and the equations for a
6 single time channel can be discretized in space as

$$\mathbf{d}^{IP} = \mathbf{J} \tilde{\eta}, \quad (39)$$

7 where \mathbf{J} is the corresponding sensitivity matrix. In particular when the observed datum is the time
8 derivative of \vec{b} , the linear relationship can be written as

$$\mathbf{d}^{IP} = \mathbf{J} \left(-\frac{\partial \tilde{\eta}}{\partial t} \right). \quad (40)$$

9 A detailed description for the discretization of the linearized kernel is shown in Appendices C1 and
10 C2. The representation in eq. (39) is valid for galvanic and inductive sources but the two assumptions:
11 a) $\vec{e} \approx \vec{e}^{ref} \hat{w}(t)$ and b) $\vec{e}^{IP} \approx -\vec{\nabla} \phi^{IP}$ need to be tested numerically for the case of inductive sources.

6 IP INVERSION METHODOLOGY

13 For the inversion of ISIP data, we focus on an ATEM survey with a coincident-loop geometry. From
14 the previous section, we first defined the IP datum (eq. 16) then linearized it as a function of the
15 pseudo-chargeability (eq. 39). The linearization was developed for a single transmitter. An ATEM
16 survey however includes many transmitters and each will excite a volumetric pixel differently. We
17 address this important issue in Appendix A1. It requires combining the pseudo-chargeabilities that
18 arise from individual transmitters into a transmitter-independent effective pseudo-chargeability. This
19 requires computing, and combining, the individual time histories of the electric fields due to each
20 transmitter into an effective time history. The result is that a d^{IP} datum for any transmitter takes the
21 form:

$$\begin{bmatrix} \mathbf{d}_1^{IP}(t) \\ \mathbf{d}_2^{IP}(t) \\ \vdots \\ \mathbf{d}_{nTx}^{IP}(t) \end{bmatrix} = \begin{bmatrix} \mathbf{J}_1 \\ \mathbf{J}_2 \\ \vdots \\ \mathbf{J}_{nTx} \end{bmatrix} \begin{bmatrix} \tilde{\eta}(t) \end{bmatrix}, \quad (41)$$

22 where $\mathbf{d}_k^{IP}(t)$ and \mathbf{J}_k indicates the IP datum and sensitivity matrix at k -th transmitter. Here $\tilde{\eta}(t)$
23 stands for an effective pseudo-chargeability, which represents pseudo-chargeability from all transmit-

1
2
3 *On recovering distributed IP information from inductive source time domain electromagnetic data* 11
4
5

6 ters. Hence, for a given effective pseudo-chargeability we can compute IP responses at all transmitters.
7
8 Eq. 41 shows that IP data for an ATEM survey are linearly related to effective pseudo-chargeability.
9
10 Information about chargeability can be obtained by solving a linear inverse problem. This is a common
11 problem in applied geophysics so we provide only an essential summary.
12
13
14

15 **6.1 3D IP inversion with a linearized kernel**
16

17 The linear inverse problem to recover chargeability is straightforward and is described in Oldenburg
18
19 & Li (1994). We rewrite eq. (39) as
20

$$\mathbf{d}^{pred} = \mathbf{J}\mathbf{m}, \quad (42)$$

23 where \mathbf{J} is the sensitivity matrix of linear problem, which corresponds to \mathbf{J} shown in eq. (39). Here,
24
25 \mathbf{d}^{pred} represents IP responses at a single time channel, \mathbf{m} denotes model parameters, which can be
26 either $\tilde{\eta}$ or $-\frac{\partial \tilde{\eta}}{\partial t}$. The important positivity constraint results because the intrinsic chargeability η is
27 restricted to the range [0,1].
28

29 The solution to the inverse problem is the model \mathbf{m} that solves the optimization problem
30
31

$$\text{minimize } \phi = \phi_d(\mathbf{m}) + \beta\phi_m(\mathbf{m}) \quad (43)$$

$$\text{s.t. } 0 \leq \mathbf{m},$$

32 where ϕ_d is a measure of data misfit, ϕ_m is a user-defined model objective function and β is
33
34 regularization or trade-off parameter.
35

36 We use the sum of the squares to measure data misfit
37
38

$$\phi_d = \|\mathbf{W}_d(\mathbf{A}\mathbf{m} - \mathbf{d}^{obs})\|_2^2 = \sum_{j=1}^N \left(\frac{d_j^{pred} - d_j^{obs}}{\epsilon_j} \right)^2, \quad (44)$$

39 where N is the number of the observed data and \mathbf{W}_d is a diagonal data weighting matrix which
40
41 contains the reciprocal of the estimated uncertainty of each datum (ϵ_j) on the main diagonal, \mathbf{d}^{obs} is
42
43 a vector containing the observed data, \mathbf{d}^{pred} is a vector containing calculated data from a linear eq.
44
45 given in eq. (42). The model objective function, ϕ_m , is a measure of the amount structure in the model
46
47 and upon minimization this will generate a smooth model which is close to a reference model, \mathbf{m}_{ref} .
48
49 We define ϕ_m as
50
51

$$\phi_m = \sum_{i=s,x,y,z} \alpha_i \|\mathbf{W}_i \mathbf{W}(\mathbf{m} - \mathbf{m}_{ref})\|_2^2, \quad (45)$$

52 where \mathbf{W} is a model weighting matrix, which will be defined below, \mathbf{W}_s is a diagonal matrix con-
53
54 taining volumetric information of prisms, and \mathbf{W}_x , \mathbf{W}_y and \mathbf{W}_z are discrete approximations of the
55
56

1
2
3 12 *Seogi Kang and Douglas W. Oldenburg*
4
5

6 first derivative operator in x , y and z directions, respectively. The α 's are weighting parameters that
7 balance the relative importance of producing small or smooth models (Tikhonov & Arsenin 1977).
8
9

10 Because in our ATEM data we have only a single datum for each transmitter, we do not have
11 intrinsic depth resolution. This is the same circumstance encountered when inverting magnetic data.
12 (Li & Oldenburg 1996). Correspondingly we apply a depth weighting through the model weighting
13 matrix (\mathbf{W}):
14
15

$$\mathbf{W} = \text{diag}(\mathbf{z} - \mathbf{z}_0)^{1.5}, \quad (46)$$

16 where \mathbf{z} and \mathbf{z}_0 are discretized depth locations and reference depth in the 3D domain.
17
18

19 Although we use the linear form of d^{IP} data (eq. 39), the inverse problem is nonlinear because
20 of imposed positivity on \mathbf{m} . We solve this constrained optimization problem using a projected Gauss-
21 Newton (GN) method (Kelley 1999). For further details of implementing this constrained optimization
22 see Marchant et al. (2012). The trade-off parameter, β , is determined using a cooling technique where
23 β is progressively reduced from some high value. The inversion is stopped when the tolerance is
24 reached (cf. Nocedal & Wright (1999); Oldenburg & Li (2005); Kang & Oldenburg (2015)).
25
26
27
28
29

30 For the implementation of our IP inversion algorithm, we use an open source python package
31 for simulation and gradient-based parameter estimation in geophysics called SIMPEG (Cockett et al.
32 2015).
33
34
35
36
37
38
39
40
41

42 6.2 IP inversion workflow

43 The 3D IP inversion methodology provides us with a capability to invert IP data at each time channel.
44 However, before we invert those IP data, we need to compute an estimate of σ_∞ which is needed for
45 EM-decoupling as well as generating the sensitivity matrix.
46
47

48 Considering the multiple tasks required to restore IP information from TEM data we use the
49 following workflow: (1) invert early-time TEM data that appear not to be contaminated with IP effects.
50 This yields a 3D conductivity model, σ_{est} which should be reasonably close to σ_∞ . (2) Forward model
51 σ_{est} to obtain the fundamental response d^F and subtract it from the observations to obtain d^{IP} data.
52 (3) Invert d^{IP} data to recover a pseudo-chargeability model at individual time channels using the
53 relationship in eq. (39). (4) Further, process the inversion outputs at multiple time-channels to estimate
54 the Cole-Cole, or equivalent IP parameters. For detailed descriptions of this step see Appendix B.
55
56
57
58

59 In the following we investigate each of the above steps via numerical simulations and test the
60 validity of our assumptions.

1
2
3 *On recovering distributed IP information from inductive source time domain electromagnetic data* 13
4
5

6 **7 NUMERICAL EXPERIMENTS**

7 For our numerical experiments we concentrate upon coincident-loop ATEM surveys. This choice is
8 made because of the observed negative transients that are direct indicators of IP phenomena (Smith &
9 Klein 1996; Kratzer & Macnae 2012; Kang & Oldenburg 2015), and the extensive use of this survey
10 by industry.

11 We begin with a simple IP model composed of a chargeable block in a halfspace as shown in
12 Figure 3. Cole-Cole parameters of the block are $\eta = 0.2$, $\tau = 0.005$ and $c = 1$. The conductivity of the
13 halfspace, (σ_1) is 10^{-3} S/m, whereas σ_2 , the conductivity at infinite frequency for the chargeable body,
14 is variable. We consider three cases: a) canonical ($\sigma_2 = \sigma_1$), b) conductive ($\sigma_2 = 10^2 \times \sigma_1$) and c)
15 resistive models ($\sigma_2 = 10^{-2} \times \sigma_1$). The 3D earth is discretized with $50 \times 50 \times 50$ m core cells and the
16 number of cells in the domain is $41 \times 41 \times 40$. The size of the chargeable body is $250 \times 250 \times 200$ m and
17 the top boundary is located 50 m below the surface. The EMTDIP code (Marchant et al. 2014) is used
18 to compute forward ATEM responses that include IP effects. The survey consisting of 11 soundings
19 along each of 11 lines is shown in Fig. 3(a). Data are from a coincident-loop system and the flight
20 height is 30 m above the surface; the radius of the loop is 10 m. A step-off transmitter waveform is
21 used and the range of the observed time channels is 0.01-60 ms. The observed responses can be the
22 vertical component of \vec{b} or $\frac{\partial \vec{b}}{\partial t}$.

23 In this section, we first decompose the observed responses and the total currents into fundamental
24 and IP portions to aid in the basic understanding of IP effects in ATEM data. Second, we validate the
25 linearized functional by computing the approximate IP current and IP responses, and compare these
26 with the true values. Third, we invert the IP data and recover 3D distributions of pseudo-chargeability
27 at multiple times. Lastly, we use the recovered pseudo-chargeabilities to examine the potential to
28 extract intrinsic Cole-Cole parameters.

29 **7.1 IP responses**

30 Using the EMTDIP code and carrying out two simulations, we compute the IP data via subtraction in
31 eq. (16). Fig. 4 shows the observed, fundamental, and IP responses at a sounding location above the
32 center of the chargeable body for (a) canonical, (b) conductive and (c) resistive models. Both b_z and
33 $-\frac{\partial b_z}{\partial t}$ data are shown. The IP effects are most noticeable for the conductive body and we turn attention
34 to this example first. The IP response starts to significantly affect the observations near 0.6 ms and the
35 observed responses show a sign reversal near 1 ms. Beyond that time the signal is dominated by the IP.
36 The dashed line in Fig. 4(b) shows that after turning off the transmitter current, the IP current increases
37 (as inferred by the magnitude of the b_z field) until about 1 ms and then decreases. We interpret this
38 in terms of charging and discharging phases and a vertical dashed line in the figure defines the two
39

1
2
3 14 *Seogi Kang and Douglas W. Oldenburg*
4
5

6 phases. In the charging phase at early times the EM effects dominate and IP signals are not expected
7 to be observed. In the discharging phase, which occurs at later time, the IP effects may eventually
8 dominate the EM effects. The maximum of the b_z^{IP} corresponds to the zero crossing for $-\frac{\partial b_z^{IP}}{\partial t}$ but
9 the times at which the IP signal becomes dominant are delayed compared to b_z^{IP} . By comparing the
10 observations with the fundamental fields we see that the IP signal could be recognized in the b_z data
11 near 0.7 ms and near 2.0 ms in the $-\frac{\partial b_z}{\partial t}$ data.
12
13

14 The plots for the canonical and resistive bodies show that the time that separates charging and dis-
15 charging occurs earlier than for the conductive body. This is a reflection that the fundamental currents
16 reside for a longer time in a conductor. For the canonical body, a significant difference between the
17 measured responses and the fundamental fields occur about 0.9 ms for b_z and about 2 ms for $-\frac{\partial b_z}{\partial t}$.
18 The amplitudes of the IP responses are significantly smaller than those for the conductor. Lastly, there
19 is little IP signal for the resistive body; the IP signal is much smaller than the fundamental response
20 throughout the given time range. This is a consequence of the small fundamental currents in the resis-
21 tor.
22
23

24 The decay curves from a sounding location provide insight about the IP response but more is
25 gleaned by looking at data from all sounding locations in the ATEM survey. We focus on b_z^{IP} for the
26 conductive block at selected time channels. Fig. 5 shows interpolated maps of the observed, funda-
27 mental and IP responses at (a) 0.86 ms and (b) 6.7 ms which are respectively included in the charging
28 and discharging times. For the conductive block, 0.86 ms is close to the peak time when transition
29 from charging to discharging occurs, but it is still included in the charging time. At this time, the ob-
30 servations are dominated by the fundamental response and no negative values, which are the signature
31 of the IP effect, are observed. Subtracting the fundamental however, yields a residual d^{IP} data map
32 that has a strong negative. This example shows that our EM-decoupling procedure can work satisfac-
33 torily. At 6.7 ms, obtaining good IP data are easier because the observed data already show negative
34 values. There is still a weak fundamental field and the subtraction process improves the d^{IP} response.
35 The d^{IP} data at 0.86 ms and 6.7 ms shown in Fig. 5 are of sufficient quality to be inverted.
36
37

38 27 **7.2 Polarization currents**
39
40

41 28 To evaluate the polarization current shown in eq. (19) for the linear functional, we assumed $\vec{e}(t) \approx$
42 $\vec{e}^{ref} w^e(t)$ and defined our reference current as $\vec{j}^{ref} = \sigma_\infty \vec{e}^{ref}$. That yielded our approximation of
43 the polarization current to be $\vec{j}^{pol}(t) \approx -\vec{j}^{ref} \tilde{\eta}(t)$. This approximation requires that the polarization
44 current has a direction antiparallel to the reference current, and the direction is the same for all times.
45 With this approximation the time dependence for the polarization currents only occurs through the
46 scalar $\tilde{\eta}(t)$. We investigate the approximation by evaluating both reference and polarization currents
47
48

1
2
3 *On recovering distributed IP information from inductive source time domain electromagnetic data* 15
45 numerically. From eq. (22), a reference current can be considered as the maximum fundamental current
6 that occurred throughout the time history. To evaluate polarization currents we rearrange eq. (18) as
7 $\vec{j}^{pol} = \vec{j}^{IP} - \sigma_\infty \vec{e}^{IP}$.
89 Here we limit our attention to canonical and conductive blocks. Figs 6(a) and (b) show reference
10 currents for the canonical and conductive blocks, respectively. A transmitter is located at (-200 m, 0
11 m, 30 m) and marked as a white solid circle in the figure, where (\cdot, \cdot, \cdot) refers to a point at (easting,
12 northing, depth). Reference currents for the canonical block are circular, centered on the transmitter
13 location, and decay with distance. For the conductive block, additional vortex currents are induced.
14 We compare these reference currents with the polarization currents. Fig. 7 shows the plan and section
15 view maps of the polarization currents at 0.86 ms. Comparisons of Figs 6 and 7 clearly show that
16 polarization currents for both canonical and conductive blocks are oppositely aligned with respect to
17 their reference current. This was the hypothesized outcome. Fig. 8 shows that the direction of polar-
18 ization currents at 6.7 ms is similar to those at 0.86 ms. Thus both for the canonical and conductive
19 blocks, the direction of polarization currents after 0.86 ms is constant in time.
2021 Of particular interest is the difference in character of the polarization currents for the canonical
22 and conductive bodies. For the canonical body the currents look like anomalous galvanic currents that
23 would be expected from an EIP survey. The resultant magnetic fields will be similar to the magnetic
24 fields obtained from an electric dipole. For the conductive case however, the currents are circular and
25 they reflect the vortex nature of the induced currents. The resultant magnetic fields are those associated
26 with a magnetic dipole. The polarization currents inside a body are therefore complicated by the fact
27 that they are a mixture of galvanic and inductive processes. Our choice of reference currents effectively
28 incorporates this complexity.
2930 **7.3 IP currents**
3132 The IP currents, as provided in eq. (18), are given as
33

34
$$\vec{j}^{IP} = \sigma_\infty \vec{e}^{IP} + \vec{j}^{pol}. \quad (47)$$

35

36 In most analyses, e.g. Smith et al. (1988), the term $\sigma_\infty \vec{e}^{IP}$ is neglected. We have included this
37 term but with an approximation that $\vec{e}^{IP} \approx -\nabla\phi$ (eq. 32). Here we investigate these approximations,
38 and under what circumstances they hold.
3940 Using the forward modelling we can evaluate \vec{e}^{IP} . This field can be broken into galvanic and
41 inductive parts using the Helmholtz decomposition (Bladel 1959): $\vec{e} = -\vec{\nabla}\phi - \vec{a}$ so that $\vec{j}^{IP} =$
42 $\vec{j}^{pol} - \sigma_\infty \vec{\nabla}\phi^{IP} - \sigma_\infty \vec{a}^{IP}$. In our work we included the effects from the scalar potential but neglected
43 any contribution from the vector potential. We look at the contributions of each of these terms for the
44

16 *Seogi Kang and Douglas W. Oldenburg*

1 three cases of canonical, conductive and resistive bodies. Fig. 9 respectively shows plan view maps of
2 \vec{j}^{pol} , $-\sigma_\infty \vec{\nabla} \phi^{IP}$, and $-\sigma_\infty \vec{a}^{IP}$ for (a) canonical, (b) conductive, and (c) resistive models at 0.86 ms.

3 Inside the body, the polarization currents have the greatest strength and the strength of these cur-
4 rents is largest in the conductive body and smallest in the resistive body. In all cases, the polarization
5 currents are the largest contribution to \vec{j}^{IP} . The second column in Fig. 9 is related to the scalar poten-
6 tial for the electric field or effectively to the galvanic currents. These exist both inside and outside the
7 chargeable body. Again, these are largest for the conductive body. We note that inside the body, these
8 currents have a direction that is opposite to the polarization currents. The third column is associated
9 with the vector potential for \vec{e}^{IP} and is associated with vortex currents. The effects of these currents
10 have not been included in our linearized approximations. These currents are quite small for the canon-
11 ical and resistive models but their amplitude starts to be comparable to the galvanic portion for the
12 conductive model.

13 We evaluate \vec{j}^{IP} and its components at two locations in the body for conductive model. These are
14 denoted by white stars in the figures. For both locations, the polarization currents have the greatest
15 strength and the vortex currents are smaller than the galvanic currents. The IP current is smaller than
16 the polarization current mostly because the galvanic IP currents are in the opposite direction compared
17 to the polarization currents. The results are tabulated in Table 1.

18 The above figures provide insight about the three contributions to \vec{j}^{IP} but of ultimate interest is the
19 effect of these currents on the measured data. We therefore apply the Biot-Savart law to each current. It
20 suffices to work with the conductive case. Fig. 10 shows IP responses computed from the polarization
21 current (stars), galvanic (rectangles) and inductive portions (circles) of the IP current. Here solid and
22 empty markers show negative and positive signs, respectively. The polarization current has the major
23 contribution to the IP response although it is larger than the true value. This overshoot is primarily
24 negated by the galvanic portion of IP responses and further reduced because of the vortex currents.
25 We notice that the contribution of the galvanic currents is generally larger than those due to the vortex
26 currents except near 0.4 ms. At 6.7 ms, the amplitude of the IP response due to the polarization current
27 is about 130 percent of the true one, while galvanic portion is 30 percent. These results show that the
28 assumption by Smith et al. (1988) is reasonable, but incorporation of the galvanic portion to the IP
29 datum is significant at later times. The inductive portion of the IP responses is small compared to the
30 galvanic portion except for the time before 0.2 ms, and hence ignoring this is generally justified.

31 **7.4 Validations of linearization**

32 Forward modelling using eq. (39) requires that we have adequately estimated the IP currents and we
33 can evaluate their response using the Biot-Savart law. To validate this we first compute approximate

1
2
3 *On recovering distributed IP information from inductive source time domain electromagnetic data* 17
45
6 IP currents using eq. (35), and first compare them with the true IP currents. It suffices to work with
7 the conductive model which is the most challenging. Fig. 11 compares the true and approximate IP
8 currents at 0.86 ms. The approximate IP currents match well, both in direction and amplitude, with
9 the true IP currents both inside and outside the body. As shown in Fig. 12 the agreement improves
10 as time increases (see the directions of the true and approximate IP currents at (0,0,-350) on the right
11 panels of Figs 11 and 12).
12
1314
15 We next test the validity of the computation of IP responses by using our formulation of the Biot-
16 Savart law. To do this we compute the “true” IP responses by subtracting the fundamental response
17 from the observations. We next compute the IP responses by evaluating the Biot-Savart law with the
18 true IP currents shown in Fig. 12(a). As shown in Fig. 13 the agreement between these responses
19 is very good after 0.01 ms. This validates the use of the Biot-Savart law (eq. 37). Lastly, we want
20 to compare responses, evaluated through the Biot Savart law, but use our approximated IP currents
21 (Fig. 12b). The results are shown in Fig. 13. The responses obtained from using our approximate
22 currents have lower amplitude and differ by 33 percent at the extreme. The difference decreases with
23 increasing time. Overall the two curves are in reasonable agreement, thus validating our linearized
24 forward modeling (eq. 39).
25
2627
28 The same analysis of comparing true and approximate d^{IP} data was carried out for the canonical
29 and resistive models. As shown in Fig. 13, the true and approximate d^{IP} for both cases show good
30 agreements. We note however, that despite the fact that our linear functional reasonably explains d^{IP}
31 data for the resistive case, the IP signals are very small compared to EM signals and we likely cannot
32 identify them in practice.
33
3440
41
42
43
44 **7.5 3D IP inversions**
4546
47 Using our linearized sensitivity, we now proceed with 3D IP inversion, which recovers a pseudo-
48 chargeability given by eq. (39). We limit our attention to the conductive case. For the computation of
49 the sensitivity we use the true conductivity (σ_∞) and then invert data at successive time channels and
50 recover 3D pseudo-chargeability at multiple times. Our 3D inversion is based upon (Oldenburg & Li
51 1994; Li & Oldenburg 2000), and it requires some choices for inversion parameters.
52
5354
55 For data uncertainties, we use one percent of the maximum amplitude of the observed data ($0.01\max(|\mathbf{d}^{obs}|)$).
56
57 Coefficients for smallness and smoothness are set to $\alpha_s = 10^{-5}$ and $\alpha_x = \alpha_y = \alpha_z = 1$, respec-
58 tively. The reference model is zero, which means the pseudo-chargeability of every cell is zero, and
59 we applied a depth weighting. The need for a depth weighting arises because the sensitivity function
60 J is primarily controlled by a $1/r^3$ decay associated with the Biot-Savart kernels. Thus an ATEM data

1
2
3 18 *Seogi Kang and Douglas W. Oldenburg*
4
5
6

7 1 set is not unlike a magnetic data set where it is well established that a depth weighting is required to
8 2 image objects at depth. The following example illustrates this.
9
10

11 3 We first generate IP responses at a single time using the linear functional and specifying that
12 4 the pseudo-chargeability is unity inside the body and zero outside, as shown in Fig. 14(a). Fig. 14(b)
13 5 shows the recovered pseudo-chargeability without depth weighting. The recovered anomalous pseudo-
14 6 chargeability is concentrated near the surface and the magnitude of the pseudo-chargeability is under-
15 7 estimated; it is ~ 0.2 rather than unity. By using the depth weighting shown in eq. (46), the IP body is
16 8 imaged closer to its true depth (Fig. 14b). Also, the magnitude of the recovered pseudo-chargeability
17 9 (~ 0.6) is closer to the true value than the result without depth weighting. Based on this analysis, we
18
19 10 use the same depth weighting for our following examples.
20
21

22
23
24 11 *7.5.1 Incorrect conductivity*
25
26
27

28 12 The background conductivity σ_∞ plays a central role in our analysis. It is used in the EM-decoupling
29 13 process and it is also needed to compute the linearized sensitivities for inversion. Since we need to
30 14 estimate σ_∞ , usually through the inversion of TEM data, it will never be correct. Here we explore
31 15 some effects of an incorrect conductivity but the consequences are problem dependent.
32

33 16 We return to our conductive block in a halfspace and evaluate the d^{IP} data when the background
34 17 is the true value ($\sigma_1 = 10^{-3}$ S/m) as well as a factor of two too large (2×10^{-3} S/m) and a factor of
35 18 two too small (5×10^{-4} S/m). The data along a survey line are plotted in Fig. 15.
36
37

38 19 We invert these three IP responses, and provide sections of the recovered pseudo-chargeability at
39 20 0 m-northing. Fig. 16(a), (b) and (c) correspondingly show the recovered pseudo-chargeability when
40 21 the conductivity is: the true value, too high, or too low. With the correct conductivity the geometry
41 22 of the IP body is reasonably recovered. When the conductivity is too high, the d^{IP} have a negative
42 23 bias that results in larger pseudo-chargeabilities and positive-valued artifacts near the IP body (Fig.
43 24 16b). When the conductivity is too small, the IP data have a positive bias and this produces negative-
44 25 valued artifacts near the IP body (Fig. 16c). White dotted contours shown in Fig. 16(c) shows zero-
45 26 crossing lines, which delineate those negative-valued artifacts. However, based on the definition of the
46 27 pseudo-chargeability shown in eq. (A.5), the sign of the pseudo-chargeability should be positive. By
47 28 incorporating positivity as a constraint in the inversion, and re-inverting the IP data that have a positive
48 29 bias, we obtain the result in Fig. 16(d). This is a much better result than Fig. 16(c), and it shows that
50 30 the positive constraints prevent fitting positive residual fields. We shall use this positivity constraint
51 31 for our following 3D IP inversion examples.
52
53

54 32 The background conductivity is also needed when computing the sensitivity function, since we
55 33 need the reference electric field, which is dependent on conductivity. An incorrect conductivity will
56
57
58
59
60

1
2
3 *On recovering distributed IP information from inductive source time domain electromagnetic data* 19
4
51 then affect the sensitivity function. In order to test this, we compute the sensitivity matrix using a
2 halfspace conductivity model ($\sigma_\infty = \sigma_1$). Fig. 17 compares the recovered pseudo-chargeability from
3 the 3D IP inversion of the IP datum at 0.86 ms with the true and incorrect sensitivity function using
4 halfspace conductivity. There is not a large difference between the two inversions which suggests
5 that an approximate conductivity may still provide sensitivities that are adequate for inversion. This
6 parallels results from EIP where even an approximate conductivity can still yield good results when
7 inverting the data. Thus there is robustness in our sensitivity function with respect to an incorrect
8 conductivity.
9
1011 *7.5.2 Extracting intrinsic IP parameters*
12
1314 By applying our inversion to each time channel of d^{IP} data separately, we can recover 3D distri-
15 butions of pseudo-chargeability at multiple times. The pseudo-chargeability at each time carries dif-
16 ferent information about the state of polarization and we can use these to recover information about
17 intrinsic IP parameters. Diverse time-dependent conductivity models such as the Cole-Cole model and
18 stretched-exponential can be used for this interpretation. We use the Cole-Cole model with $c = 1$. We
19 parametrize pseudo-chargeability at a single pixel in terms of chargeability and time constant as de-
20 scribed in Appendix B, and solve a small inverse problem. In previous works about this task for the
21 EIP problem (Yuval & Oldenburg 1997; Hördt et al. 2006), the convolution shown in eq. B.1 was not
22 explicitly mentioned because $\hat{w}(t)$ is a step-off or -on function and it does not change for different
23 cells and transmitters. This allowed an explicit equation for a step-off or -on response of the pseudo-
24 chargeability to be derived. However, in our work, convolution plays a fundamental role and needs to
25 be explicitly addressed when extracting intrinsic IP parameters. Also, the details regarding how we
26 defined the effective pseudo-chargeability (eq. A.8) needs to be included. Except for this additional
27 complexity related to the convolution, our approach parallels that of Yuval & Oldenburg (1997); Hördt
28 et al. (2006).
29
3031 As an example, we use the conductive and chargeable block presented in the previous section
32 and invert 14 time channels of data ranging from 1-10 ms. The EM data are forward modelled using
33 EMTDIP code and the true σ_∞ model is used to evaluate the IP datum and compute the sensitivity
34 function. The recovered pseudo-chargeability from one of the 14 inversions is shown in Fig. 17a. In
35 that pseudo-chargeability model, we select cells that have a pseudo-chargeability value greater than
36 0.001, and then carry out the nonlinear inversion to estimate the time constant, τ , and chargeability,
37 η , for each cell separately. The forward modelling for this inversion is shown in eq. (A.8), which
38 requires $w^e(t)$ (eq. A.9). The $w^e(t)$ for a pixel in the block is shown in Fig. A2.
39
4041 Fig. 18(a) and (b) correspondingly show the estimated time constants and chargeability as section
42
43

1
2
3 20 *Seogi Kang and Douglas W. Oldenburg*
4
5
6
7
8
9
10
11
12
13
14
15
16
17
18
19

maps. The estimated time constants show good agreement with the true value $\tau = 0.005$. There is less agreement about chargeability for which the true value is $\eta = 0.2$. Recovered values range from about 0.04-0.2 so most values are underestimated. In Fig. 19, we also provide time decays of the observed and predicted pseudo-chargeabilities at a single pixel marked as a black empty rectangle in Fig. 18. The estimated time constant, τ_{est} , and chargeability, η_{est} , for this pixel are 0.0046 and 0.09, respectively. These results imply there is greater stability on recovering the time constant than on recovering chargeability with our approach. Again, similar experiments were carried out for the canonical and resistive bodies and the conclusions were also that the time constant was adequately recovered with better fidelity than was the chargeability.

20
21
22
23
24
25
26
27

10 8 ESTIMATING THE BACKGROUND CONDUCTIVITY

28
29
30
31
32
33
34
35
36
37
38
39
40
41
42
43
44
45
46
47
48
49
50
51
52
53
54
55
56
57
58
59
60

In this paper we have generally assumed that a good estimate of σ_∞ was available. If it is, then we have shown that we can obtain IP data by subtracting the fundamental responses from the observations. This process is sometimes referred to as EM-decoupling and its solution has been a long-standing goal in exploration geophysics. For the ATEM survey, one potential approach to finding σ_∞ is to invert the early-time data in which the EM response is much larger than the IP response (for example inverting time channels 2 to 10 ms in the left panel of Fig. 4b). The success of this method is dependent upon three factors: (a) that the data are uncontaminated by IP effects (i.e. there is no IP-coupling); (b) that the data acquisition is sufficiently dense in space and in time so that needed information about σ_∞ is obtained; (c) an inversion algorithm exists that can generate a 3D conductivity model. Even so, the recovered conductivity will not be equal to the true conductivity. In Section 7.5.1, we showed how the estimated IP data are affected when a background halfspace is altered by a factor of two. This was a simple example but it illustrated the general effects of an incorrect conductivity and ameliorating effects of the positivity constraint in the IP inversion (eq. 43). The problem will become more challenging when there is substantial spatial variation between the true and approximate conductivity. It is conceivable that if the ATEM data show no negative values and if the conductivity approximation is sufficiently poor then our EM-decoupling procedure will fail to produce quality IP data. This will have to be addressed for each survey. What we did demonstrate here was that even an approximate σ_∞ is sufficient to generate the sensitivities, and hence if quality IP data can be isolated from observations, then our techniques can unravel the data to generate information about the polarization structure.

1
2
3 *On recovering distributed IP information from inductive source time domain electromagnetic data* 21
4
5

6 **9 CONCLUSIONS**

7
8 In this paper, we have introduced a procedure for recovering IP information from TEM data with
9 inductive sources. Three main steps are required: 1) subtraction of the fundamental responses from
10 the observations to generate IP data, 2) linearization of the IP responses as a function of the pseudo-
11 chargeability, and 3) restoration of 3D pseudo-chargeability at multiple times, and further interpreta-
12 tion of the pseudo-chargeability to extract intrinsic IP parameters like Cole-Cole model. We used the
13 ATEM survey to test our IP inversion procedure.
14
15

16 The first step requires a good estimate for the background conductivity σ_∞ . This is important for
17 two reasons. σ_∞ is used to generate the fundamental fields that are subtracted from the observations
18 to produce the IP data. This conductivity is also needed to compute the sensitivities for our linear
19 relationship between the IP data and pseudo-chargeability. To construct σ_∞ we invert early time data
20 that is felt to be uncontaminated with significant IP responses. For the mid-time data, subtraction of
21 the fundamental responses from the observations revealed negative data even though the observations
22 were positive. At very late times this subtraction process was not necessary since the EM fields had
23 sufficiently decayed. We note that maps of the d^{IP} data can, in themselves, be a useful processing
24 tool for detecting anomalies. To carry out that analysis we assumed that σ_∞ was known. For practical
25 applications, where we propose inverting early TEM data to recover σ_∞ , the effects on an incorrect
26 σ_∞ on the d^{IP} data will need to be investigated.
27
28

29 The second item, linearization of the IP responses with respect to a pseudo-chargeability, required
30 that a number of assumptions be made. Our pseudo-chargeability is defined as the ratio of the polar-
31 ization current to a reference current. Unlike the EIP case, the electric fields for an inductive source
32 do not achieve steady-state and hence neither do the polarization currents. To address this important
33 difference we evaluate the fundamental fields at each location in the earth and generate a reference
34 electric field that has the direction and magnitude of the field at the time when the fundamental field
35 reaches its maximum value. The pseudo-chargeability at a point in the earth thus depends upon the
36 chargeability, the reference electric field, and the time history of the fundamental electric field. The sit-
37 uation becomes more complicated when data from many transmitters are to be inverted simultaneously
38 because the time history of the electric field at a point in the earth is different for each transmitter. We
39 handle this by defining an effective pseudo-chargeability and an associated reference electric field that
40 accommodates, in a least squares fashion, the effects of all transmitters acting on a single cell.
41
42

43 To have confidence in when, and under what circumstances, our approximations are sufficiently
44 valid, we proceed with a number of rigorous tests. First we introduce 3 test models which are respec-
45 tively a chargeable block in a halfspace. The block can be conductive, canonical, or resistive with
46 respect to the background. Our evaluations show that: (a) our choice of reference electric field and
47
48

1
2
3 22 Seogi Kang and Douglas W. Oldenburg
4
5

6 its time history produces a good estimate of the polarization currents; (b) the IP currents are domi-
7 nated by the polarization currents, which is an assumption that is often made. However, the galvanic
8 and vortex currents arising from the scalar and vector potentials in the Helmholtz decomposition of
9 \bar{e}^{IP} can be significant in some circumstances. The galvanic currents are the second most important
10 contribution to the IP currents and, in the body, they have a direction that opposes the direction of
11 the polarization currents. In our work we have included the galvanic currents and neglected the vor-
12 tex currents which are almost always smaller than the galvanic currents; (c) the IP responses can be
13 accurately evaluated using the Biot-Savart law provides accurate results; (d) with our approximate IP
14 currents, the predicted responses are in reasonably good agreement with true values although they are
15 underestimated for the highly conductive example. These results lead us to infer that our linearized
16 formulation $d^{IP}(t) = J\tilde{\eta}(t)$ is a viable representation for the forward modelling at late times when
17 the IP effects are substantial compared to the EM effects. (e) For the multi-transmitter case we derived
18 an effective pseudo-chargeability which is a linear combination of the pseudo-chargeability of each
19 transmitter. These were forward modelled with the linearized formulation and compared to the true
20 responses. The values were underestimated for the conductive model but were almost identical for the
21 canonical and resistive models.
22
23

24 The third component is the 3D inversion of the IP data using the linearized formulation to recover
25 an effective pseudo-chargeability for each cell. ATEM data have only one receiver for each transmitter
26 and a data map at a single time channel is essentially a potential field. The data do not have intrinsic
27 resolving power and hence, as in magnetics or gravity inversions, we attempt to counteract this by in-
28 troducing a depth weighting. When this is done, our 3D IP inversion recovers a reasonable geometric
29 shape and location of the chargeable body but the amplitude is underestimated. For the inversion it
30 is assumed that a good estimate of σ_∞ is available. An incorrect σ_∞ has two effects in the inversion.
31 Firstly it can generate errors in the d^{IP} data because the fundamental field, which is subtracted from
32 the observations, is incorrect. To obtain insight we looked at the effects when σ_{est} was too low or two
33 high. This respectively yielded positive or negative residual fields in the IP response. A positivity con-
34 straint on the pseudo-chargeability (similar to that used in EIP surveys) greatly ameliorated the effects
35 of the positive residuals. The other avenue by which an incorrect σ_∞ can affect the inversion is through
36 the sensitivity matrix J . We showed that, even with an approximate conductivity, we recovered impor-
37 tant information about the chargeable body such as geometric shape and location. An inversion of the
38 data at a particular time channel provides information about the effective pseudo-chargeability for each
39 pixel. Inversions carried out at multiple time channels therefore generates a pseudo-chargeability as a
40 function of time for each pixel. The pseudo-chargeability for pixels that had significant chargeability
41 were subsequently fit to a Cole-Cole model to estimate τ and η by assuming $c = 1$. The estimated τ
42
43
44
45
46
47
48
49
50
51
52
53
54
55
56
57
58
59
60

1
2
3 *On recovering distributed IP information from inductive source time domain electromagnetic data* 23
4
5

6 1 was close to the true value whereas η was underestimated and less robust. This suggests that there is
7 2 a possibility to extract intrinsic IP parameters from the recovered pseudo-chargeability from ATEM
8 3 surveys.

9 4 Our IP inversion procedure provides a framework for recovering IP information from inductive
10 5 source EM surveys and in particular from ATEM surveys that are commonly flown. Our examples
11 6 show: (a) that the horizontal location of a target body can be well recovered; (b) the overall geometry
12 7 might be recovered but much of that inference requires a depth weighting to be included; (c) we can
13 8 recover estimates of intrinsic τ and η that may be useful for distinguishing between two chargeable
14 9 targets. Our procedure depends on having a good estimate for the background conductivity and this
15 10 aspect this should be carefully investigated in future practical applications. Other areas for follow-
16 11 up research include quantifying depth of resolution for airborne IP surveys, and general strategies
17 12 for extracting intrinsic IP parameters from our effective pseudo-chargeabilities. Lastly, our numerical
18 13 examples only treated the ATEM survey, but the procedure is applicable to other types of inductive
19 14 source TEM survey such as a large-loop TEM with many receivers. There will be details that need to
20 15 be addressed for those applications but the work presented here provides the fundamental background
21 16 for those future studies whose goal is to extract some information about polarization from an inductive
22 17 time domain system.

33
34
35
36
37 18 **ACKNOWLEDGMENTS**

38
39 19 We wish to thank David Marchant for providing EMTDIP code, and other UBC-GIF members for
40 20 their constructive comments. We would like to thank Rowan Cockett and Lindsey Heagy for their
41 21 contributions to SIMPEG (<http://www.simpeg.xyz>).

42
43
44
45
46
47 22 **REFERENCES**

- 48
49 23 Bladel, J., 1959. On helmholtz's theorem in finite regions, *Antennas and Propagation, IRE Transactions on*,
50 24 **7**(5), 119–119.
- 51
52 25 Chen, J. & Oldenburg, D., 2003. 3-D inversion of magnetic induced polarization data, *ASEG Extended Ab-*
53 26 *stracts*, **1**(1), 1–11.
- 54
55 27 Cockett, R., Kang, S., Heagy, L. J., Pidlisecky, A., & Oldenburg, D. W., 2015. SimPEG: An open source
56 28 framework for simulation and gradient based parameter estimation in geophysical applications (submitted),
57 29 *Computers and geoscience*.
- 58
59 30 Cole, K. S. & Cole, R. H., 1941. Dispersion and absorption in dielectrics i. alternating current characteristics,
60 31 *The Journal of Chemical Physics*, **9**(4).

24 Seogi Kang and Douglas W. Oldenburg

- 1 Dias, C. A., 2000. Developments in a model to describe lowfrequency electrical polarization of rocks, *GEO-
2 PHYSICS*, **65**(2), 437–451.
- 3 ElKaliouby, H. & Eldiwany, E., 2004. Transient electromagnetic responses of 3D polarizable body, *Geo-
4 physics*, **69**(2), 426–430.
- 5 Fiandaca, G., Auken, E., Christiansen, A. V., & Gazoty, A., 2012. Time-domain-induced polarization: Full-
6 decay forward modeling and 1D laterally constrained inversion of Cole-Cole parameters, *Geophysics*, **77**(3),
7 E213.
- 8 Fink, J., McAlister, E., Sternberg, B., Wieduwilt, W., & Ward, S., 1990. *Induced Polarization Applications
9 and Case Histories*, Society of Exploration Geophysicists.
- 10 Flis, M. F., Newman, G. A., & Hohmann, G. W., 1989. Inducedpolarization effects in timedomain electromag-
11 netic measurements, *Geophysics*, **54**(4), 514–523.
- 12 Haber, E., 2014. *Computational Methods in Geophysical Electromagnetics*, Society for Industrial and Applied
13 Mathematics, Philadelphia, PA.
- 14 Hodges, G. & Chen, T., 2014. IP effect in airborne TDEM data: Model studies and field examples, *SEG
15 Technical Program Expanded Abstracts*, **158**, 828–832.
- 16 Hördt, A., Hanstein, T., Hönig, M., & Neubauer, F. M., 2006. Efficient spectral IP-modelling in the time
17 domain, *Journal of Applied Geophysics*, **59**(2), 152–161.
- 18 Kang, S. & Oldenburg, D., 2015. Recovering IP information in airborne-time domain electromagnetic data,
19 *ASEG Extended Abstracts*, **1**(1), 1–4.
- 20 Kelley, C. T., 1999. *Iterative Methods for Optimization*, Society for Industrial and Applied Mathematics.
- 21 Kemna, A., Binley, A., Cassiani, G., Niederleithinger, E., Revil, A., Slater, L., Williams, K. H., Orozco, A. F.,
22 Haegel, F. H., Hördt, A., Kruschwitz, S., Leroux, V., Titov, K., & Zimmermann, E., 2012. An overview
23 of the spectral induced polarization method for near-surface applications, *Near Surface Geophysics*, **10**(6),
24 453–468.
- 25 Kohlrausch, R., 1854. Theorie des elektrischen Rückstandes in der Leidener Flasche, *Annalen der Physik*,
26 **167**(2), 179–214.
- 27 Kratzer, T. & Macnae, J., 2012. Induced polarization in airborne EM, *Geophysics*, **77**(5), E317–E327.
- 28 Li, Y. & Oldenburg, D., 1996. 3-D inversion of magnetic data, *Geophysics*, **61**(2), 394–408.
- 29 Li, Y. & Oldenburg, D. W., 2000. 3-D inversion of induced polarization data, *Geophysics*, **65**(6), 1931–1945.
- 30 Marchant, D., Haber, E., & Oldenburg, D. W., 2012. Inductive source induced polarization, *Geophysical
31 Journal International*, **192**(2), 602–612.
- 32 Marchant, D., Haber, E., & Oldenburg, D., 2013. Recovery of 3D IP distribution from airborne time-domain
33 EM, *ASEG Extended Abstracts*, **144**, 1–4.
- 34 Marchant, D., Haber, E., & Oldenburg, D., 2014. Three-dimensional modeling of IP effects in time-domain
35 electromagnetic data, *Geophysics*, **79**(6), E303–E314.
- 36 Nocedal, J. & Wright, S. J., 1999. *Numerical Optimization*, Springer, New York, NY.
- 37 Oldenburg, D. & Li, Y., 1994. Inversion of induced polarization data, *Geophysics*, **59**(9), 1327–1341.

1
2
3 *On recovering distributed IP information from inductive source time domain electromagnetic data* 25
4
5

- 1 Oldenburg, D. W. & Li, Y., 2005. 5. *Inversion for Applied Geophysics: A Tutorial*, chap. 5, pp. 89–150.
- 2 Pelton, W., Ward, S., Hallof, P., Sill, W., & Nelson, P., 1978. Mineral discrimination and removal of inductive
3 coupling with multifrequency IP, *Geophysics*, **43**(3), 588–609.
- 4 Routh, P. S. & Oldenburg, D. W., 2001. Electromagnetic coupling in frequency-domain induced polarization
5 data: a method for removal, *Geophysical Journal International*, **145**(1), 59–76.
- 6 Seigel, H., 1959. Matehmathical formulation and type curves for induced polarization, *Geophysics*, **24**(3),
7 547–565.
- 8 Seigel, H., 1974. The magnetic induced polarization (MIP) method, *Geophysics*, **39**(3), 321–339.
- 9 Smith, R. S. & Klein, J., 1996. A special circumstance of airborne inducedpolarization measurements, *Geo-
10 physics*, **61**(1), 66–73.
- 11 Smith, R. S., Walker, P., Polzer, B., & West, G. F., 1988. The time-domain electromagnetic response of
12 polarizable bodies: an approximate convolution algorithm, *Geophysical Prospecting*, **36**(April), 772–785.
- 13 Tarasov, A. & Titov, K., 2013. On the use of the Cole-Cole equations in spectral induced: Polarization,
14 *Geophysical Journal International*, **195**(1), 352–356.
- 15 Tikhonov, A. & Arsenin, V., 1977. *Solutions of Ill-Posed Problems*, W.H. Winston and Sons.
- 16 Weidelt, P., 1982. Response characteristics of coincident loop transient electromagnetic systems, **47**(Septem-
17 ber), 1325–1330.
- 18 Xu, Z. & Zhdanov, M., 2015. Three-Dimensional Cole-Cole Model Inversion of Induced Polarization Data
19 Based on Regularized Conjugate Gradient Method, *Geoscience and Remote Sensing Letters, IEEE*, **12**(6),
20 1180–1184.
- 21 Yee, K., 1966. Numerical solution of initial boundary value problems involving maxwell's equations in
22 isotropic media, *Antennas and Propagation, IEEE Transactions on*, **14**(3), 302–307.
- 23 Yuval & Oldenburg, D., 1997. Computation of Cole-Cole parameters from IP data, *Geophysics*, **62**(2), 436–
24 448.
- 41
42
43
44
45
46
47
48
49
50
51
52
53
54
55
56
57
58
59
60

1
2
3 26 *Seogi Kang and Douglas W. Oldenburg*
4
5
6
7
8

9 **Table 1.** Amplitudes of decomposed IP currents at two marked points (white stars) shown in Fig. 9(b). Units in
10 A/m^2
11
12
13

Division	$ \vec{j}^{IP} $	$ \vec{j}^{pol} $	$ - \sigma_\infty \vec{\nabla} \phi^{IP} $	$ - \sigma_\infty \vec{d}^{IP} $
Left	1.5×10^{-10}	2.5×10^{-10}	7.6×10^{-11}	1.9×10^{-12}
Right	5.4×10^{-11}	1.2×10^{-10}	3.5×10^{-11}	3.3×10^{-11}

14
15
16
17
18
19
20
21
22
23
24
25
26
27
28
29
30
31
32
33
34
35
36
37
38
39
40
41
42
43
44
45
46
47
48
49
50
51
52
53
54
55
56
57
58
59
60

On recovering distributed IP information from inductive source time domain electromagnetic data 27

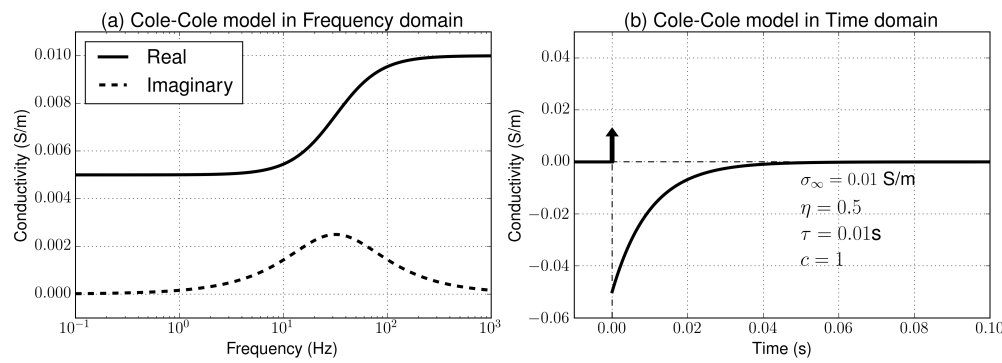


Figure 1. Cole-Cole response in frequency domain (a) and time (b) domain. The Cole-Cole parameters are $\sigma_\infty = 10^{-2} \text{ S/m}$, $\eta = 0.5$, $\tau = 0.01$, and $c=1$. The arrow shown in Fig. 1(b) indicates a delta function ($\sigma_\infty \delta(t)$).

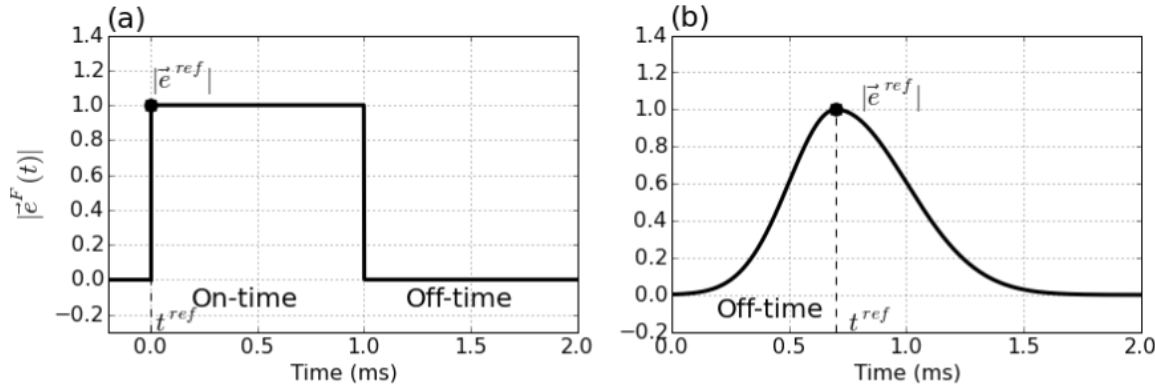


Figure 2. Conceptual diagram for the amplitude of the fundamental electric fields. (a) EIP and (b) ISIP cases.

28 Seogi Kang and Douglas W. Oldenburg

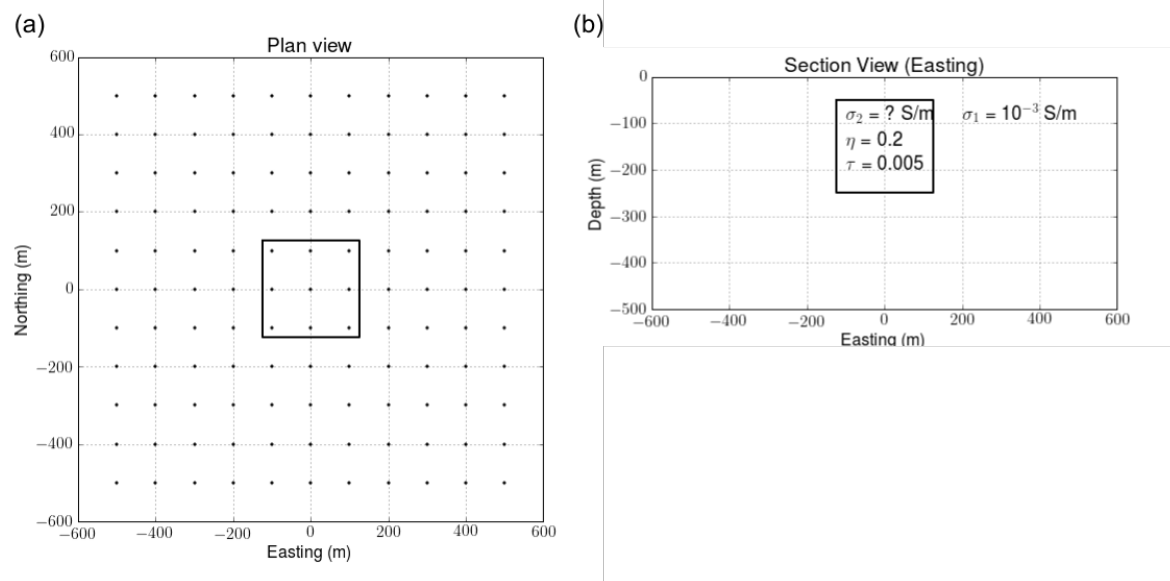


Figure 3. Plan (a) and section b) views of the IP model. The solid line in (a) delineates the boundary of the IP body. Solid circles in (a) denote the sounding locations. In (b) the conductivity σ_2 is variable so that canonical, conductive and resistive blocks can be examined

On recovering distributed IP information from inductive source time domain electromagnetic data 29

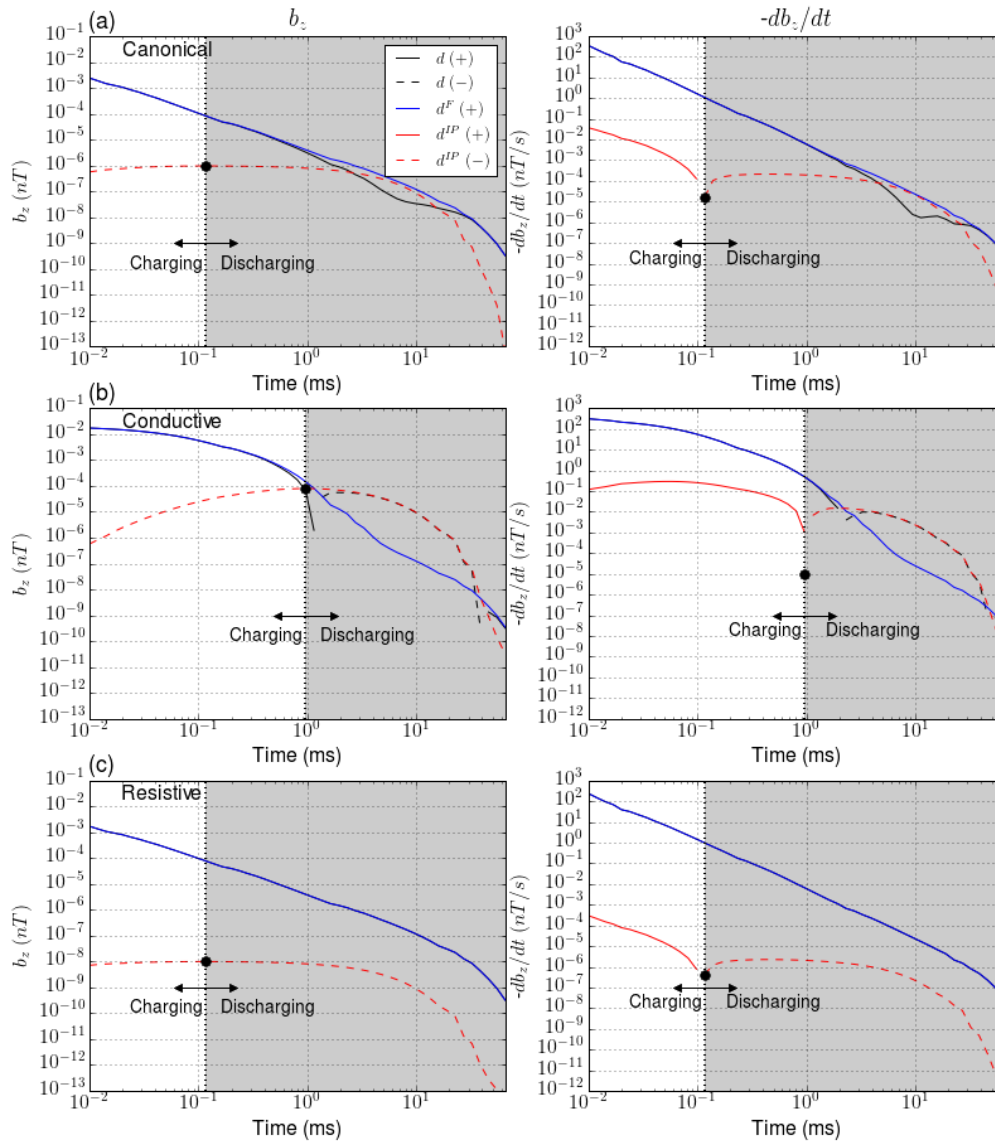


Figure 4. Time decaying curves of the observations (d ; black line), fundamental (d^F ; blue line) and IP (d^{IP} ; red line) responses. All three cases: (a) canonical, (b) conductive and (c) resistive are presented. Right and left panels show b_z and $-\frac{\partial b_z}{\partial t}$. The vertical black dotted line indicates the time at which the polarization field reaches its maximum value. The flight height of the collocated transmitting and receiving loop is 30 m above the surface.

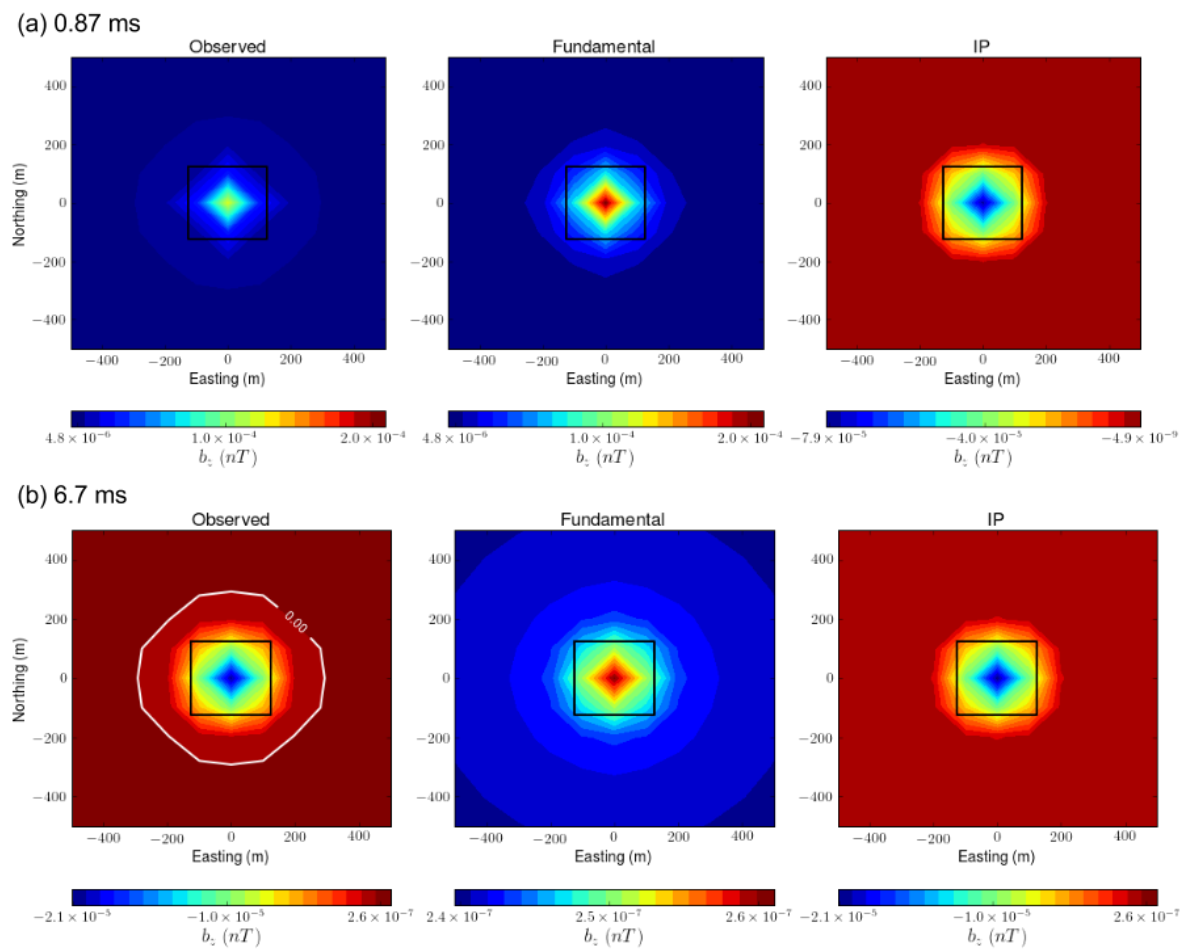
30 *Seogi Kang and Douglas W. Oldenburg*

Figure 5. Interpolated maps of observed (left panel), fundamental (middle panel) and IP (right panel) responses. Two time channels at (a) 0.86 ms and (b) 6.7 ms are presented. White line contours a zero-crossing in the observed response.

1
2
3
4
5
6
7
8
9
10
11
12
13
14
15
16
17
18
19
20
21
22
23
24
25
26
27
28
29
30
31
32
33
34
35
36
37
38
39
40
41
42
43
44
45
46
47
48
49
50
51
52
53
54
55
56
57
58
59
60
On recovering distributed IP information from inductive source time domain electromagnetic data 31

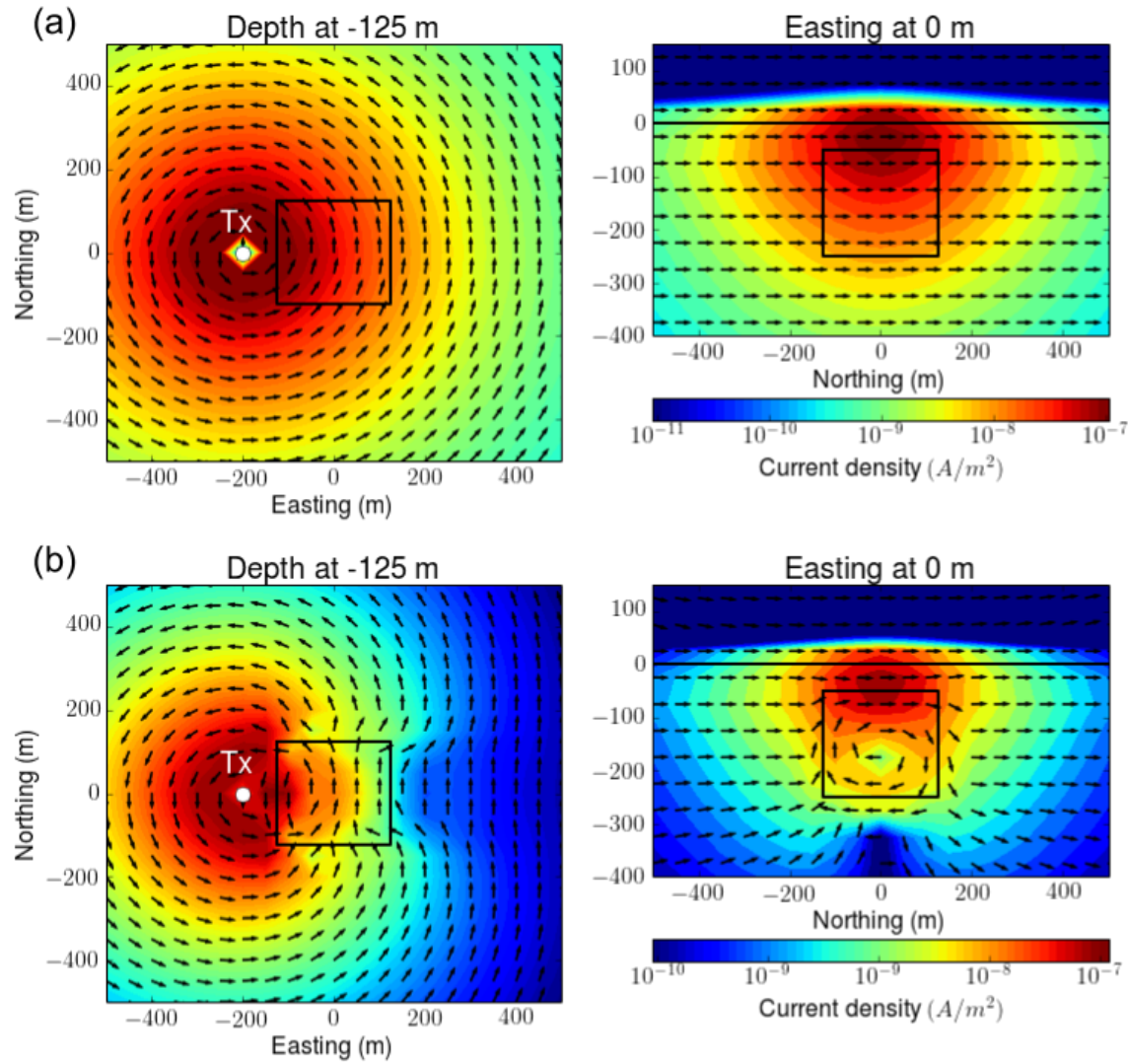


Figure 6. Maps of reference currents: (a) canonical and (b) conductive models. Left and right panels show plan and section views at -125 m-depth and 0 m-easting, respectively. A transmitter is located at (-200 m, 0 m, 30 m). Black arrows and colored background respectively indicate the direction and amplitude of the current. The black solid line outlines the boundary of chargeable body.

32 Seogi Kang and Douglas W. Oldenburg

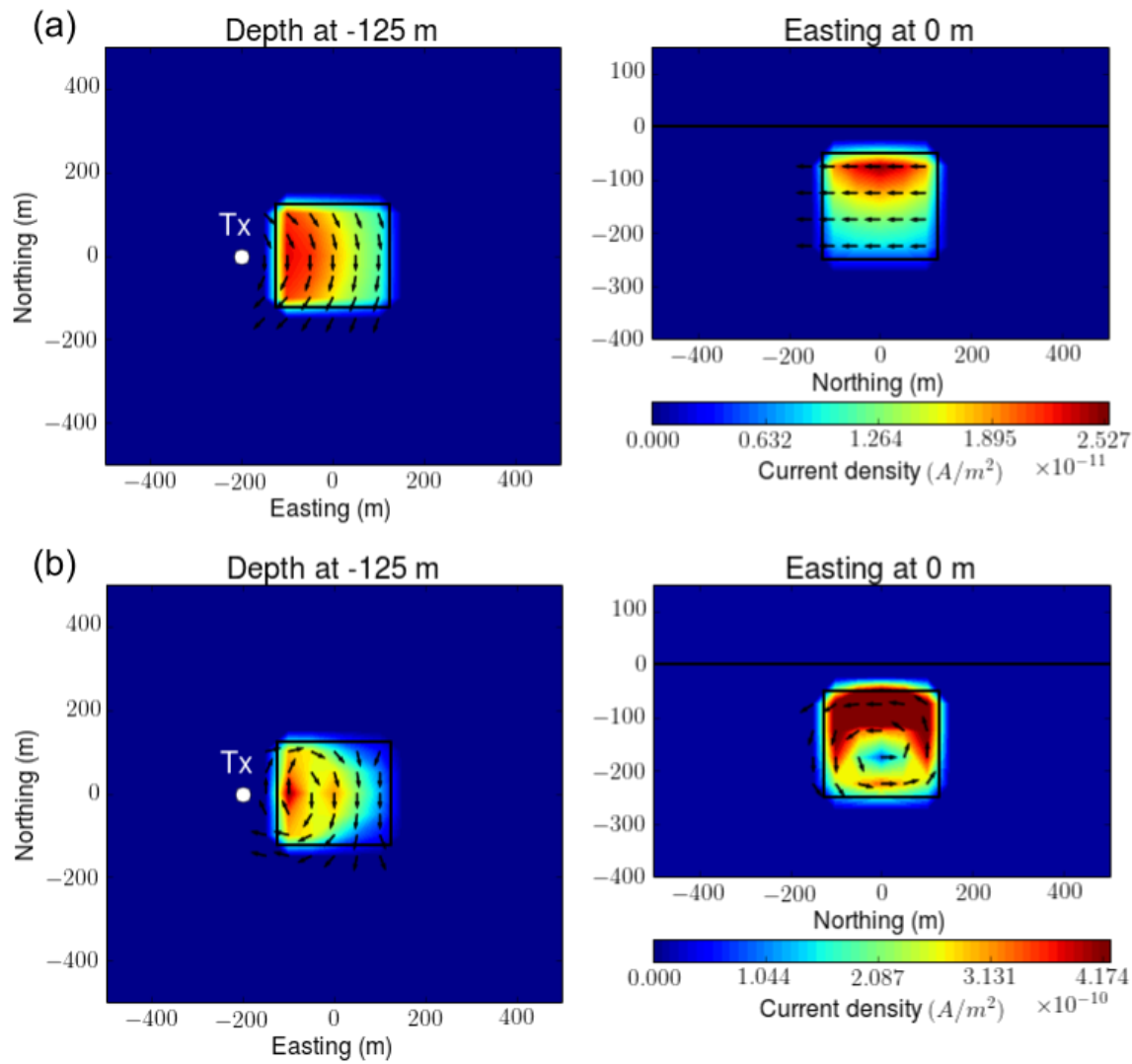


Figure 7. Maps of polarization currents: (a) canonical and (b) conductive models at 0.86 ms. Left and right panels show plan and section views at -125 m-depth and 0 m-easting, respectively. A transmitter is located at (-200 m, 0 m, 30 m). Black arrows and shaded values respectively indicate the direction and amplitude of the current. Black solid outlines boundary of the surface or the chargeable body.

1
2
3
4
5
6
7
8
9
10
11
12
13
14
15
16
17
18
19
20
21
22
On recovering distributed IP information from inductive source time domain electromagnetic data 33
23
24
25
26
27
28
29
30
31
32
33
34
35
36
37
38
39
40
41
42
43
44
45
46
47
48
49
50
51
52
53
54
55
56
57
58
59
60

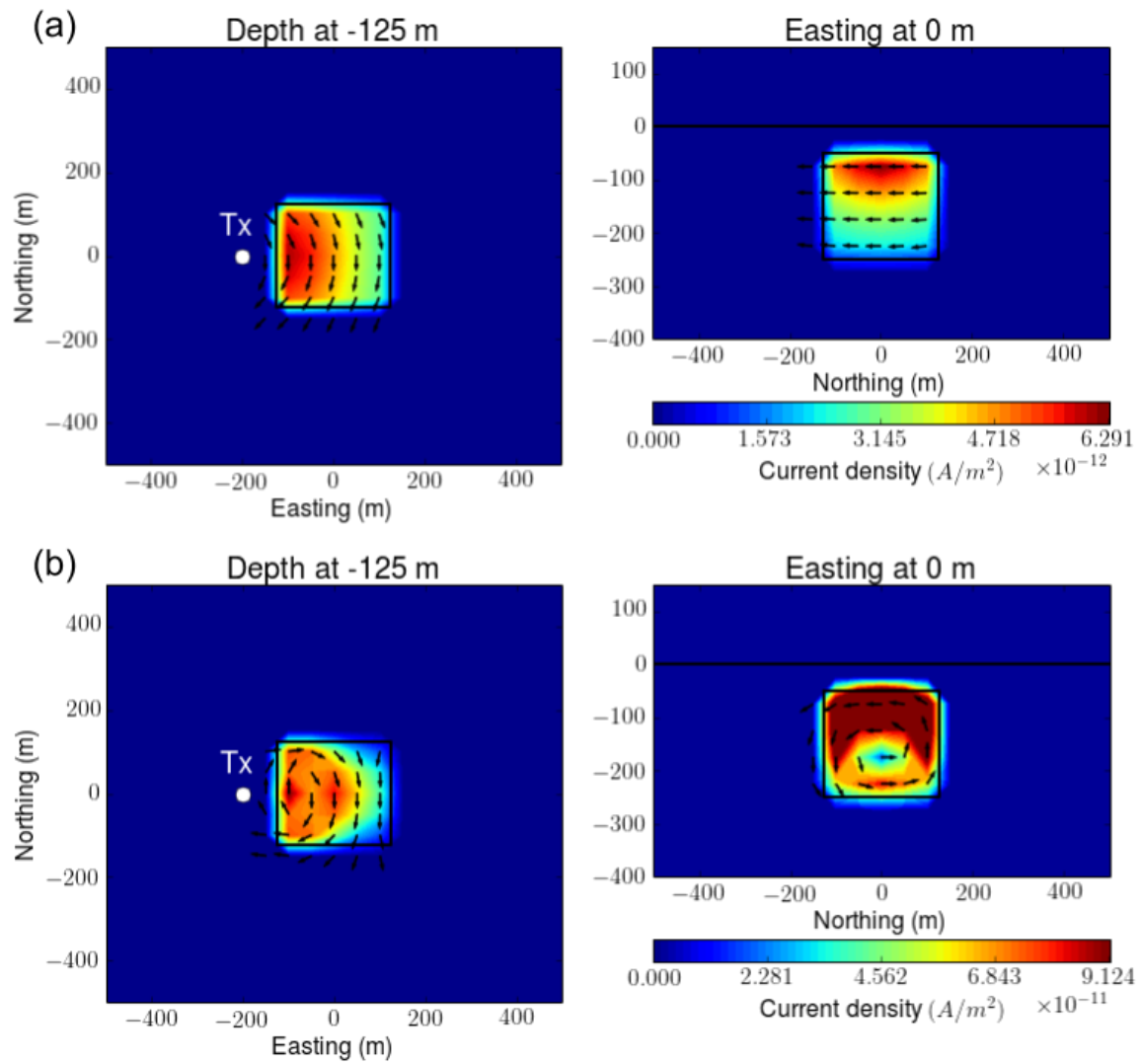


Figure 8. Maps of polarization currents: (a) canonical and (b) conductive models at 6.7 ms. Left and right panels show plan and section views at -125 m-depth and 0 m-easting, respectively. A transmitter is located at (-200 m, 0 m, 30 m). Black arrows and shaded values indicate the direction and amplitude of the current, respectively. Black solid outlines boundary of the surface or the chargeable body.

34 Seogi Kang and Douglas W. Oldenburg

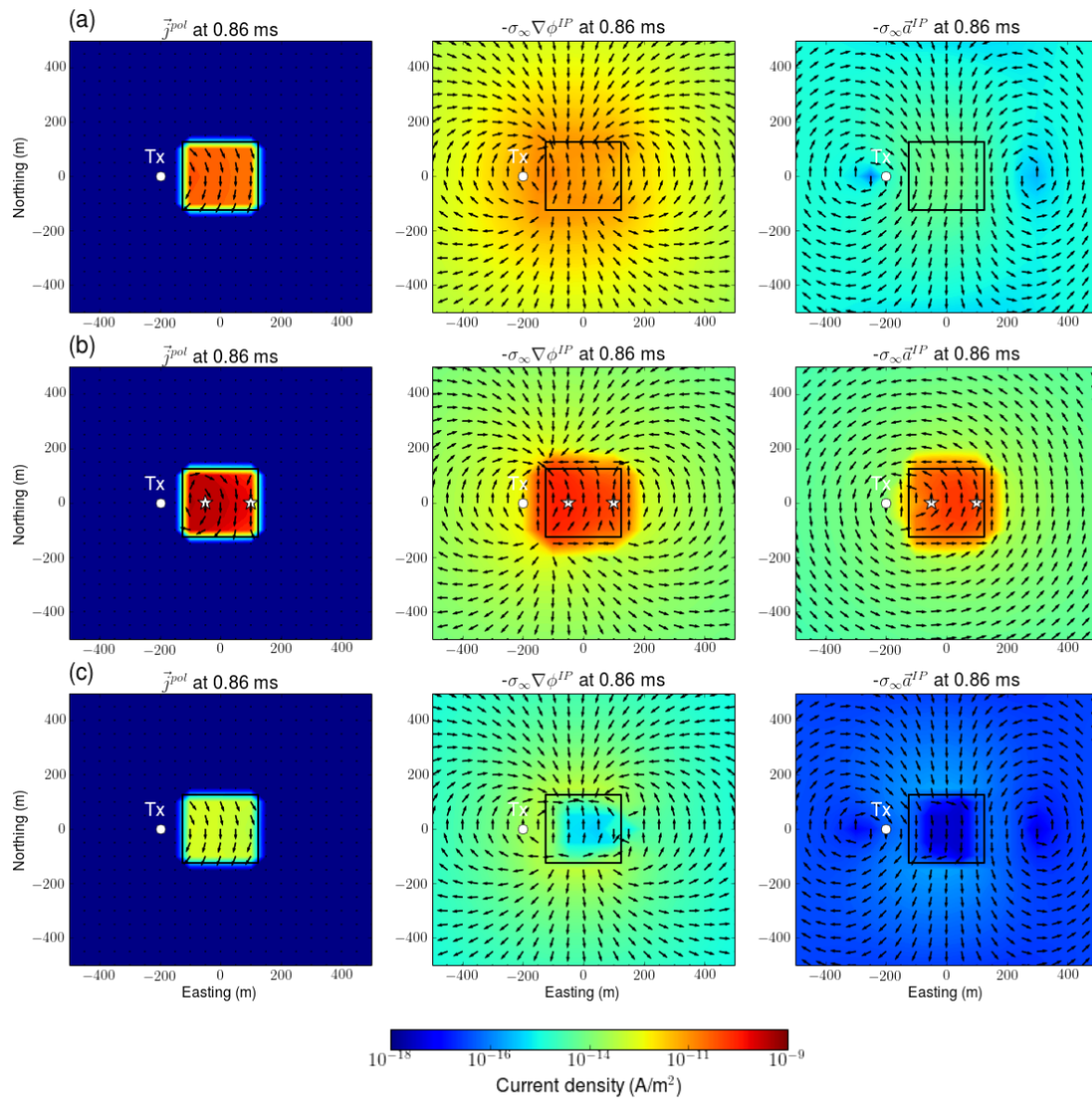


Figure 9. Decomposition of the IP currents as \vec{j}^{pol} (left panel), $-\sigma_\infty \nabla \phi^{IP}$ (middle panel), and $-\sigma_\infty \vec{a}^{IP}$ (right panel) at 0.86 ms. Plan view maps of the currents at -125 m-depth are shown: (a) canonical, (b) conductive, and (c) resistive cases.

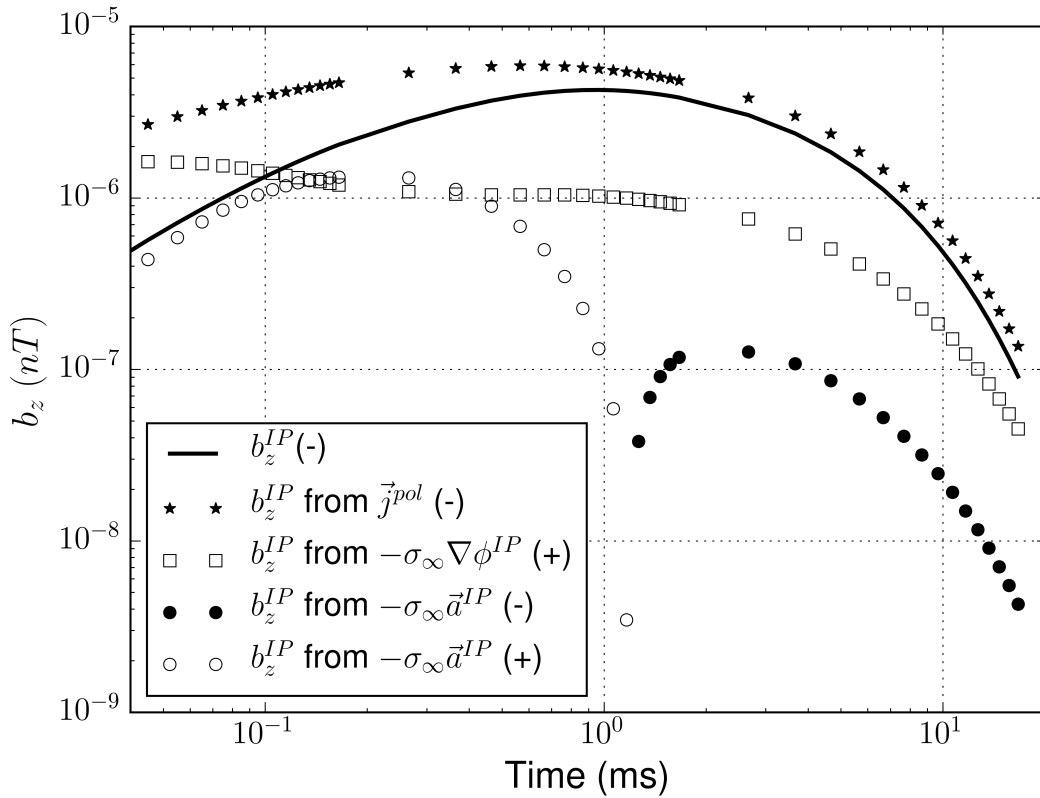


Figure 10. Comparisons of contributions of \vec{j}^{pol} , $-\sigma_{\infty} \vec{\nabla} \phi^{IP}$, and $-\sigma_{\infty} \vec{a}^{IP}$ to the observed IP responses. Solid line indicates true b_z^{IP} responses. Stars, rectangles, and circles correspondingly indicate each IP response generated by applying Biot-Savart law to \vec{j}^{pol} , $-\sigma_{\infty} \vec{\nabla} \phi^{IP}$, and $-\sigma_{\infty} \vec{a}^{IP}$. Empty and solid markers represent positive and negative values, respectively.

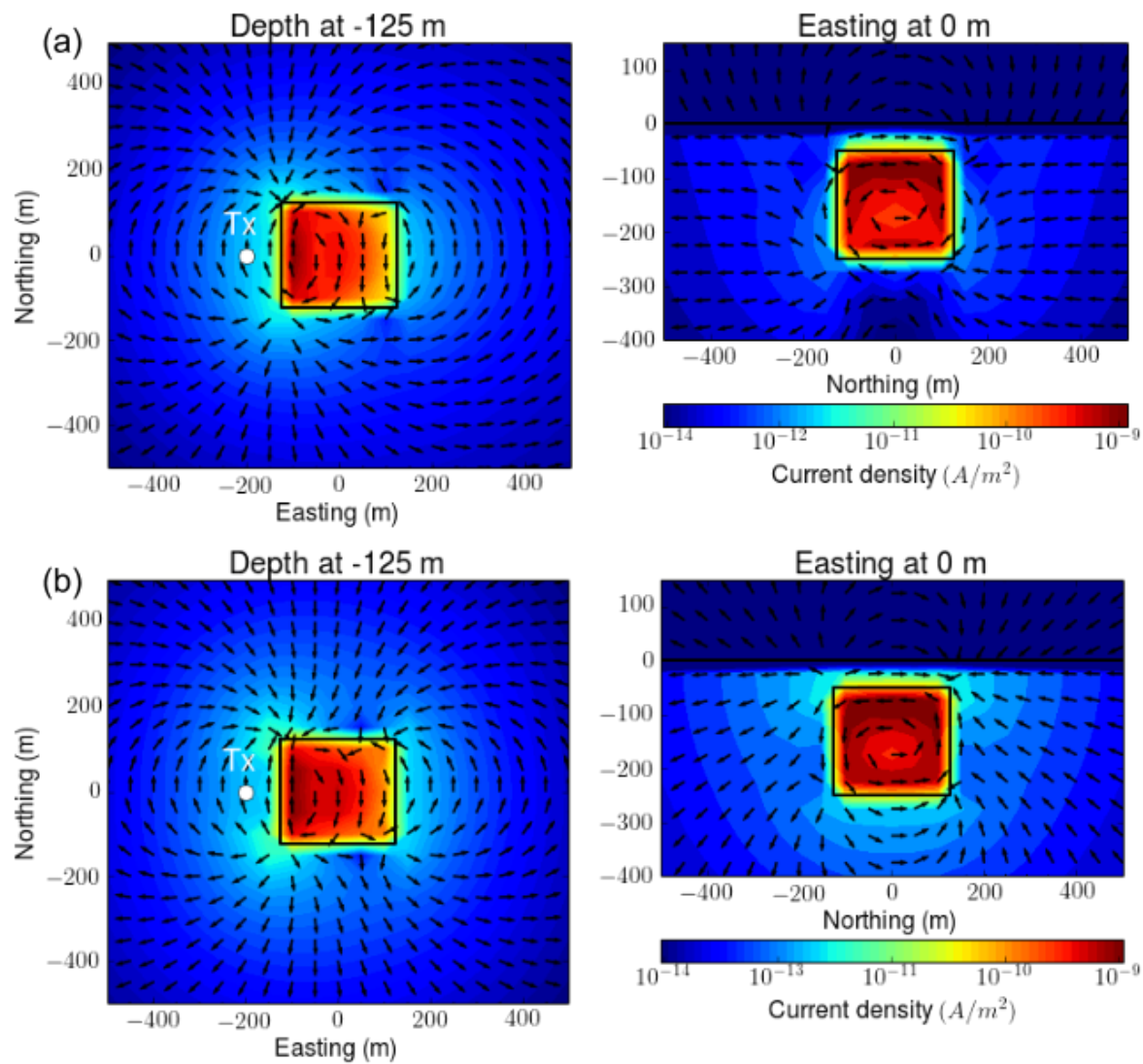
36 *Seogi Kang and Douglas W. Oldenburg*

Figure 11. Interpolated maps of (a) true and (b) approximate IP currents at 0.86 ms. Left and right columns respectively show plan and section view maps at -125 m-depth and 0 m-easting.

1
2
3
4
5
6
7
8
9
10
11
12
13
14
15
16
17
18
19
20
21
22
23
24
25
26
27
28
29
30
31
32
33
34
35
36
37
38
39
40
41
42
43
44
45
46
47
48
49
50
51
52
53
54
55
56
57
58
59
60

On recovering distributed IP information from inductive source time domain electromagnetic data 37

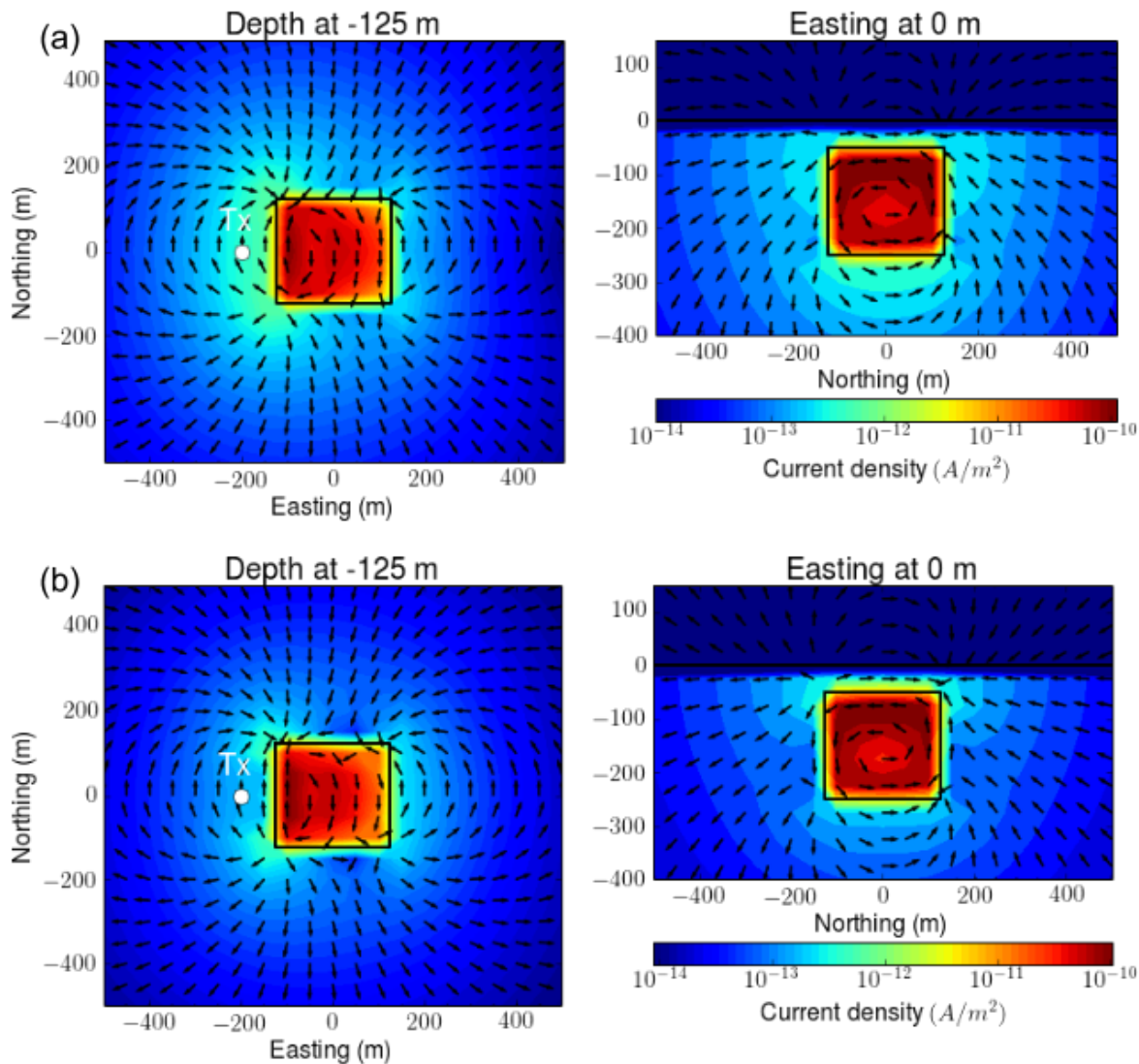


Figure 12. Interpolated maps of (a) true and (b) approximate IP currents at 6.7 ms. Left and right columns respectively show plan and section view maps at -125 m-depth and 0 m-easting.

38 Seogi Kang and Douglas W. Oldenburg

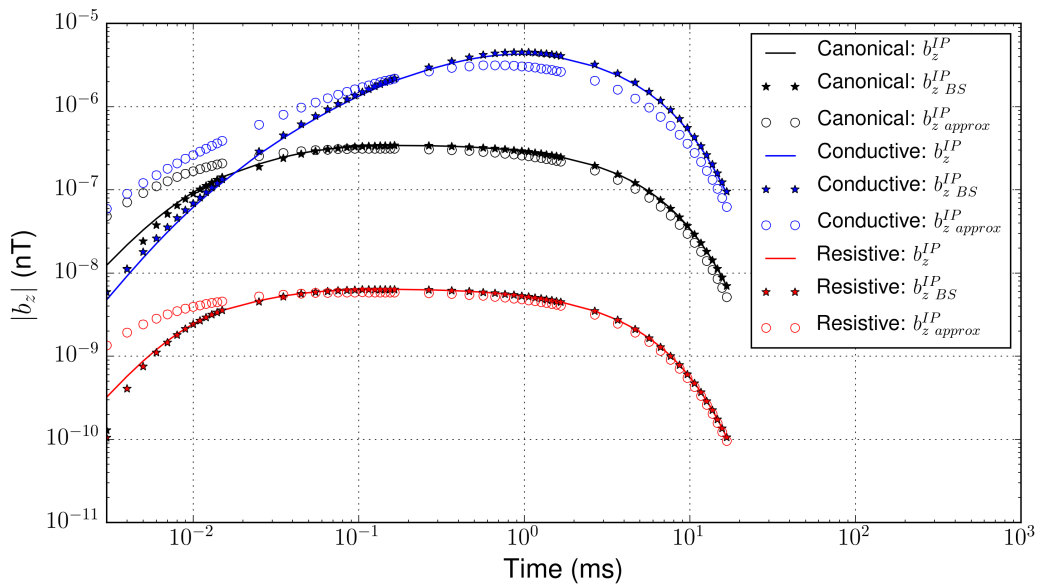


Figure 13. Comparison of true and approximate IP responses (b_z^{IP}). Black, blue, and red colors respectively indicate canonical, conductive, and resistive cases. Solid lines indicate true b_z^{IP} computed by subtracting the fundamental response from the observation. The stars are the application of Biot-Savart to true IP current and generate $b_z^{IP,BS}$. Empty circles show our approximate $b_z^{IP,approx}$ response.

On recovering distributed IP information from inductive source time domain electromagnetic data 39

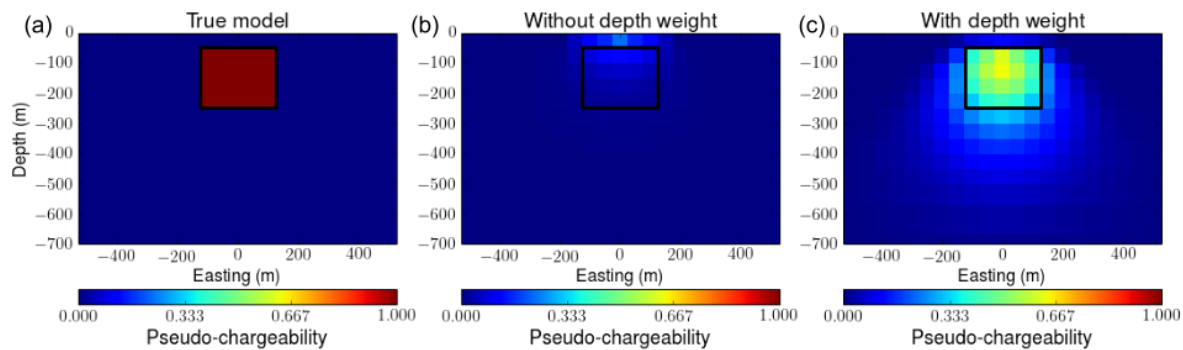


Figure 14. Effect of depth weighting in 3D IP inversion. (a) True pseudo-chargeability model on vertical section at 0 m-northing. Recovered pseudo-chargeability models (b) without depth weighting and (c) with depth weighting.

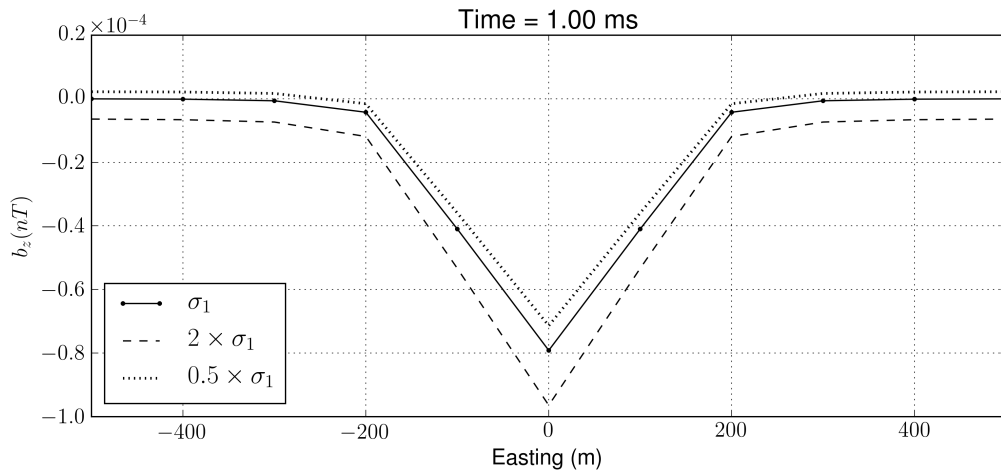


Figure 15. IP responses on a profile line at 0 m-northing. IP responses are computed from perturbed σ_∞ models. Halfspace conductivity (σ_1) is perturbed two times higher or less resulting in overestimated (dotted line) and underestimated (dashed line) IP responses. Solid line shows the true IP response.

40 Seogi Kang and Douglas W. Oldenburg

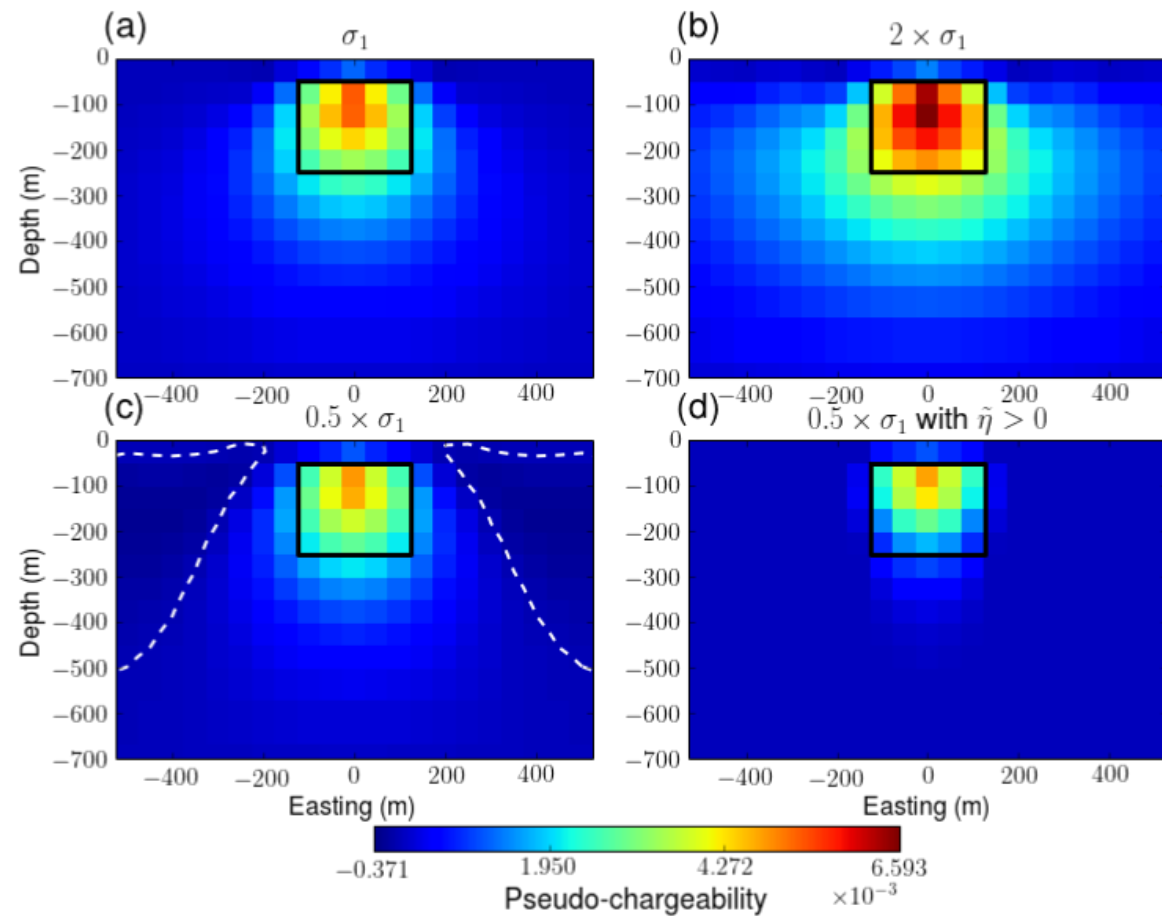


Figure 16. Recovered pseudo-chargeability sections from 3D IP inversions at 0 m-northing. (a) d^{IP} with true σ_1 . (b) d^{IP} with $2 \times \sigma_1$. (c) d^{IP} with $0.5 \times \sigma_1$. (d) d^{IP} with $0.5 \times \sigma_1$ and the positivity constraint on the pseudo-chargeability. White dashed lines contour zero-crossing lines.

1
2
3
4
5
6
7
8
9
10
11
12
13
14
15
16
17
18
19
20
21
22
23
24
25
26
27
28
29
30
31
32
33
34
35
36
37
38
39
40
41
42
43
44
45
46
47
48
49
50
51
52
53
54
55
56
57
58
59
60

On recovering distributed IP information from inductive source time domain electromagnetic data 41

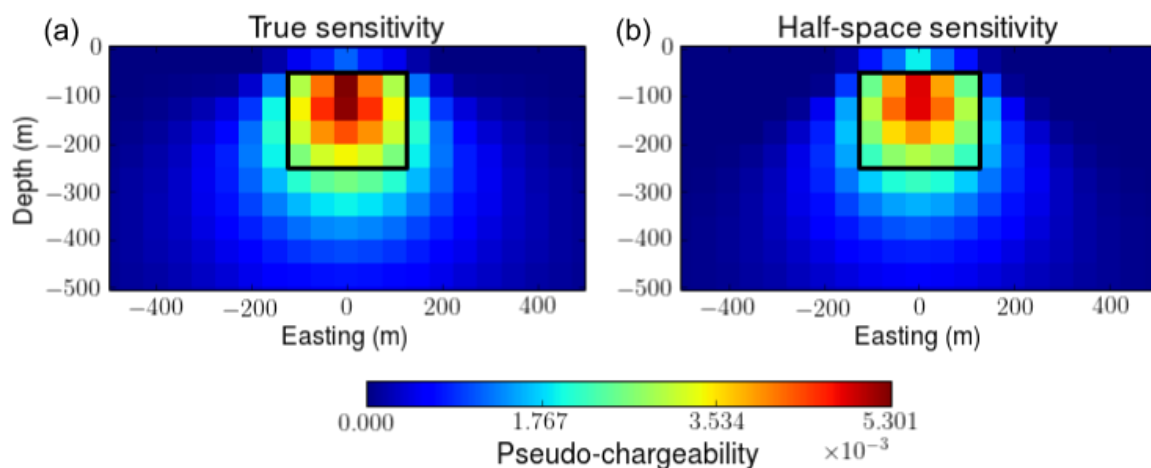


Figure 17. Recovered pseudo-chargeability sections from the 3D IP inversions at 0 m-northing. (a) True and (b) incorrect σ_∞ is used to compute sensitivity function. For the incorrect sensitivity we used a halfspace conductivity σ_1 .

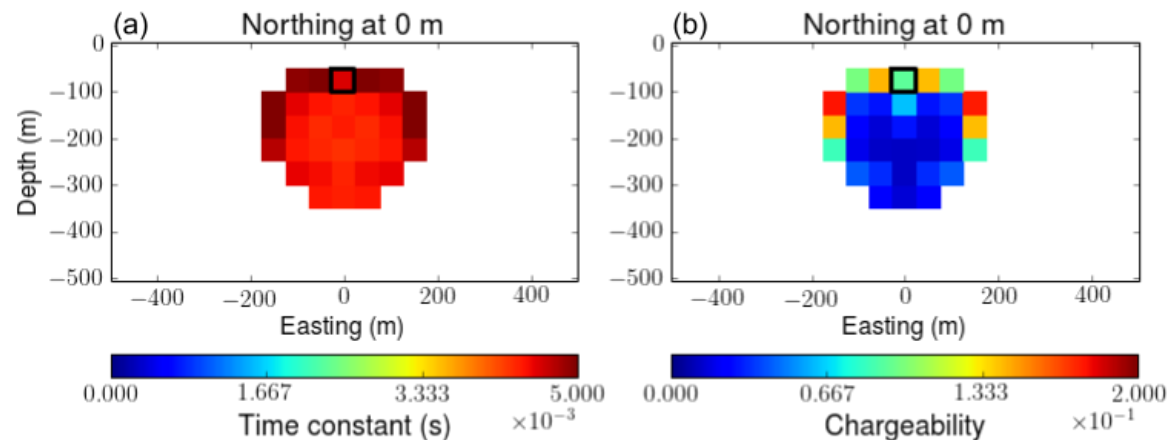


Figure 18. Section views of recovered: (a) time constant and (b) chargeability. Any region where the pseudo-chargeability shown in Fig. 17a is smaller than 0.001 is ignored in this analysis, and blanked.

42 Seogi Kang and Douglas W. Oldenburg

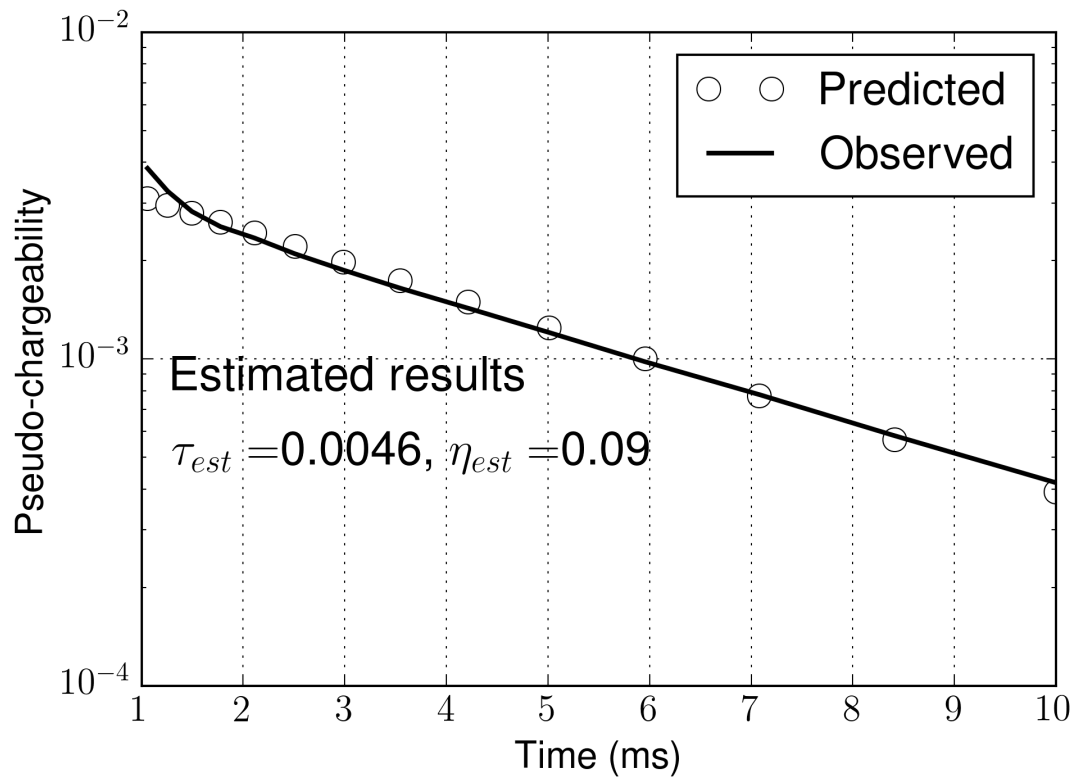


Figure 19. Comparisons of the observed and predicted pseudo-chargeability at a single pixel in a chargeable body. The empty circles and solid line respectively indicate predicted and observed pseudo-chargeability. The estimated time constant and chargeability are respectively expressed as τ_{est} and η_{est} . The true values for τ and η are respectively 0.005 and 0.2.

1
2
3 *On recovering distributed IP information from inductive source time domain electromagnetic data* 43
4
5

6 **APPENDIX A: EFFECTIVE PSEUDO-CHARGEABILITY**
7
8

9 **A1 Handling multiple transmitters in ATEM surveys**
10

11 The work for inductive sources in the main section of the paper has been developed for a single
12 transmitter and 3D information about chargeability can be obtained if there are multiple receivers. For
13 ATEM data however, we have only a single receiver location for each transmitter but we have multiple
14 transmitter locations. Our goal is to alter the problem to work with an effective pseudo-chargeability.
15
16

17 In our linearized eq. (39), each transmitter has its own sensitivity and pseudo-chargeability. For our
18 airborne case the sensitivity for the k -th transmitter is the k -th row of \mathbf{J} and the pseudo-chargeability
19 is $\tilde{\eta}^k$. The corresponding IP datum is
20

$$22 \quad d_k^{IP}(t) = \sum_{i=1}^{nC} J_{k,i} \tilde{\eta}_i^k(t), \quad k = 1, \dots, nTx, \quad (A.1)$$

23 where nTx is the number of transmitters, nC is the number of cells in the domain, and $J_{k,i}$ indicates
24 an element of the Jacobian matrix for the k -th transmitter and the i -th cell. We want to replace $\tilde{\eta}_i^k$ with
25 a single effective pseudo-chargeability $\tilde{\eta}_i$ and therefore write the IP datum as
26
27

$$28 \quad d_k^{IP}(t) = \sum_{i=1}^{nC} J_{k,i} \tilde{\eta}_i(t), \quad k = 1, \dots, nTx, \quad (A.2)$$

29 The waveforms are different for each transmitter and hence this representation cannot be exact. To
30 examine the implications of this it suffices to look at the contribution of any volumetric pixel. Each
31 pixel contributes to all of the IP data but in differing amounts. The total contribution of the i -th pixel
32 to the nTx data set at a single time is
33
34

$$35 \quad q_i = \sum_{k=1}^{nTx} J_{k,i} \tilde{\eta}_i^k(t), \quad i = 1, \dots, nC. \quad (A.3)$$

36 Our goal is to find an effective chargeability that produces the same net effect on the measured data.
37
38 We search for a transmitter-independent $\tilde{\eta}_i$ such that
39

$$40 \quad q_i^{est} = \sum_{k=1}^{nTx} J_{k,i} \tilde{\eta}_i(t), \quad i = 1, \dots, nC. \quad (A.4)$$

41 Minimizing the least squares difference between eqs (A.3) and (A.4) yields
42
43

$$44 \quad \tilde{\eta}_i(t) = \frac{\sum_{k=1}^{nTx} J_{k,i}^2 \tilde{\eta}_i^k(t)}{\sum_{k=1}^{nTx} J_{k,i}^2} = \sum_{k=1}^{nTx} a_i^k \tilde{\eta}_i^k(t), \quad i = 1, \dots, nC. \quad (A.5)$$

45 where the normalized weight (p_i^k) is
46
47

$$48 \quad p_i^k = \frac{J_{k,i}^2}{\sum_{k=1}^{nTx} J_{k,i}^2}, \quad i = 1, \dots, nC. \quad (A.6)$$

44 *Seogi Kang and Douglas W. Oldenburg*

With the above understanding about how $\tilde{\eta}_i$ relates to the $\tilde{\eta}_i^k$ from each transmitter we can proceed

as follows. Firstly, from eq. (28) we have

$$\tilde{\eta}_i^k(t) = \tilde{\eta}^I \otimes \hat{w}_i^k(t) \quad (\text{A.7})$$

Substituting eqs (A.7) into (A.5) allows us to write

$$\tilde{\eta}_i(t) = \tilde{\eta}^I(t) \otimes w_i^e(t), \quad (\text{A.8})$$

where we define the effective time history of the electric field, $w_i^e(t)$ as

$$w_i^e(t) = \sum_{k=1}^{nTx} a_i^k \hat{w}_i^k(t), \quad i = 1, \dots, nC. \quad (\text{A.9})$$

The above equations shows that the pseudo-chargeability for any pixel recovered from the inversion is equal to the convolution of the impulse pseudo-chargeability, $\tilde{\eta}^I(t)$, with an effective time history of the electric field $w^e(t)$. Although it is somewhat involved, the $w^e(t)$ associated with each pixel can be evaluated by knowing the electric fields associated with the fundamental EM problem. Ultimately this allows us to estimate the parameters associated with the impulse pseudo-chargeability in the same manner as outlined for the case with a single transmitter. Our ability to evaluate the $w^e(t)$ and test the validity of eq. (A.2) is treated in Section A2.

A2 Effective pseudo-chargeability for ATEM data

In Appendix A1 we showed how to define an effective chargeability when we have multi-transmitters.

For each pixel we have equation:

$$\tilde{\eta}_i(t) = \tilde{\eta}_i^I(t) \otimes w_i^e(t), \quad (\text{A.10})$$

where $\tilde{\eta}_i^I(t)$ is the impulse pseudo-chargeability associated with an individual pixel. The effective time history of the electric field, $w_i^e(t)$ is a linear combination of the fundamental electric fields due to the individual transmitters. We can calculate $w_i^e(t)$ and carry out the convolution to evaluate the effective pseudo-chargeability. The IP data can then be forward modelled using eq. (39). This allows us to validate eq. (A.2), which demonstrated linear form of d^{IP} data at all transmitter locations, by comparing results with the true IP data obtained via forward modelling. It is only necessary to apply this to the conductive model.

The evaluation of the effective pseudo-chargeability is carried out on a cell by cell basis. For each

cell we first evaluate $w^e(t)$ (eq. A.9). This requires calculating normalized weights shown in eq. (A.6).

Fig. A1 shows these weights at a single pixel located at (0 m, 0 m, -75 m). These decay away from

the center pixel because of the decay of the sensitivity functions. Because those are weights used

to compute $w^e(t)$, we could expect that the computed $w^e(t)$ will be mostly affected by \hat{w}_k from a

1
2
3
4 *On recovering distributed IP information from inductive source time domain electromagnetic data* 455
6 few stations close to the center. In Fig. A2, we provide both \hat{w}_k (dashed lines) from all transmitter
7
8 locations and $w^e(t)$ (solid line) averaged by them. The $w^e(t)$ is dominantly affected by the $\hat{w}(t)$ at the
9 center transmitter location (solid circles). Considering that the transmitters are 50 m apart, the decay
10 of the sensitivity from center transmitter location to others is substantial ($\sim 1/r^3$). This results in the
11 greatest normalized weight at the center transmitter location, and the observed result about $w^e(t)$ is
12 caused by this. $w^e(t)$ is convolved with $\tilde{\eta}^I(t)$ to compute the effective $\tilde{\eta}(t)$ for that cell. When this is
13 carried out for each cell then the approximate IP responses can be computed using eq. (39). These can
14 be compared with the true IP responses. Fig. A3 shows the comparisons at 0.86 ms. The images are
15 nearly identical in shape but the approximate IP responses are nearly a factor of two lower than the
16 true values. This is not entirely unexpected. A similar effect was observed for IP responses for a single
17 transmitter shown in Fig. 13. At 0.86 ms, the approximate value was about 70 percent of the true d^{IP} .
18 These results seem to be a worst case scenario. The discrepancy for a conductive body lessens as time
19 increases and analyses for the canonical and resistive bodies shows that the approximate and true IP
20 data are in very good agreement.
21
22
23
24
25
26
27
28
29
30
3132 **APPENDIX B: EXTRACTING INTRINSIC IP PARAMETERS**33 The output of our IP inversion is a 3D distribution of the pseudo-chargeability at multiple time chan-
34 nels. As its name suggests, pseudo-chargeability is not an intrinsic IP parameter like chargeability, but
35 it is a convoluted property between $\tilde{\eta}^I(t)$ and $\hat{w}(t)$:
36
37

38
39
$$\tilde{\eta}(t) = \tilde{\eta}^I(t) \otimes \hat{w}(t), \quad (B.1)$$

40
41

42 with the definition of impulse pseudo-chargeability (eq. 4). We now use the $\tilde{\eta}(t)$ as the data and recover
43 intrinsic parameters such as η, τ, c in a Cole-Cole model. Assuming a Debye model ($c=1$), we obtain
44
45

46
47
$$\tilde{\eta}^I(t) = \frac{\eta}{(1-\eta)\tau} e^{-\frac{t}{(1-\eta)\tau}}, \quad (B.2)$$

48
49

50 Since we have σ_∞ we can compute $\hat{w}(t)$, which is the time history of the electric field. Accord-
51 ingly, we can unravel the recovered pseudo-chargeability to extract intrinsic IP parameters such as
52 chargeability(η) and time constant (τ). We use a gradient-based optimization and thus we need the
53 sensitivity function for the pseudo-chargeability (eq. B.1) with respect to η and τ . To simplify this
54 procedure, we rewrite impulse pseudo-chargeability as
55
56

57
58
$$\tilde{\eta}^I(t) = a e^{-bt}, \quad (B.3)$$

59
60

61 where $a = \frac{\eta}{(1-\eta)\tau}$ and $b = \frac{1}{(1-\eta)\tau}$. Then we take the derivative of $\tilde{\eta}(t)$ with regard to a and b :

62
63
$$\frac{\partial \tilde{\eta}(t)}{\partial a} = e^{-bt} \otimes \hat{w}(t), \quad (B.4)$$

64
65

46 Seogi Kang and Douglas W. Oldenburg

$$\frac{\partial \tilde{\eta}(t)}{\partial b} = -ate^{-bt} \otimes \hat{w}(t). \quad (\text{B.5})$$

1 With these sensitivity functions, we can set up an inverse problem, and recover a and b . The charge-
2 ability and time constant can be obtained from a and b :

$$\eta = \frac{a}{b}, \quad (\text{B.6})$$

$$\tau = \frac{1}{(1 - a/b)b}. \quad (\text{B.7})$$

4 We apply this inversion separately to each cell in the recovered pseudo-chargeability in a manner
5 similar to (Yuval & Oldenburg 1997). For the better alternative (representation) of time-dependent
6 conductivity, a different parameterization such as stretched-exponential (Kohlrausch 1854) or Cole-
7 Cole model with variable c can be implemented.

APPENDIX C: DISCRETIZATIONS

C1 Steady-state Maxwell's equations

As shown in eq. (33), computation of our linearized kernel requires solving steady-state Maxwell's equations. We discretize this system using a mimetic finite volume (FV) method with weak formulation (Yee 1966; Haber 2014). For the discretization, we assume that the electric field \vec{e} is discretized by a grid function e on cell edges and the magnetic flux density \vec{b} is discretized by a grid function b on cell faces. The electrical potential ϕ is discretized by a grid function ϕ on the cell nodes. For a clear representation of the derivation, recall Maxwell's equations in steady state are

$$\vec{j} = \sigma_\infty \vec{e} = -\sigma_\infty \vec{\nabla} \phi, \quad (\text{C.1})$$

$$-\nabla \cdot \vec{j} = \nabla \cdot \vec{j}_s, \quad (\text{C.2})$$

$$\vec{j}|_{\partial\Omega} \cdot \hat{n} = 0, \quad (\text{C.3})$$

where $\partial\Omega$ indicates boundary surface of the system and \hat{n} is the normal vector of the boundary surface.

The weak form of those equations can be written as

$$(\vec{j}, \vec{w}) + (\sigma_\infty \vec{\nabla} \phi, \vec{w}) = 0, \quad (\text{C.4})$$

$$-(\vec{j}, \vec{\nabla} \psi) = (\vec{j}_s, \vec{\nabla} \psi). \quad (\text{C.5})$$

10 The inner products (\vec{j}, \vec{w}) , $(\sigma_\infty \vec{\nabla} \phi, \vec{w})$, $(\vec{j}, \vec{\nabla} \psi)$ and $(\vec{j}_s, \vec{\nabla} \psi)$ are edge-based products. Here we define
11 the inner product as

$$(\vec{a}, \vec{b}) = \int_{\Omega} \vec{a} \cdot \vec{b} dv, \quad (\text{C.6})$$

1
2
3 *On recovering distributed IP information from inductive source time domain electromagnetic data* 47
4
5

6 1 where Ω is the volume of the system. By discretizing the $\vec{\nabla}$ operator and the inner product in space,
7 2 we obtain
8
9

$$10 \quad \mathbf{M}^e \mathbf{j} + \mathbf{M}_{\sigma_\infty}^e \mathbf{G} \phi = 0, \quad (\text{C.7})$$

$$11 \quad 12 \quad -\mathbf{G}^T \mathbf{M}^e \mathbf{j} = \mathbf{G}^T \mathbf{M}^e \mathbf{j}_s, \quad (\text{C.8})$$

13
14 4 where \mathbf{M}^e performs volume averaging, and $\mathbf{M}_{\sigma_\infty}^e$ is the mass matrix of conductivity (σ_∞), which
15
16 5 discretizes the edge based inner product. For further details on the formation of this matrix see Haber
17
18 6 (2014).

19 7 By substituting eq. (C.7) into (C.8), we have
20
21

$$22 \quad \mathbf{A}_{\sigma_\infty} \phi = \mathbf{rhs}^{DC}, \quad (\text{C.9})$$

23
24 8 where $\mathbf{A}_{\sigma_\infty} = \mathbf{G}^T \mathbf{M}_{\sigma_\infty}^e \mathbf{G}$ and $\mathbf{rhs}^{DC} = \mathbf{G}^T \mathbf{M}^e \mathbf{j}_s$. We use SIMPEG's tensor mesh and solver
25
26 9 classes to form and solve above linear system (Cockett et al. 2015).

29 10 C2 Linearized kernel for IP responses

31
32 11 To obtain a linear form of eq. (39), we first discretize the Biot-Savart law shown in eqs (37) and (38).
33
34 12 In our discretization \vec{j}^{IP} and $\tilde{\eta}$ are defined at the cell centers, and those for each time channel are
35
36 13 constant in a cell volume, whereas \vec{e}^{ref} is defined on the cell edges. We define the number of cells
37
38 14 and edges in 3D space as nC and nE , respectively. The discretized IP current density, $\mathbf{j}_{cc}^{IP} \in \mathbb{R}_1^{3nC}$, is
39
40 15 defined at the cell center. Since \vec{j}^{IP} has three components, we first discretize the integration operator
41
42 16 including cross product ($\int_v \frac{\mathbf{x} \hat{r}}{r^2} dv$) as

$$43 \quad \mathbf{G}_{Biot} = \begin{bmatrix} \mathbf{e}^T & \mathbf{0} & \mathbf{0} \\ \mathbf{0} & \mathbf{e}^T & \mathbf{0} \\ \mathbf{0} & \mathbf{0} & \mathbf{e}^T \end{bmatrix} \begin{bmatrix} \mathbf{0} & \mathbf{S}_z & -\mathbf{S}_y \\ -\mathbf{S}_z & \mathbf{0} & \mathbf{S}_x \\ \mathbf{S}_y & -\mathbf{S}_x & \mathbf{0} \end{bmatrix}, \quad (\text{C.10})$$

47 17 where

$$48 \quad \mathbf{S}_l = \mathbf{diag}(\mathbf{v} \oplus \mathbf{r}_l \oplus \frac{1}{\mathbf{r}^2}), \quad l = x, y, z$$

49
50 18 and the electric field, $\mathbf{e} \in \mathbb{R}_1^{nE}$ is a column vector, $\mathbf{diag}(\cdot)$ is the diagonal matrix and \oplus is the
51
52 19 Hadamard product. Then we discretize \vec{j}^{IP} shown in eq. (35) as
53
54

$$55 \quad 56 \quad \mathbf{j}_{cc}^{IP}(t) = \mathbf{S} \mathbf{diag}(\mathbf{e}_{max}^F) \mathbf{A}_c^{eT} \mathbf{diag}(\mathbf{v}) \mathbf{diag}(\sigma_\infty) \tilde{\eta}(t), \quad (\text{C.11})$$

57
58 20 where \mathbf{A}_c^e is a discrete averaging matrix from edge to cell center and
59
60

$$61 \quad \mathbf{S} = \mathbf{A}_{ccv}^e \mathbf{M}^{e-1} [\mathbf{M}_{\sigma_\infty}^e \mathbf{G} \mathbf{A}_{\sigma_\infty}^{-1} \mathbf{G}^T - \mathbf{I}] \mathbf{diag}(\mathbf{e}_{max}^F) \mathbf{A}_c^{eT} \mathbf{diag}(\mathbf{v}) \mathbf{diag}(\sigma_\infty). \quad (\text{C.12})$$

1
2
3 48 *Seogi Kang and Douglas W. Oldenburg*
4
5

6 1 Here \mathbf{A}_{ccv}^e is a discrete averaging matrix from edge to cell center with consideration of three compo-
7 2 nent vector: $\in \mathbb{R}_{nE}^{3nC}$. Thus, we can have a linear equation for a single time channel as
8
9

$$\mathbf{b}^{IP} = \mathbf{G}_{Biot} \mathbf{S} \tilde{\eta},$$

10 12 Finally, by letting
13
14 3 $\mathbf{J} = \mathbf{G}_{Biot} \mathbf{S}$, (C.13)
15
16 4 we have
17
18 5 where \mathbf{J} is the Jacobian matrix of the linear equation, and since \mathbf{J} is static, we also obtain
19
20 22
21 23
22 24
23 25
24 26
25 27
26 28
27 29
28 30
29 31
30 32
31 33
32 34
33 35
34 36
35 37
36 38
37 39
38 40
39 41
40 42
41 43
42 44
43 45
44 46
45 47
46 48
47 49
48 50
49 51
50 52
51 53
52 54
53 55
54 56
55 57
56 58
57 59
58 60

$$\mathbf{b}^{IP} = \mathbf{J} \tilde{\eta}, \quad (C.14)$$

$$-\frac{\partial \mathbf{b}^{IP}}{\partial t} \Big| = \mathbf{J} \left(-\frac{\partial \tilde{\eta}}{\partial t} \Big| \right). \quad (C.15)$$

1
2
3
4 *On recovering distributed IP information from inductive source time domain electromagnetic data* 49
5
6
7
8
9
10
11
12
13
14
15
16
17
18
19
20
21
22
23
24
25
26
27
28
29
30
31
32
33
34
35
36
37
38
39
40
41
42
43
44
45
46
47
48
49
50
51
52
53
54
55
56
57
58
59
60

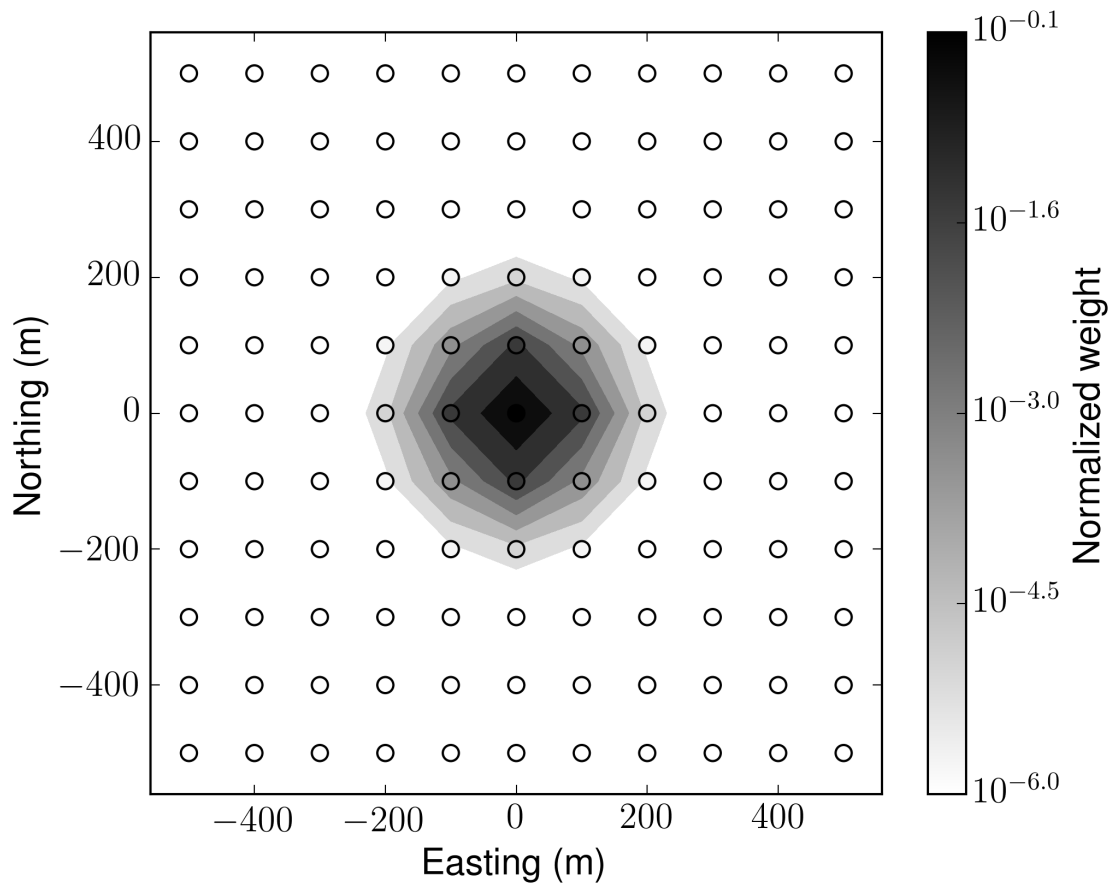


Figure A1. Normalized weights for the conductive case for all transmitter locations. A single pixel located at (0 m, 0 m, -75 m) is used.

50 Seogi Kang and Douglas W. Oldenburg

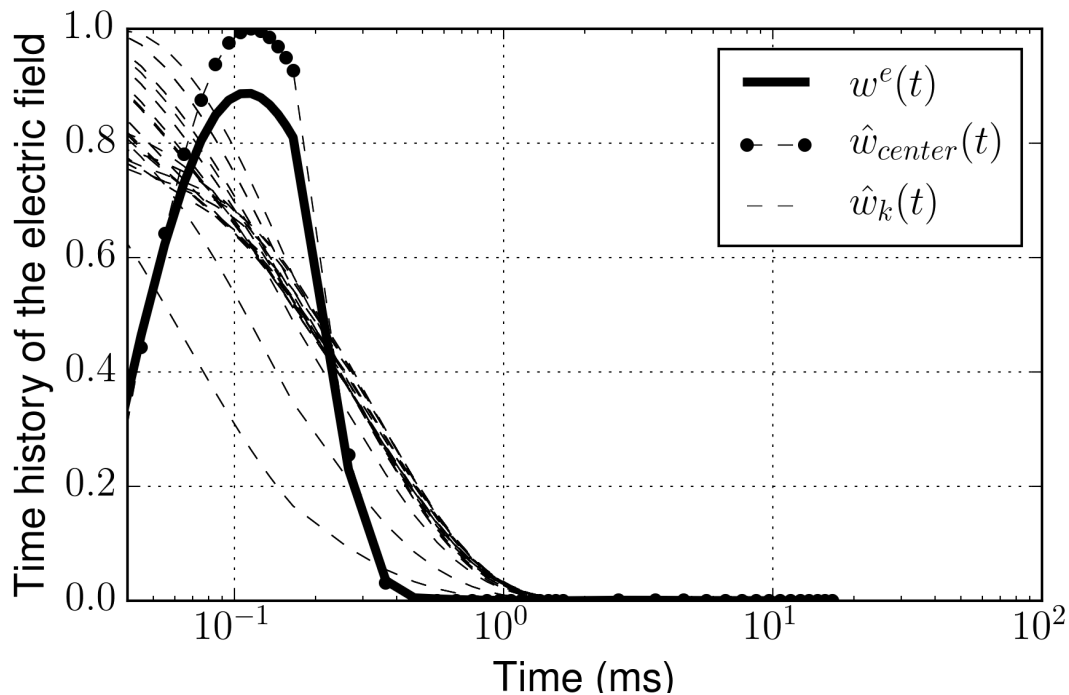


Figure A2. Time decays of $w^e(t)$ and $\hat{w}(t)$ for the conductive case. A single pixel located at (0 m, 0 m, -75 m) is used. Solid line and dashed lines correspond to $w^e(t)$ and $\hat{w}_k(t)$ for all transmitters ($k = 1, \dots, n_{Tx}$); \hat{w}_k at the center transmitter located at (0 m, 0 m, 30 m) is marked as solid circles. A number of $w^e(t)$ curves are overlaid due to the symmetric position of transmitter locations to the conductive block.

1
2
3
4 *On recovering distributed IP information from inductive source time domain electromagnetic data* 51
5
6
7
8
9
10
11
12
13
14
15
16
17
18
19
20
21
22
23
24
25
26
27
28
29
30
31
32
33
34
35
36
37
38
39
40
41
42
43
44
45
46
47
48
49
50
51
52
53
54
55
56
57
58
59
60

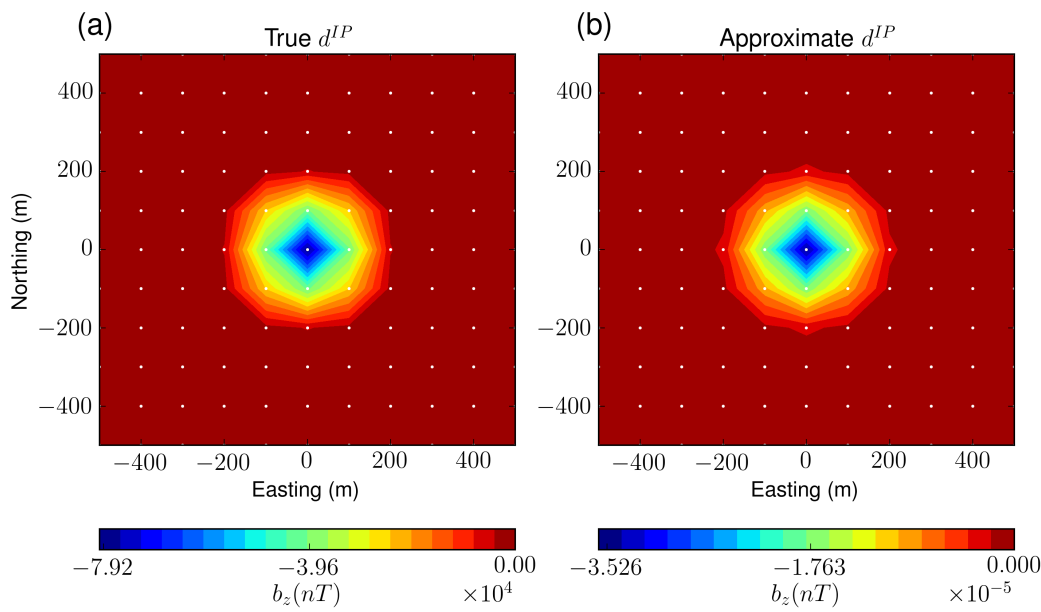


Figure A3. Comparison of true and approximate b_z^{IP} responses at 0.86 ms on plan view map.